Polymer Enhanced Foam in Unconsolidated Sand

Master Thesis in Reservoir Physics

by

Silje Lande

Department of Physics and Technology

University of Bergen

June 2016

Abstract

Foam is an EOR technique that significantly can improve the macroscopic sweep efficiency by lowering the gas mobility. Limited stability of conventional surfactants for foam generation is one of the reasons why foam is not being widely used as a common EOR technique. One proposed approach for foam stabilization is the addition of polymers, so called polymer enhanced foam, and is defined here as an integrated EOR (IEOR) technique. The objective of this thesis was to investigate the observed difference in the development of pressure during co-injection of N_2 gas and two different foaming solutions, one with and one without polymer for foam stability. Foam generation and flow behavior were studied at core scale to evaluate the potential of polymer enhanced foam for IEOR application. In addition, bulk foam stability with or without the presence of different oils was studied using surfactant as foaming agent.

Foam stability was studied during sixteen bulk foam coalescence tests by measuring the half-life of foam with and without the presence of oil. Changes in foam texture and foam height were observed visually, and destruction mechanisms were studied during the foam decay regime. Without oil, foam columns had constant height and a continuous thinning of lamellae by gravity was observed. With oil, the foam columns divided into several parts with a rapid reduction of foam height, depending on amount of oil and oil composition.

Foam generation with and without the addition of polymers for added stability was studied during fourteen co-injections in unconsolidated sand packs. The development in absolute pressure in five pressure ports placed along the sand pack and the pressure gradient across four sections was analyzed to establish if stable pressures were achieved. Stable pressures were achieved using regular surfactants during co-injection with N_2 gas, whereas the pressure did not stabilize with the addition of polymer solution. The pressure drop across the four sections of the sand pack was used to calculate the apparent viscosity of the generated foam to compare flow and foam ability. A variation in apparent foam viscosity was observed along the core length, and in general the apparent foam viscosity increased with higher permeability.

One co-injection of N_2 gas and surfactant+polymer solution was conducted in PET-CT scanner to investigate the local development of the foaming solution. The results showed that saturation development of the foaming solution was not uniform across the scanned section of the sand pack and within t=7 PV the saturation had not reached stable state.

Acknowledgements

I would like to gratefully acknowledge the following people, who were important to me during the experimental work and writing of this thesis:

My supervisor Associated Professor Martin Fernø and Dr. Bergit Brattkås at the Dept. of Physics and Technology, University of Bergen, for valuable guidance and support.

Professor Arne Graue for the opportunity to study Reservoir Physics at the Dept. of Physics and Technology and to travel abroad on conferences for educational purpose.

Research Technician Sverre S. Aksnes at the Dept. of Earth Science, University of Bergen, for guidance and for providing me with necessary equipment.

I also want to thank the mechanical workshop at The Dept. of Physics and Technology for providing me with the custom made sand pack.

Radiographer Bodil Næss at Haukeland University Hospital, Bergen, for help during the experiment performed in the PET-CT scanner.

I have received help from many during the experimental work of this thesis: Dr. Marianne Steinsbø, Inez Luiza Buzdugan, Dr. Jarand Gauteplass and fellow master students Petter Solberg, Håkon Kyte Haugland, Sigbjørn Assheim Johansen and Snorre Vasshus. Thank you!

My fellow master students, especially Mari Høyvik and Sandra Heldal, for appreciated breaks, educational discussions and fun times.

My parents, Hanne Kari and Jostein, and my boyfriend, Jøran, for support and motivation during my years of study.

Bergen, June 2016

Silje Lande

Table of Contents

Introduction

Today many of the world's producing oil fields are mature with declining production rates. The world average of oil recovery factor is estimated to be 35 % (Babadagli, 2007), indicating that large quantities of oil are left behind after conventional recovery due to poor volumetric sweep efficiency and oil entrapment. At the same time, the rate of new conventional discoveries compared to produced reserves has been steadily decreasing over the last decades. To meet the globally increasing energy demand in the years to come it will be essential to implement enhanced oil recovery (EOR) techniques in developed oil fields to optimize recovery (Manrique et al., 2010). It is expected that the global energy demand will increase with 35% from 2010-2040 (Selin, 2013) and fossil fuels will likely be among the main energy resources. The objective of applying EOR techniques is to improve the macroscopic sweep efficiency and microscopic sweep efficiency in the oil field (Zolotukhin and Ursin, 2000).

Gas injection is one of most applied EOR technique worldwide (Taber et al., 1997). However, a challenge associated with gas injection is the unfavorable mobility ratio due the low viscosity of gas that induces viscous fingering and gravity segregation that result in poor sweep efficiency. The unfavorable mobility ratio cause even more gas channeling in heterogeneous reservoirs (Lake et al., 1989). Foam can be utilized to reduce the challenges associated with gas injection. Foam reduces the mobility of gas by trapping large fraction of the gas in the porous media and by increasing the gas viscosity (Hirasaki and Lawson, 1985). In addition, foam can reduce the gas mobility more in high permeable areas of the reservoir and hence mitigate the effects of reservoir heterogeneity (Rossen, 1996). Thus, foam is an EOR technique that improves the macroscopic sweep efficiency by lowering the mobility ratio between displacing and displaced phases (Zolotukhin and Ursin, 2000). The use of foam for mobility control was first suggested in the late 1950s (Bond and Holbrook, 1958) and since then several promising foam pilot tests have been conducted by co-injection of surfactant and gas for mobility control in reservoirs (Patzek, 1996). "Foam in a porous media is defined as a dispersion of a gas in a liquid such that the liquid phase is continuous, and at least some part of the gas is made discontinuous by thin liquid films called lamellae" (Hirasaki, 1989). The lamellae are stabilized by surfactants, and foam stability is vital for achieving a successful foam flooding (Kutay and Schramm, 2004). However, foam will break down over time if the lamellae lack long-term stability. The stability of a single lamella decides the longevity of foam (Farajzadeh et al., 2012). One proposed approach for foam stabilization is the addition of polymers. The technique is called polymer enhanced foam

(PEF) (Sydansk, 1994a). PEF is an integrated enhanced oil recovery (IEOR) technique that combines several EOR techniques into one injection strategy (Brattekås, 2014). The addition of a polymer to a surfactant solution has the potential to improve the viscosity of the liquid phase in foam and the stability of foam (Kutay and Schramm, 2004). Several aspects of PEF have so far been studied successfully during laboratory experiments in the presence and absence of oil for mobility control applications in heterogeneous reservoirs (Xu and Pu, 2014, Sydansk, 1994a, Sydansk, 1994b, Kutay and Schramm, 2004, Kantzas et al., 1999). Kantzas et al. (1999) suggested that PEF had been developed to the point that field testing could be considered, and in 2003 a pilot field test was conducted in the Gudao, Shengli oilfield in China demonstrating that PEF was a promising IEOR technique for highly heterogeneous reservoirs and high water-cut reservoirs (Li et al., 2006). Nevertheless, the relationship between the physical properties of PEF and how it perform in a porous media is not well understood (Kutay and Schramm, 2004) and need to be investigated more experimentally (Brattekås, 2014).

The objective of this thesis was to investigate the observed difference in the development of pressures during co-injection of N_2 gas and two different foaming solutions, one with and one without polymer added for foam stability. Foam generation and flow behavior were studied at core scale to evaluate the potential of polymer enhanced foam for IEOR application. The co-injections were conducted at controlled laboratory conditions using unconsolidated sand packs with diameter 4.65 cm and lengths between 37.8 cm and 38.3 cm. A PET-CT scanner was used to visualize the saturation development of the foam solution within a sand pack. In addition, bulk foam coalescence tests were performed to investigate the foam stability with or without the presence of different oils.

The thesis is divided into four main parts, and subdivided into 15 chapters. Part 1 introduces the relevant background theory and includes an introduction to reservoir upscaling (chapter 1), petroleum reservoirs (chapter 2) and integrated enhanced oil recovery (chapter 3). Part 1 also presents important aspects with foam (chapter 4) and polymer enhanced foam (chapter 5) with respect to applications in the petroleum industry. In addition the basic physics behind in-situ images techniques are briefly presented (chapter 6). Part 2 review the experimental procedure and set up used during foam coalescence tests (chapter 7) and during the surfactant foam and polymer enhanced foam experiments (chapter 8). Part 3 presents the experimental result and discussion of the result from the foam coalescence tests (chapter 9), surfactant foam and polymer enhanced foam experiments (chapter 10). In addition, the uncertainties related to

the experiments are discussed (chapter 11). Part 4 summarize and conclude based on the experimental results and discussion (chapter 12) and give suggestions to further work (chapter 13). References used in this thesis are listed in the end (chapter 14). Appendix consists of uncertainties and examples of uncertainty calculations, experimental results and a list of abbreviations and nomenclature.

Part 1: Theory

1. Reservoir Scaling Techniques

Experiments and modelling in petroleum research are performed at different scales, ranging from pore scale to field scale, to analyze fluid flow in a porous system. **Figure 1.1** illustrates the different scales used in petroleum research. Experiments performed at controlled conditions allow researchers to analyze specific parameters and how they influence fluid flow at pore, core and block scale. The objective is to obtain knowledge about the recovery processes to better understand the complex fluid flow at field scale. Linking the measurements from laboratory pore, core and block experiments to reservoir conditions are called up-scaling. The use of in-situ imaging at core scale such as X-ray computed tomography (CT) and positron emission tomography (PET) can lead to new information about spatial fluid flow in opaque porous systems (Zitha et al., 2011).

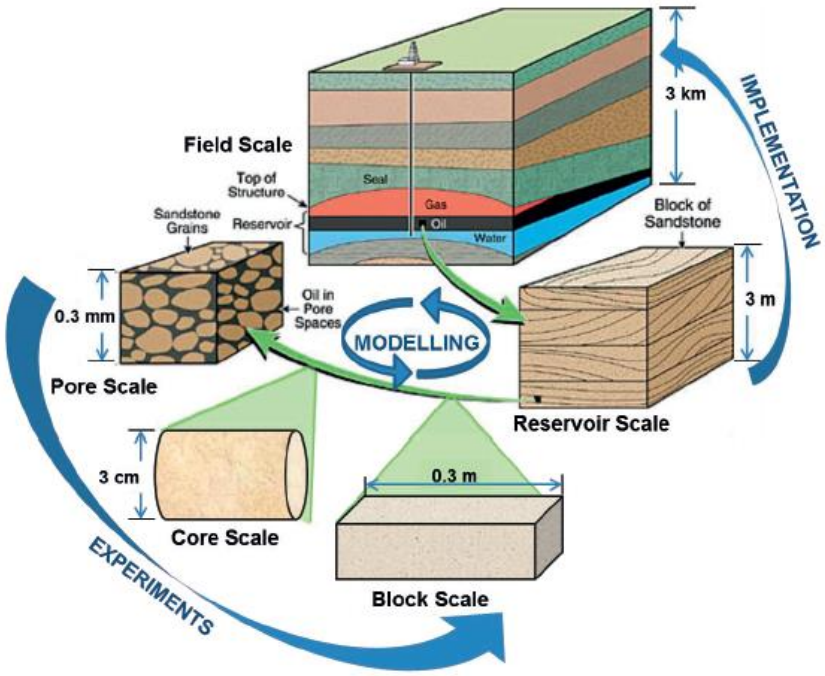

Figure 1.1: Scale levels used in petroleum research (Brattekås, 2014).

2. Petroleum Reservoirs

A petroleum reservoir is a porous and permeable medium that contain brine, oil and gas. The reservoir fluids can flow towards production wells under natural or artificial pressure (Donaldson et al., 1989). The petroleum reservoirs can consist of a variety of materials ranging from loose and unconsolidated sand to dense and hard sandstones or carbonates. Minerals such as silica, calcite and clay bond the grains together (Ahmed, 2006). The key properties of a reservoir rock are porosity and permeability, but pore geometry and the wetting preference of the mineral surface can also affect petroleum recovery (Bjorlykke, 2010). The porosity ranges from 10-25 % and permeability ranges from 0.5 milliDarcy (mD) to 3500 mD in petroleum reservoirs (Donaldson et al., 1989).

2.1 Heterogeneous Reservoirs

All reservoir rocks are to some degree heterogeneous. Reservoir heterogeneity is variations of reservoir characteristics such as permeability, porosity, thickness, saturation, faults, rock facies and rock properties within the reservoir rock. If a homogenous reservoir existed, measuring a reservoir characteristic at one specific location would describe that characteristic for the entire reservoir rock (Ahmed, 2006). Heterogeneous reservoirs can be separated into three groups (Latil et al., 1980):

- **Naturally fractured reservoirs** consist of fractures that divide the reservoir rock into blocks and provide conductive fluid flow.
- **Layered reservoirs** are dominated by horizontal layers of different permeability with or without communication between the layers.
- **Reservoirs with random heterogeneity** have two or more porosity distributions.

Reservoir heterogeneity cause poor sweep efficiency. The displacing phase will preferentially flow into high permeable zones of the reservoir rock and bypass the low permeably zones, consequently leading to a low recovery factor due early breakthrough and bypassing some of the oil in place (Donaldson et al., 1989, Latil et al., 1980).

2.2 Sandstone Reservoirs

Some 60 % of the world`s petroleum reserves are stored in sandstone reservoirs. Sand and sandstone are sedimentary rocks that are composed of sand grains that vary between 1/16 mm and 2 mm in diameter (Bjorlykke, 2010). Quartz is the main mineral in the sand and the sand grains can be held together by silica or another type of cement (Zolotukhin and Ursin, 2000). Sandstone reservoirs at depths shallower than 2.0-2.5 km consist of loose and weakly cemented sand (Bjorlykke, 2010). They can be referred to as unconsolidated sandstone reservoirs and consists of poorly sorted sediments varying between round, fine, medium and coarse sandstone fragments (Zhou and Sun, 2016). The North Sea field, Statfjord, situated at 2.5-3.0 km below the subsurface is one example of a weakly cemented sandstone reservoir. The reservoir consist of sand layers that are so weakly cemented that it is challenging to collect core samples of sufficient quality, due to the sandstone fall apart inside the core sample holder. Sand ingress into the production wellbore can be a problem from these types of reservoirs (Bjorlykke, 2010). Sandstone reservoirs show great potential for utilizing enhanced oil recovery (EOR) methods. Most of the EOR methods have been tested on pilot and commercial scale for this type of reservoirs. **Figure 2.1** shows that most EOR techniques have been utilized in sandstone reservoirs. The results is based on 1507 international EOR projects during the last decade. Thermal and chemical EOR techniques are most widely applied in sandstone reservoirs, whereas gas injection is most common as EOR technique in carbonates and other reservoir rocks (Alvarado and Manrique, 2010).

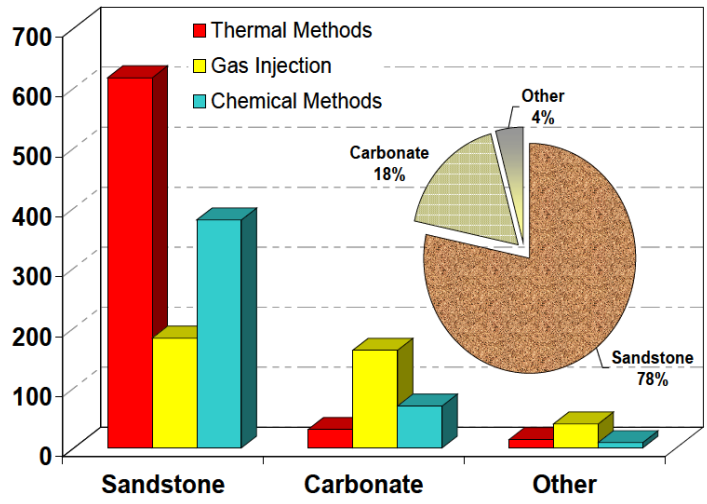

Figure 2.1: EOR techniques by reservoir rocks based on 1507 international EOR projects. The majority of the EOR techniques have been performed in sandstone reservoirs where thermal and chemical techniques are most widely applied, gas injection is the most common in carbonate and other reservoir rocks (Alvarado and Manrique, 2010).

2.3 Porosity and Permeability in Unconsolidated Sand

In this thesis experiments are performed on sand packs that contain unconsolidated sand. The grain shape, grain size, sorting, packing and grain orientation are textural parameters of unconsolidated sand that influence the porosity and permeability. The porosity is defined as the ratio between volume of pore space in a rock which can contain fluids and the total volume of the rock. The pores within a porous medium must be connected to be able to transmit fluids through it and this is the so-called permeability (Selley and Sonnenberg, 2015). Permeability is dependent on porosity, hence properties affecting the porosity will influence the permeability (Zolotukhin and Ursin, 2000). The grain shape in unconsolidated sands can be analyzed by roundness and sphericity (Powers, 1953), see **Figure 2.2**. Limited information exist about how the grain shape influence the porosity and permeability (Selley and Sonnenberg, 2015).

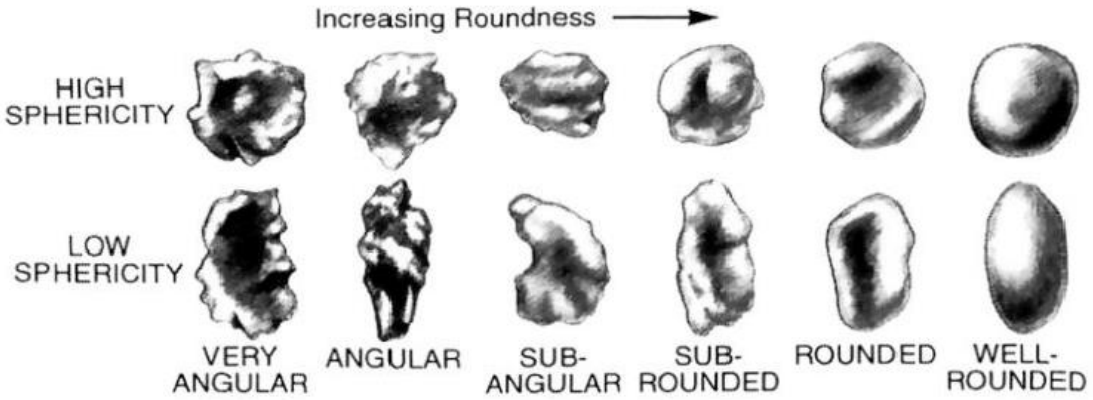

Figure 2.2: The six different roundness classes, very angular, angular, sub-angular, sub-rounded, rounded and well-rounded, and sphericity for sand grains (Selley and Sonnenberg, 2015).

In well-sorted sands the porosity is not affected by the size of the grains. However, in poorly sorted sands the porosity declines with increasing grain size due to larger grains have higher sphericity and are more closely packed than smaller grains with lower sphericity (Rogers and Head, 1961). The permeability declines with decreasing grain size due to reduced pore diameter (Krumbein and Monk, 1943) hence increased capillary pressure (Selley and Sonnenberg, 2015). **Figure 2.3** illustrates how porosity increase with improved grain sorting (Jahn et al., 1998). In poorly sorted sediments, the void space between the pore networks is filled with small particles which cause low porosity and permeability (Fraser, 1935, Rogers and Head, 1961).

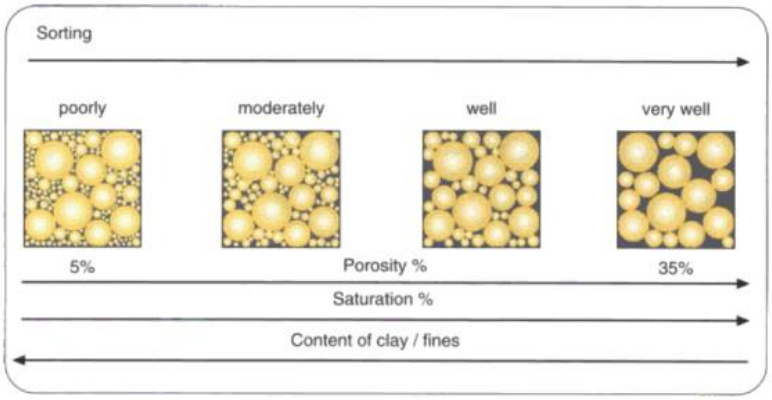

Figure 2.3: Effect of sediment sorting on porosity (Jahn et al., 2008).

Figure 2.4 gives a summary of how sediment sorting and grain size influence the porosity and permeability in unconsolidated sands.

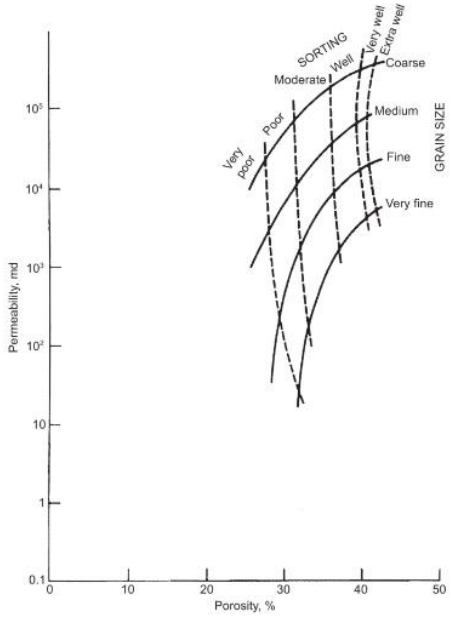

Figure 2.4: Graphical illustration of permeability [md] as a function of porosity [%] showing how sediment sorting and grain size influence the two properties in unconsolidated sands (Selley and Sonnenberg, 2015) after (Beard and Weyl, 1973, Nagtegaal, 1978).

There exist six theoretical packing geometries with spheres of uniform size when considering grain packing in relation with porosity and permeability. The geometry of the theoretical packing vary from the loosest cubic packing with 48 % porosity to tightest rhombohedral packing with 26 % porosity (Fraser, 1935, Graton and Fraser, 1935), see **Figure 2.5**.

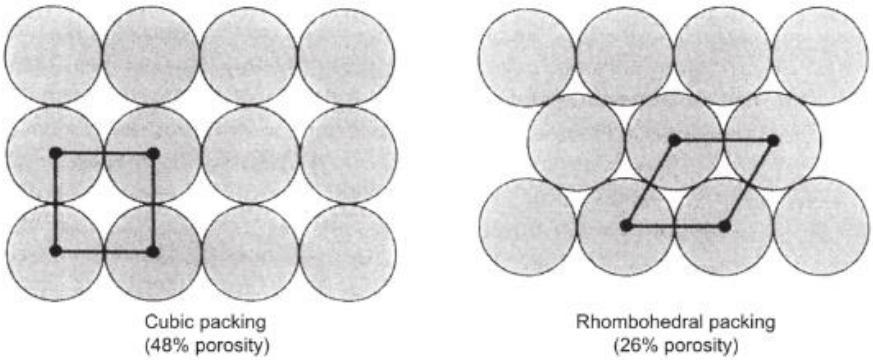

Figure 2.5: On the left hand-side cubic packing with 48% porosity and on the right hand-side rhombohedral packing with 26 % porosity (Selley and Sonnenberg, 2015).

3. Integrated Enhanced Oil Recovery

Motion of hydrocarbons induced by a pressure gradient between reservoir and production wells is the main mechanism behind oil recovery (Donaldson et al., 1989). Oil recovery can be divided into primary, secondary or tertiary phase based upon the producing life of the reservoir (Sheng, 2010). Primary recovery utilizes the natural drive mechanisms originally present in the reservoir (Donaldson et al., 1989, Sheng, 2010). No injection of external fluids or heat is necessary. Expansion of rock and fluids, solution gas, water influx, gas cap and gravity drainage are natural drive mechanisms (Sheng, 2010). 0-50% of the original oil in place (OOIP) can be produced be primary recovery (Ali and Thomas, 1996). Secondary recovery is water injection or gas injection and the objective is to maintain reservoir pressure (Lake, 2010). 20-50% of OOIP can be produced by secondary recovery (Ali and Thomas, 1996). After secondary recovery, tertiary recovery is applied (Lake, 2010, Sheng, 2010) and at this stage the oil is recovered by injection of chemicals, miscible gases and/or heat (Sheng, 2010).

Enhanced oil recovery (EOR) is not limited by the phase of the producing life of the reservoir. EOR processes are divided into three main groups (Sheng, 2010, Lake, 2010):

- Gas injection
- Chemical injection
- Thermal recovery

The objective of applying EOR is to improve the macroscopic and microscopic sweep efficiency. The macroscopic sweep efficiency can be improved be lowering the mobility ratio between displacing and displaced phases (Zolotukhin and Ursin, 2000). The mobility ratio can be lowered by reducing the oil viscosity and the effective permeability of the displacing phase, increase the viscosity of the displacing phase and the effective permeability of oil (Ali and Thomas, 1996). A more favorable mobility ratio results in reduced effects of fingering. The mobility can be controlled by foam injection, polymer flooding, water alternating gas (WAG) (Zolotukhin and Ursin, 2000) and surfactant alternating gas (SAG) (Farajzadeh et al., 2009). The microscopic sweep efficiency can be improved be lowering the interfacial tension (IFT) between the displacing and displaced phases. Enhanced microscopic efficiency results in lower residual oil saturation and can be obtained from surfactant flooding, miscible gas injection and microbial EOR (Zolotukhin and Ursin, 2000).

Integrated EOR (IEOR) is combining several EOR methods together. Potentially IEOR can enhance the macroscopic and microscopic sweep efficiency in a reservoir (Brattekås, 2014). In this thesis foam and polymer are combined, and is called **Polymer Enhanced Foam**.

4. Foam

4.1 Definition

Foam is defined as a gas dispersed in a continuous liquid phase as illustrated in **Figure 4.1**. A foam structure consists of two bulk phases, a gas on the top and at the bottom a fluid. Lamella and Plateau border details are specified within the enlarged area. A two dimensional interface separates the gas phase from thin liquid film. The lamella is the thin film, between two Plateau borders, where three lamellae meet at angles of 120° due to polyhedral arrangement of bubbles in foam (Schramm, 2006). Generation of foam can take place by disturbing an aqueous solution with surfactant while in contact with gas (Sheng, 2013a). The thin liquid films are stabilized by adsorption of surfactant molecules on both sides of the film (Farajzadeh et al., 2012). Without the surfactant as a foaming agent the foam will become unstable and rupture (Sheng, 2013a).

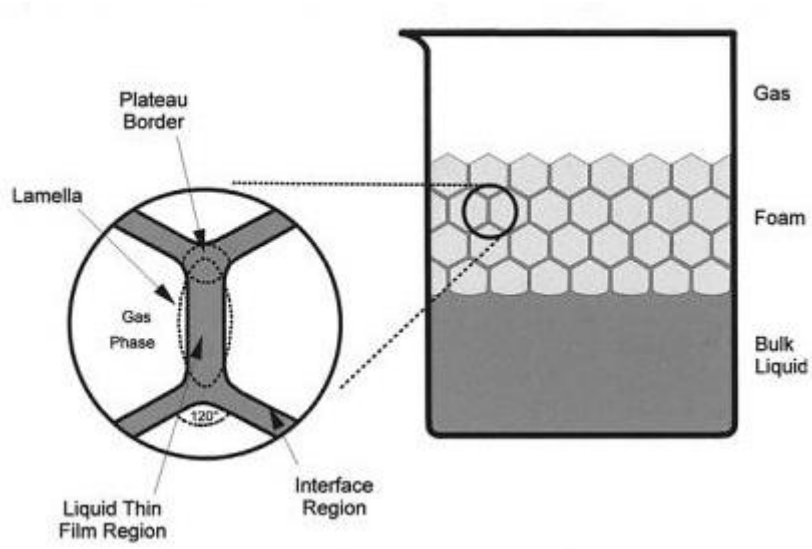

Figure 4.1: A schematic illustration of a foam system. Lamella and Plateau border details in the bulk foam are enlarged on the left-hand side. A container with bulk foam is illustrated on the right-hand side (Schramm, 2006).

Foam in a porous network is different from bulk foam (Manlowe and Radke, 1990, Ransohoff and Radke, 1988). "Foam in a porous media is defined as a dispersion of a gas in a liquid such that the liquid phase is continuous, and at least some part of the gas is made discontinuous by thin liquid films called lamellae" (Hirasaki, 1989). Unlike bulk foam the lamella can stretch over a pore channel causing interactions between lamellae and pore walls which dominate the foam flow behavior (Ransohoff and Radke, 1988). A lamella consist of an aqueous solution separated by gas from both sides.

The thickness of the lamella ranges from a few Nano meters to a few micro-meters, but their area may be as large as 1-2 square meters. Through Plateau borders the lamellae are in direct contact with the liquid phase and each other. The continuous structure of the liquid phase connects the Plateau borders together (Farajzadeh et al., 2012).

We separate between continuous-gas foam and discontinuous-gas foam in a porous media (see **Figure 4.2**). In continuous-gas foam, minimum one continuous gas path exist through the pore network that is not blocked by stationary lamellae. The gas flow as a Newtonian fluid and due to the lamellae the gas relative permeability is reduced. In discontinuous-gas foam, lamellae block all flow paths for the gas. Lamellae have to be transported through the pore network for the gas phase to flow (Hirasaki, 1989).

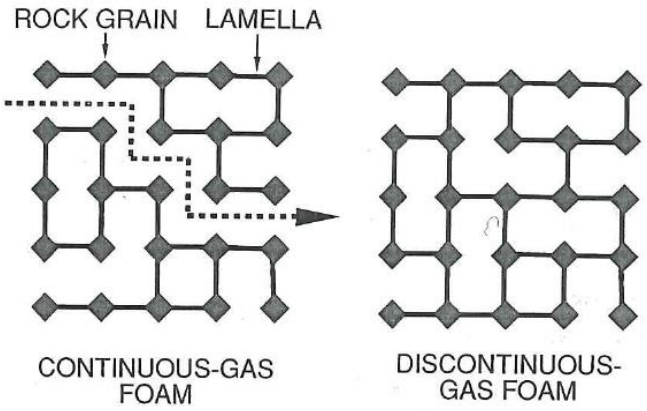

Figure 4.2: A schematic illustration of continuous-gas foam on the left-hand side and discontinuous- gas foam on the right hand-side (Rossen, 1996).

4.2 Foam Characteristics

Foam can be described by foam quality, foam texture and the range of bubble sizes. Foam quality represents the percentage or fraction of gas in foam and can be fairly high, potentially reaching 97 % (Lake, 2010). The foam quality, f_g, can be defined as (Farajzadeh et al., 2012):

$$f_g = \frac{q_g}{q_g + f_{liq}} \tag{4.1}$$

where the gas flow rate is q_g and the liquid flow rate is q_{liq}. Foam quality can represent gas fractional flow in porous network studies. At low gas fractional flow the gas bubbles are widely spaced, separated by thick wetting liquid lenses or bridges, whereas at high gas fractional flow gas bubbles are in direct contact, separated by lamellae. In enhanced oil recovery high gas fractional flow is most used (Romero-Zeron and Kantzas, 2007).

Foam texture is the average bubble size (Lake, 2010). The bubble size can range from 0.01-0.1 µm up to macro emulsions (Lake, 2010). David and Marsden Jr (1969) studied bubble size and bubble size distribution in a porous media. They were able to measure bubble diameter ranging between 0.20 mm to 0.60 mm in porous media. Foam texture is closely linked to foam quality. Foam will become unstable if the bubble size becomes greater, hence lower foam quality (Sheng, 2013a). Foams with a wide range of bubble sizes are expected to be unstable (Lake, 2010). The flow properties of foam in a permeable medium are depend on foam texture. Foam will flow as dispersed bubbles if the average bubble size is smaller than the pore diameter. Opposite, if the average bubble size is greater than the pore diameter foam will flow as a development of lamellae (Lake, 2010). Foam texture determines the pressure-drop/flow-rate relationship of foam in a porous network. In turn, foam texture in porous network is decided by pore-level mechanisms that generate and destroy which are dependent on the ratio between pore-body and pore-throat size (Romero-Zeron and Kantzas, 2007). Foam will obtain a new texture when advancing through a porous network, regardless of whether the foam is generated externally or in situ, because the porous medium will model and reshape the foam (Nguyen et al., 2000, Romero-Zeron and Kantzas, 2007). The processes that generate and destroy foam defines the foam texture (Hirasaki, 1989).

4.3 Foam States and Foam Flow Regimes

No foam, weak foam or strong foam are three states that can occur when foam flow through a porous network, see **Figure 4.3**. The first state (see **Figure 4.3 A**) occurs when originally no lamellae are present due high capillary pressure, high oil saturation or that the porous network is oil wet. These mention properties can destroy or destabilize lamellae. Consequently, conventional gas flooding occur leading to high water saturation in the smallest pores in the porous network. The second state is weak foam (see **Figure 4.3 B**). Weak foam is generated by a moderate increase in the effective foam viscosity that causes a moderate increase in the pressure gradient or reduced water saturation in the porous network. The third state is strong foam (see **Figure 4.3 C**) that is fine textured foams which consist of many lamellae. A significantly increasing pressure gradient or reduced water saturation is caused by the ability strong foam has to increase the effective foam viscosity (or decrease the mobility of the gas phase) (Lee and Kam, 2013).

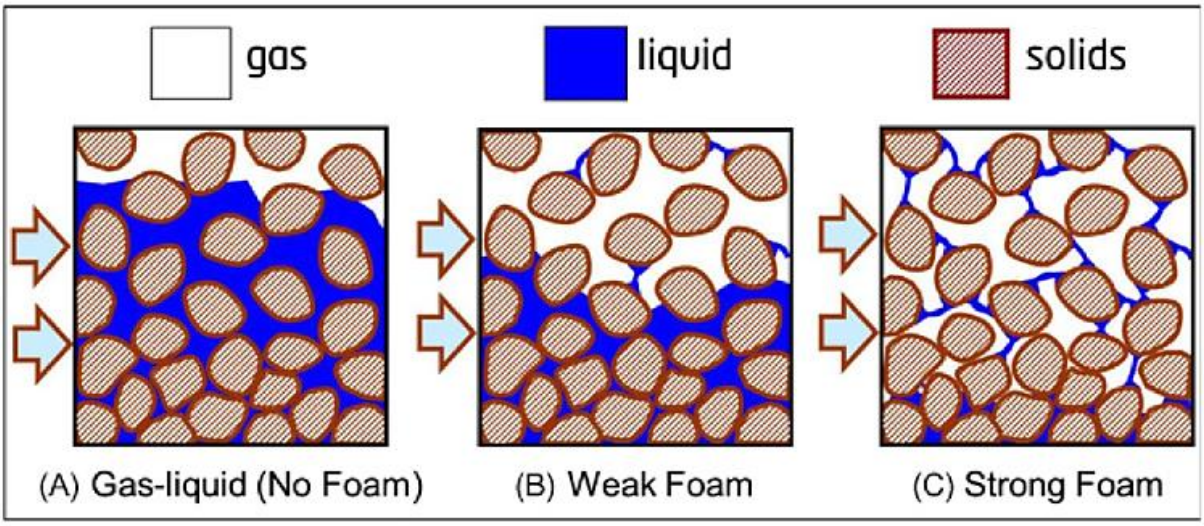

Figure 4.3: A schematic illustration of no foam (A), weak foam (B) or strong foam (C) that are states that can occur when foam flow through a porous network. White, blue and brown indicates gas, water and solids, respectively (Lee and Kam, 2013).

The transition from weak foam to strong foam, i.e. foam generation, happens suddenly and is indicated by a steep incremental pressure drop. Experimental results from the transition from weak foam to strong foam during co-injection of surfactant solution and nitrogen gas into a sandstone core are shown in **Figure 4.4**. Throughout the experiments the foam quality was kept constant and the co-injection rate of surfactant solution and nitrogen gas was increased in steps. The results show that the total pressure drop, Δp_{total}, and the pressure drop in four measure points,$\Delta p_1, \Delta p_2, \Delta p_3, \Delta p_4$, along the core strongly increased when the injection rate, Q_t, reached 1,30 cc/min (Lee and Kam, 2013).

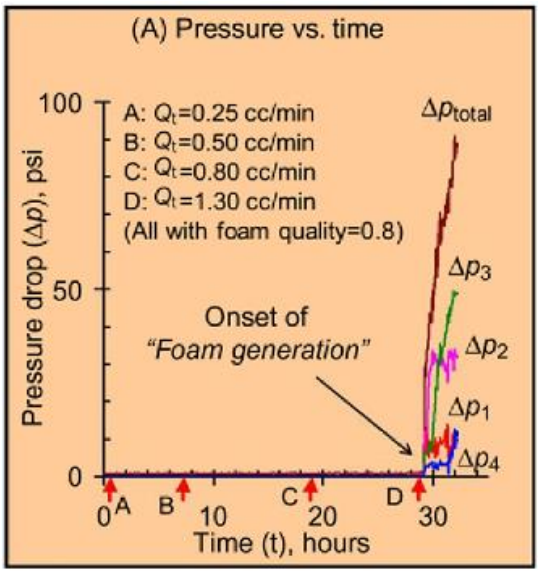

Figure 4.4: Experimental results from co-injection of surfactant solution and nitrogen gas into a sandstone core. The injection rate, Q_t, was increased in steps and the different injection rates are denoted A, B, C and D. The results are presented graphical showing the pressure drop, Δp, as function of time, t. The total pressure drop is denoted Δp_{total}, and the pressure drop in the four measure points are indicted by $\Delta p_1, \Delta p_2, \Delta p_3, \Delta p_4$ (Lee and Kam, 2013) .

In strong foam two flow regimes can be classified based on the gas fractional flow, f_g:

- High-quality regime
- Low-quality regime

In the high-quality regime, the pressure gradient is independent of gas flow rate and dependent on liquid fluid flow rate, whereas in the low quality regime the pressure gradient is independent of liquid flow rate and dependent on gas flow rate. Between the two flow regimes, there is a transition zone, which occur at of f_g^*= 0.94 and this value corresponds to when the critical capillary pressure is reached (Osterloh and Jante Jr, 1992).

Figure 4.5 shows a simplified pressure gradient, Δp, contour plot of foam flow behavior in a porous network. In the transition zone the foam quality is controlled by surfactant properties and the permeability of the porous medium. The foam flow behavior in the high-quality regime is decided by lamellae stability or coalescence and at the critical capillary pressure foam will collapse, hence vertical Δp contours in **Figure 4.5**. In the low-quality regime the foam flow behavior is decided by gas trapping and mobilization, hence horizontal Δp contours in **Figure 4.5** (Alvarez et al., 2001, Lee and Kam, 2013).

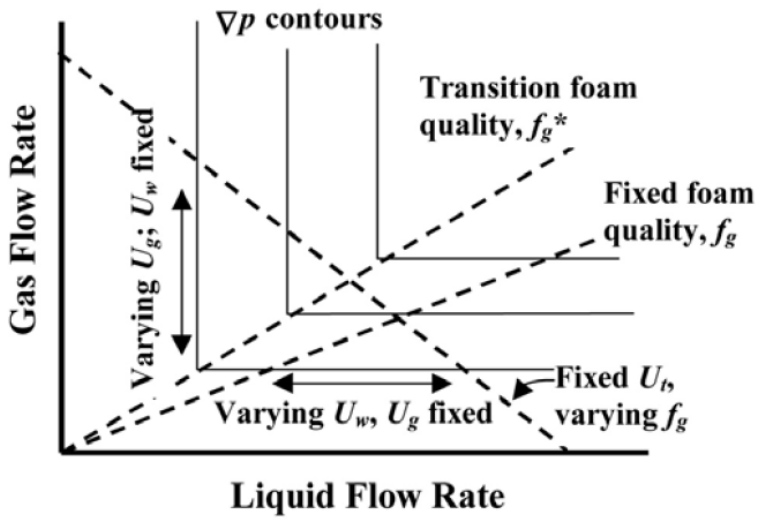

Figure 4.5: A simplified pressure gradient, Δp, contour plot of strong foam flow behavior in a porous network. Δp contours are plotted as a function of the gas flow rate on the y-axis and liquid flow rate at x-axis. The transition is indicated by a specific value of the fractional gas flow denoted f_g^* (Alvarez et al., 2001)

4.3 Foam Generation

A comprehensive understanding of foam generation mechanisms is important to be able to predict the efficiency of foam as an EOR-agent. The flow properties and the apparent viscosity of foam in a porous network are dependent on foam texture and foam texture is dependent on how foam is generated (Ransohoff and Radke, 1988). Co-injection of gas and liquid or surfactant alternating gas injection are two injection methods for generating foam in a porous network. During co-injection gas and liquid are injected at a specific ratio, whereas the latter method inject a surfactant solution and gas in alternating slugs (Farajzadeh et al., 2012). High flow rates or large pressure gradients are required in most cases to make lamellae during foam generation. Foam generation and decay is a dynamic process where lamellae are continuously generated and decayed. In a porous media lamellae can be created by different mechanisms such as leave-behind, snap-off and lamellae division (Ransohoff and Radke, 1988). Once bubbles are created by these pore-level mechanisms gas saturation increases due to trapped gas fraction, which leads to the creation of new bubbles. A sufficient pressure gradient is required to mobilize lamellae otherwise the foam will not be able to flow through the porous media (Chen et al., 2004).

4.3.1 Leave-Behind

The leave-behind mechanism, see **Figure 4.6**, occurs when two gas fronts invade a liquid saturated pore space from different directions and the liquid is pushed into a lamella by the two fronts (Ransohoff and Radke, 1988). This mechanism generates lamellae that are parallel to the flow direction (Nguyen et al., 2000). In a porous body, leave-behind happens relatively often resulting in a large number of lamellae. The lamellae reduce the relative permeability to gas by blocking flow paths (Ransohoff and Radke, 1988). The leave-behind mechanism occur as the saturated pore space is drained by gas generating relatively weak foam (Kam and Rossen, 2003), due to a moderate increase in resistance to gas flow (Ransohoff and Radke, 1988). If leave-behind is the only mechanism generating lamellae, the result is continuous-gas foam (Chen et al., 2004) and low reduction in mobility (Hirasaki, 1989).

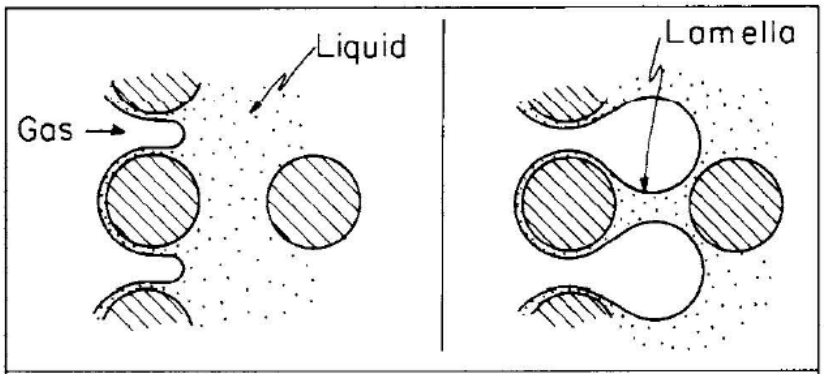

Figure 4.6: A schematic illustration of the leave-behind mechanism for foam generation (Ransohoff and Radke, 1988).

4.3.2 Snap-Off

During snap-off, a non-wetting gas bubble penetrates a pore constriction initially saturated with a wetting phase and a new gas bubble is formed (Tanzil et al., 2000). This pore-level mechanism is illustrated in **Figure 4.7**. Once the gas leaves the pore-neck of the constriction it expands and the capillary pressure decreases creating a pressure gradient in the liquid phase. The pressure gradient enables the surrounding liquid to flow into the constriction and accumulate in a collar (Ransohoff and Radke, 1988). The collar can become unstable if it contains adequate amount of liquid and eventually the bubble will snap-off. In a porous network snap-off is dependent on local dynamic capillary pressure and reservoir heterogeneity to occur (Liontas et al., 2013). Snap-off can happen several times at one location, influencing a large portion of the flow field. This mechanism creates discontinuity in the gas phase and lamellae, hence strong foam is generated. The generated foam can either flow or block gas pathways thus reduce the relative permeability of the gas. Snap-off is the main mechanism behind foam generation (Ransohoff and Radke, 1988).

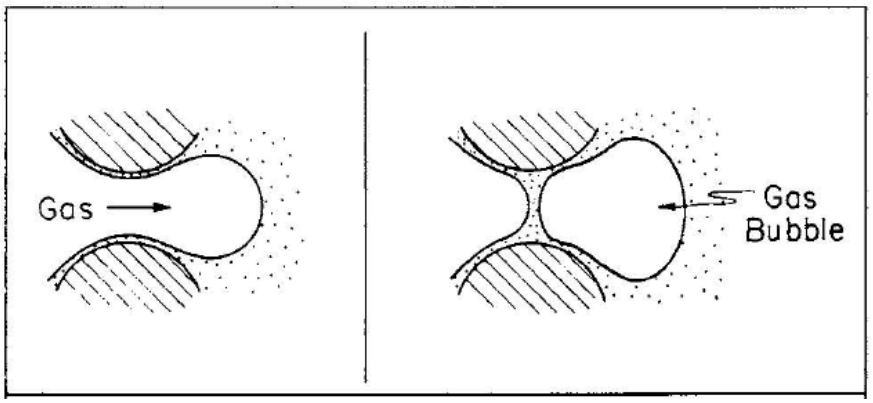

Figure 4.7: A schematic illustration of the snap-off mechanism for foam generation (Ransohoff and Radke, 1988).

4.3.3 Lamellae Division

Lamellae division is a secondary foam generation mechanism. It can only occur after snap-off or leave-behind, because lamellae division requires moving lamellae. Lamellae division occurs when mobile lamellae (pre-generated foam) are split into two or more lamellae at a branch point in the flow field as illustrated in **Figure 4.8**. Studies at pore level are necessary to separate lamellae division from snap-off. Lamella division like snap-off can occur repeatedly at one site and generates strong foam (Ransohoff and Radke, 1988).

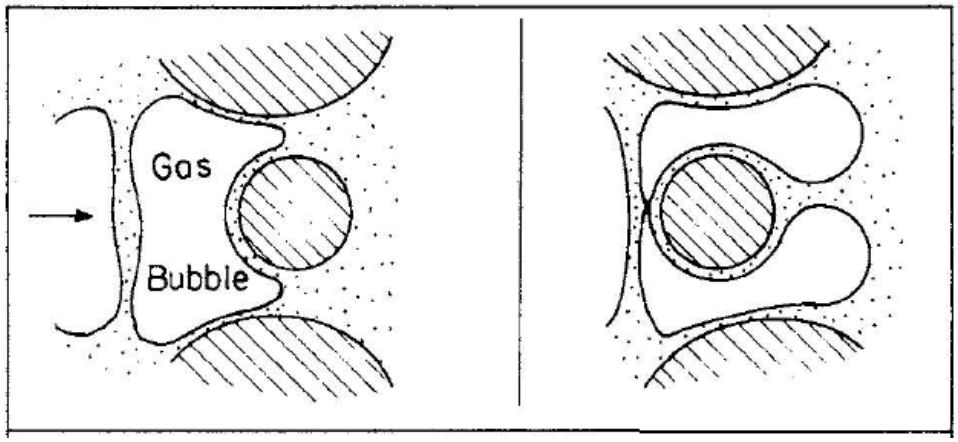

Figure 4.8: A schematic illustration of the lamellae division mechanism for foam generation (Ransohoff and Radke, 1988).

4.4 Foam Stability and Surfactants

The effect of surfactants, capillary suction, critical capillary pressure, bubble size distribution, liquid drainage and oil on foam stability is presented in this chapter. Wettability, diffusion, pressure and temperature are other factors that influence the foam stability (Sheng, 2013a), but will not be further discussed in this thesis as these factors are not taken into account during the experimental work.

A vital criterion for achieving successful foam flooding is foam stability (Kutay and Schramm, 2004). Foam stability is the ability foam has to resist bubble collapse or coalescence (Romero-Zeron and Kantzas, 2007). Foam is not thermodynamically stable, meaning it will break down over time (Sheng, 2013a). The stability of single foam films decides the longevity of foam. The stability of these films are in turn dependent on physiochemical properties and process like surfactant concentration, salt concentration, adsorption, liquid drainage, gas diffusion, surface forces, capillary pressure and mechanical fluctuations (Farajzadeh et al., 2012).

Foam stability can be quantified by measuring its half-life cycle (Sheng, 2013a). This method is used in the experimental work of this thesis by performing foam coalescence tests. The longevity of foam includes stability against film thinning and coalescence. Film thinning, two or more bubbles converge and the liquid film separating them becomes thinner. Coalescence, thin liquid films between bubbles breach and merge into one larger bubble (Schramm, 2006).

4.4.1 Surfactants

A foaming agent acts like a surface active substance. A foaming agent is vital to enable stable lamellae and generate foam (Bureiko et al., 2014). The most common foaming agent, surfactant (Bureiko et al., 2014), consist of a non-polar lipophilic tail and a polar hydrophilic head (Zolotukhin and Ursin, 2000). Surfactants can dissolve in solvents and spontaneous adsorb on interfaces, which reduces the interfacial energy, due to their amphiphilic properties. Foam generation from a surfactant solution can be divided into 3 steps:

1. As gas is injected into the surfactant solutions bubbles are generated. Surfactant molecules cover the created gas-liquid interface.
2. Increased bubble volume fraction and contacting bubbles with surfactant layer causes formation of foam films.
3. The amount of bubbles rises and foam is generated.

In **Figure 4.9** the key steps for generation of surfactant layer is schematically illustrated.

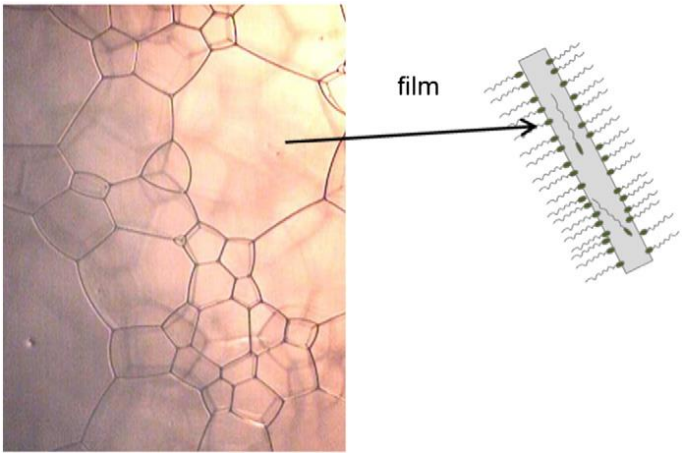

Figure 4.9: Foam with surfactant. On the left hand-side foam is stabilized by surfactant. On the right-hand-side enlarged area of foam film which illustrates surfactant layers at the gas-liquid interface. The surfactants accumulate at the interface with its polar parts in contact with water, whereas the non-polar parts are in contact with air. Surfactant molecules are also present inside the liquid film (Bureiko et al., 2014).

Surfactants stabilize foam by (Bureiko et al., 2014):

1. Enhance elasticity of the liquid films between the gas bubbles and thus increase their resistance to rupture.
2. Strong repulsive forces between surfactant molecules increase the disjoining pressure.

Micelle is an aggregate of surfactant molecules. Micelles form spontaneously at high surfactant concentrations (Schramm, 2006) and the lipophilic parts of the surfactant molecule are oriented inwards and hydrophilic parts outwards (Zolotukhin and Ursin, 2000). Critical micelle concentration (CMC) is the surfactant concentration at which micelle formation becomes dominant. At or above CMC of surfactants the best possible foaming ability is reached (Schramm, 2006). Polymers together with surfactant in a water solution can also be used as a method to stabilize foam (Bureiko et al., 2014) and this method is presented in chapter 5.

4.4.2 Capillary Suction

Lamellae rupture initiated by capillary suction can be explained by the disjoining pressure (Bertin et al., 1998). The disjoining pressure is an additional pressure within liquid films which supports or stabilizes the film. It depends on the film thickness, *h*. The disjoining pressure function, indicated by $\Pi(h)$, is the sum of repulsive forces and attractive forces acting between two interfaces (Skauge et al., 2007). A positive disjoining pressure indicates repulsive forces between film interfaces and the film is stable. A negative disjoining pressure implies attractive forces between the two interfaces and the film is unstable. The disjoining pressure increases when the film thickness decreases until Π_{max} is reached. Π_{max} is equivalent to the critical capillary pressure, P_C^*, for film rupture. The film becomes unstable and break once the capillary pressure exceeds the critical pressure (Skauge et al., 2007). Above P_C^* longevity of lamellae and bulk foam is reduced because at sufficiently high capillary suction pressure (higher than Π_{max}) macroscopic disturbance can start film breaking (Farajzadeh et al., 2012). Adsorption of surfactant molecules at each gas-liquid interface of the film leads to extra repulsive forces (Sheng, 2013a). The disjoining pressure varies with surfactant type, surfactant concentration and salinity (Farajzadeh et al., 2012).

4.4.3 The Critical Capillary Pressure

In a porous medium the stability of foam is dependent on film properties and petro-physical properties of the rock. Two types of films are present in a porous medium (Farajzadeh et al., 2012):

- A foam film which separates the gas bubbles.
- Wetting films that are created at the contact of the foam bubble with the rock surface.

The stability of foam is indirectly linked to the pressure gradient measured over the porous medium. If the pressure gradient is large, the generated foam will have a fine texture, i.e. small foam bubbles. In addition gas, will have lower mobility, hence displacing water to a lower saturation resulting in increased gas-water capillary pressure, until the rate of coalescence equals the rate of foam generation. The rate of coalescence increases when gas-water capillary pressure approaches P_c^*. In porous medium foam become unstable if the gas-water capillary pressure surpasses P_c^*. Since the lamellae in porous medium are flat the capillary pressure on foam films in pore throats are balanced by the disjoining pressure. The capillary pressure as a function of water saturation is illustrated in **Figure 4.10**. The gas-water capillary pressure increases when the water saturation decreases and the fractional flow of gas, f_g, increases. The water saturation, S_w^*, coincides with P_c^* which is a function of the wetting phase and rock morphology (Farajzadeh et al., 2012). In a porous medium all lamellae do not coalescence at the same time. The foam will become coarser with further increase in gas fractional flow while the capillary pressure remains at its critical value (Farajzadeh et al., 2012). The critical capillary pressure can vary with surfactant formulation, gas velocity and the permeability of the porous medium (Khatib et al., 1988).

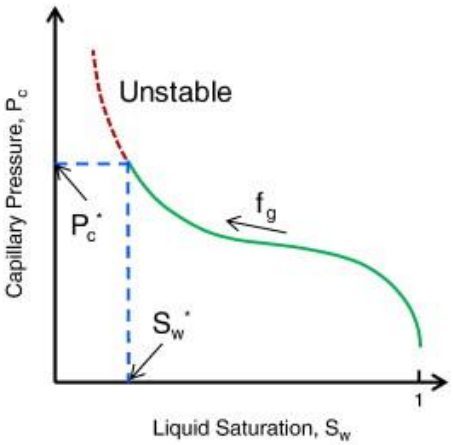

Figure 4.10: Capillary pressure as a function of water saturation. Foam is stable below the critical capillary pressure, P_c^*, which corresponds to the water saturation, S_w^*. The fractional flow of gas is denoted f_g (Farajzadeh et al., 2012).

4.4.4 Liquid Drainage

Liquid drainage by gravity is important to take into account during the foam coalescence test done during the experimental work of this thesis. The foam coalescence tests set-up were performed in cylinders positioned vertically. Liquid films residing in foam can become thinner due to gravity induced liquid drainage. Spherical gas bubbles will transform into polyhedral as liquid flow downwards through existing liquid films. Capillary forces compete with gravity forces during this transformation. Liquid drainage by gravity is shown in **Figure 4.11**. A gas/liquid interface is curved at the Plateau border generating low pressure (P_B), whereas at the flat interface along the thin film region the pressure (P_A) is high. Liquid residing in liquid films is forced to flow towards Plateau border due pressure differences at the interfaces. The process may lead to bubble coalescence due to thinning of the film and movement in the foam (Schramm, 2006).

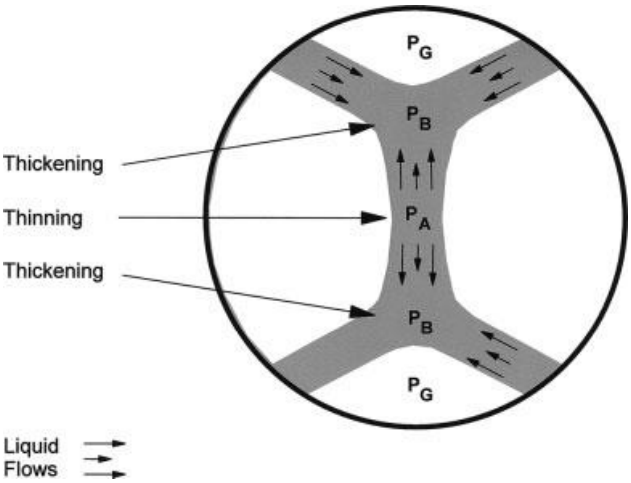

Figure 4.11: Schematic illustration of liquid draining causing film thickening and thinning due to pressure differences across gas/liquid interfaces. Pressure in the thin film region is P_A, pressure in the Plateau border is P_B and pressure in the gas phase is denoted P_G.

4.4.5 Bubble Sizes

Foam stability is not directly a function of bubble size, but there may be an ideal bubble size for the variety of individual foam types that are more stable than other sizes. Foam with a uniform bubble size distribution will act more stable than foam with non- uniform size distribution. Foam containing small sized bubbles are generally more stable than foam with large bubbles (Sheng, 2013a).

4.4.6 The Effect of Oil

The effect of oil on foam stability is essential when considering foam as an EOR method. Oil can affect the stability of foam films. Foam with intermediate or low tolerance to oil is sufficient if foam is to be injected for mobility control in swept regions with low oil saturation. The stability of foam is vital if the foam is going to displace oil (Mannhardt et al., 1998). Reduced longevity of foam due to oil can be explained by surface interactions between oil and foam that in turn depends on multiple physicochemical properties (Farajzadeh et al., 2012). Surfactant depletion, entering, spreading and bridging coefficient, oil emulsification and pseudo-emulsion film are four possibilities of foam destabilization by oil that will be discussed in this chapter.

Surfactant depletion is a mechanism where oil can reduce the stability of foam by changing the interfacial tension at the film surface hence increasing the probability for lamellae rupture. Surfactant depletion can be caused by (Farajzadeh et al., 2012):

1) Partition of surfactant into the oil phase or transfer of the surfactant to oil/water interface leading to reduction of surfactant concentration at the gas/water interface.
2) Oil adsorption into the micelles in the foam or oil can adsorb at the gas/water interface.

Entering *(E)*, spreading *(S)* and bridging *(B)* coefficients are defined as

$$E = \sigma_{gw} + \sigma_{ow} - \sigma_{og} \tag{4.2}$$

$$S = \sigma_{gw} - \sigma_{ow} - \sigma_{og} \tag{4.3}$$

$$B = \sigma_{gw}^2 + \sigma_{ow}^2 - \sigma_{og}^2 \tag{4.4}$$

where σ is the interfacial tension and water, gas and oil is denoted as subscripts w, g and o respectively. Above expressions may be used to describe foam stability when oil is present (Simjoo et al., 2013). An oil droplet must have the ability to enter the gas-water interface to affect the lifetime of foam (Farajzadeh et al., 2012). This is only feasible if the entering coefficient is positive and the oil droplet spreads over the surface i.e. the spreading coefficient is also positive. This leads to expansion of gas-water interface, hence thinning of lamellae and the lamellae will eventually break. Alternatively, the spreading coefficient can be negative meaning no spreading of the oil drop. Instead it will form lens at the gas-water interface (Simjoo et al., 2013). Bridging of lamella will occur if the oil lens remains on one surface of

the lamella and during lamella thinning oil will enter the other surface creating a bridge across the film (Farajzadeh et al., 2012). The bridging coefficient is positive under this condition and the lamella is unstable (Simjoo et al., 2013). Whereas negative values of the bridging coefficient imply stable lamellea (Farajzadeh et al., 2009). The three mention coefficients determine if it is thermodynamically possible in an oil-surfactant system for oil to enter or spread at the gas-water interface (Simjoo et al., 2013). A limitation for entering and spreading coefficients is that it assumes thermodynamically equilibrium, whereas foams tend to be dynamic systems. Application of entering and spreading coefficients correlates best to bulk foams (Schramm, 2006). Foam in porous network with variable pore geometry, pore size, constrictions and interplay of fluids with the rock surface will behave in another way than bulk foam. Direct use of result from bulk foam experiments to explain foam behavior in a porous rock can seem questionable, but have given valuable understanding (Farajzadeh et al., 2009).

The stability of foam in the presence of oil can be related to oil droplet size. Small oil droplets destabilize foam most efficient (Schramm, 2006). Oil emulsification into foam structure is a process where lamellea may breach (Farajzadeh et al., 2012). Small oil droplets are formed by emulsification, which allows oil droplets to enter the structure of the foam (Simjoo et al., 2013).

The lamellae number, L, is a dimensionless parameter to describe foam stability and is defined as (Simjoo et al., 2013):

$$L = \frac{\Delta P_c}{\Delta P_R} = \frac{r_o \sigma_{gw}}{r_p \sigma_{ow}} \tag{4.5}$$

where ΔP_c is the capillary pressure at the plateau border and ΔP_R is the pressure difference across the oil-water interface. The radius of the oil droplet and the radius to the plateau border is denoted r_o and r_p respectively. σ is the interfacial tension and water, gas and oil are denoted as subscripts *w, g* and *o* respectively. Oil droplets are small enough to enter lamella due to capillary suction in the plateau border if the lamellae number > 1. Low lamellae number and entering coefficient<0 give the most stable foam (Farajzadeh et al., 2012). In a porous network that contains oil the lamellae number can together with bulk entering and spreading coefficients describe foam stability. A limitation is that oil droplets as small as the thickness of lamellae (5-50 nm) will likely not be formed in a reservoir (Farajzadeh et al., 2012).

A pseudo-emulsion film is defined as a thin aqueous film enclosed by gas on one side and oil on the other (Schramm, 2006). In the presence of oil, foam can only be stable if oil and gas remains separated by this thin aqueous film (Mannhardt et al., 1998). The foam will rupture if the pseudo-emulsion film breach due to contact between oil droplet and gas-water interface (Simjoo et al., 2013). The pseudo-emulsion film may be metastable in a dynamic foam system even when the entering coefficient > 0 (Schramm, 2006).

The stability of foam in a porous network is more complicated than in bulk foams, thus considering only bulk physical properties and bulk foam measurements is not a reliable source for how efficient foam is in a porous network. The efficiency of foam in porous medium is best considered by studying foaming properties during micro- or macro scale experiments (Schramm, 2006).

4.5 Foam Mobility and the Trapped Gas Fraction

This chapter gives an introduction to factors describing foam flow behavior. These factors are vital when analyzing the results obtain from the surfactant foam and polymer enhanced foam by co-injection experiments performed in this thesis.

During foam flooding in a porous rock the mobility of the gas phase within foam is reduced significantly compared to the mobility of gas during gas flooding (Sydansk and Romero-Zeron, 2010). Gas viscosity and yield stress are two features in foam rheology that are responsible for the ability foam has to control gas mobility and act as blocking agent. Yield stress is the reason for that a large fraction of the gas phase is trapped during foam flow in a porous network, which causes a decrease of the relative permeability of gas (Nguyen et al., 2009). Foam does not affect the relative permeability or viscosity of the liquid phase constituting the foam. In a porous media foam mobility is determined by the foam texture (Bertin et al., 1998). The foam texture influences the viscosity of the gas phase in foam. The gas in foam has increased viscosity when the gas bubbles have a uniform size distribution (Nguyen et al., 2000). Apparent foam viscosity, relative permeability or the mobility reduction factor can describe the behavior of foam flow (Sheng, 2013a).

It is challenging to separate between permeability and viscosity when foam is present in a porous medium. The effects of foam may be easier to describe by combining all the effects into one effective parameter called the Apparent Foam Viscosity. The apparent foam viscosity is defined by Darcy's law (Kantzas et al., 1999):

$$\mu_{app} = \frac{KA\Delta p}{qL} \tag{4.6}$$

where μ_{app} is the apparent foam viscosity [Pa*s], K is the absolute permeability [cm^2], A is the cross sectional area of the sand pack $[cm^2]$, ΔP is the differential pressure across the sand pack [Pa] and q is the flow rate $[cm^3/s]$.

In a porous medium the wetting aqueous surfactant solution will flow as a separated phase in the smallest pores due to capillary forces. Foam will flow through the largest pores due to low flow resistant compared to other possible flow paths. Consequently, the relative permeability of the wetting phase is unchanged in the presences of foam. Blocking of flow paths due to trapped gas saturation in intermediate sized pores reduces the effective permeability of gas advancing through the pore network resulting in a lower gas relative permeability.

The efficiency of generated foam can be characterized by the mobility reduction factor (MRF), which is defined as (Vikingstad et al., 2005):

$$MRF = \frac{\Delta P\ (foam)}{\Delta P\ (no\ foam)} \tag{4.7}$$

where $\Delta P\ (foam)$ is the measured pressure drop across a porous medium with foam, while $\Delta P\ (no\ foam)$ is the measured pressure drop with no foam present. The porous rock, all chemical compositions present, foam quality, foam texture, flow rate, temperature and pressure are properties influencing the mobility reduction factor (Schramm, 2006).

Immobilizing or trapping a large portion of the gas is the main mechanism behind the ability foam has to reduce the gas mobility. Trapped gas does not contribute to flow of gas and it increase resistant for gas flow by reducing the cross sectional area available for flow (Hirasaki, 1989). Trapped gas can be defined as a substantial portion of the gas in foam exists within trapped lamellae. Foam flow through a porous network is significantly affected by this pore-level mechanism. Trapped lamellae can block large areas in the porous rock initially available for flow, resulting in reduced relative permeability of gas (Radke and Gillis, 1990). During foam transport the trapped gas saturation can be 99% or higher (Farajzadeh et al.,

2011). Determining trapped gas saturation is vital to predict foam flow resistance (Radke and Gillis, 1990). The most important factors influencing gas trapping are pressure gradients, gas velocity, pore geometry, foam texture and the length of the bubble train (Kovscek and Radke, 1993). Initiate movement of the lamellae demand a sufficient pressure gradient to push them out of the pore throat and into a pore body (Chen et al., 2004). A maximum pressure gradient where all lamellae will flow have not been established, hence there will always be a fraction of trapped gas within a porous rock during foam flooding (Nguyen et al., 2000). In trapped gas saturation the gas flow is limited due to slow diffusion through lamellae (Farajzadeh et al., 2011). The gas will continue to flow as a Newtonian fluid with reduced relative permeability if lamellae only block some pore throats. Gas will act as it has yield stress if there are sufficient lamellae to block gas movement entirely (Chen et al., 2004).

Trapping of gas in a porous medium, see **Figure 4.12**, is caused by small liquid filled pore throats. The trapped gas bubbles, shown as dark blue, resides in the smallest pore throats shown in the uppermost and lower most pore channel in the figure. In the uppermost channel the trapping is caused by a lamellae resting at the exit of the right most pore throat. A large pressure drop is necessary to mobilize the lamellae. In the lowermost pore channel mobilization of the trapped gas bubbles situated next to a lens of the wetting phase requires a sufficient pressure drop to overcome the capillary threshold pressure of the pore throat. Mobile foam, illustrated as light blue, flows as bubble trains around the trapped gas and through the intermediate constricted pore that has larger pore throats. Foam flow resistant is lower in this area compared to smaller pore channels. Dark arrows indicate pore throats causing blocking (Radke and Gillis, 1990).

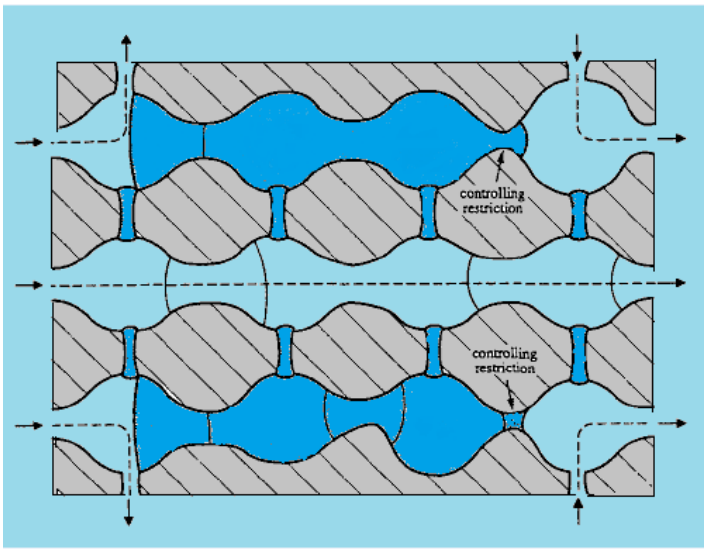

Figure 4.12: Trapping of gas by small liquid filed pore throats. The dark blue areas indicate trapped gas, mobile foam is light blue, grey is solid grain and arrows illustrates the pore throats responsible for gas trapping. Modified from (Radke and Gillis, 1990).

Figure 4.13 shows the distribution of foam in a porous rock. Sand grains are indicated by grey and white represents the wetting phase. Mobile foam is indicated by light blue, while trapped gas bubbles are dark blue. Only 1-15 % of the gas phase is mobile during foam flooding in a reservoir (Sydansk and Romero-Zeron, 2010). The wetting phase resides in the smallest pores due to capillary forces and thereby gas is the non-wetting fluid. Gas bubbles are trapped in intermediate sized pores. Mobilization of the trapped gas requires larger pressure drops in smaller pore throats. Therefore are gas bubbles trapped in pore throats larger than those taken up by the wetting phase (Radke and Gillis, 1990).

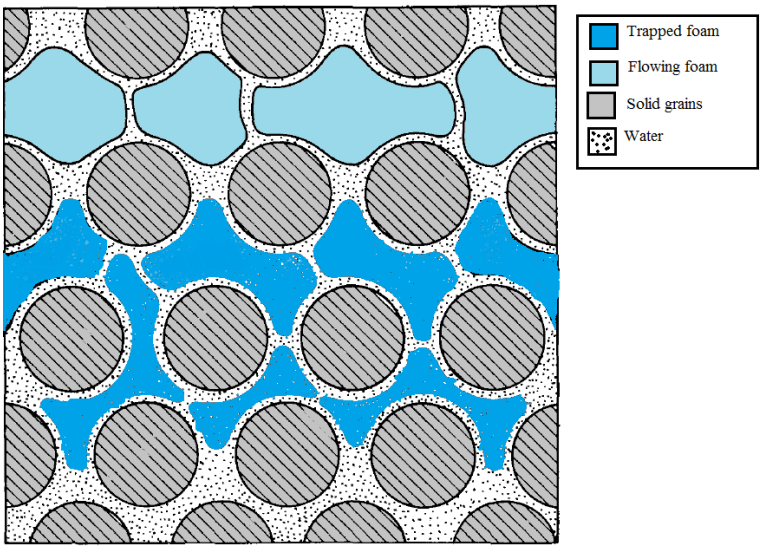

Figure 4.13: Foam distributions in a porous rock. Sand grains are indicated by grey color. White represents the wetting phase. Mobile foam is indicated by light blue, while trapped gas is denoted by dark blue. Modified from (Radke and Gillis, 1990).

The reduced mobility of the gas phase during foam flooding in a porous network is caused by the combination of foam-induced permeability reduction and improved apparent foam-induced viscosity. To summarize there are two mechanism that are responsible for the reduced mobility of the gas phase in foam (Sydansk and Romero-Zeron, 2010):

- The formation or increased trapped gas fraction
- Reduced mobility of the gas phase since gas has to advance through the porous network within the lamellae.

4.6 Foam in EOR

Carbon dioxide, nitrogen, steam, air and hydrocarbon gases are used in EOR (Farajzadeh et al., 2012). A problem associated with gas injection is the poor sweep efficiency, which causes the overall oil recovery to be low since gas only contacts and sweep a small portion of the oil within the reservoir (Kovscek and Radke, 1993, Rossen, 1996, Farajzadeh et al., 2012). Poor sweep efficiency is caused by (Farajzadeh et al., 2012):

1. Gas channels through high permeable zones in heterogeneous reservoir.
2. Viscous fingering caused by differences in viscosity between gas and oil
3. Gas has lower density than brine and oil resulting in gravity overriding. Gas rises to the top of the reservoir and overrides the oil-rich zone.

Foaming of the injected gas phase will reduce the gas mobility within the porous network leading to improved sweep efficiency (Kam and Rossen, 2003). The displacement fronts of gas and foamed gas are illustrated in **Figure 4.14**.

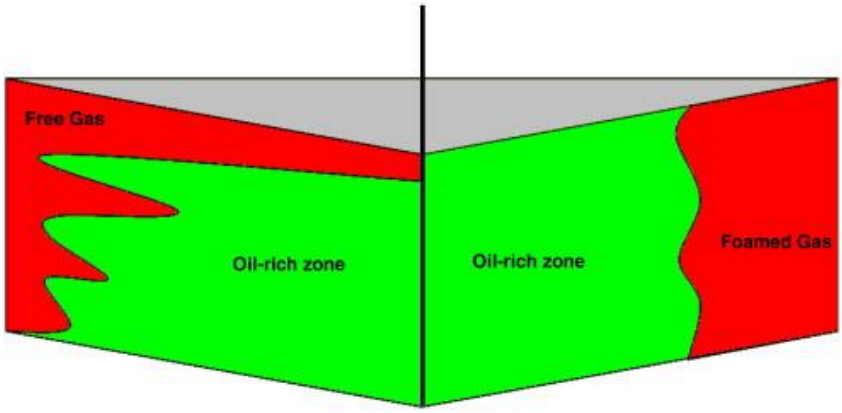

Figure 4.14: Gas flooding vs. foam flooding. The gas displacement front is unstable and inefficient. Foaming of gas results in lower gas mobility due to improved displacement (Farajzadeh et al., 2012).

Compared with gas injection, foam can improve the oil recovery in two ways:

1. Increasing the viscosity of the displacing fluid resulting in a stable displacement process due to a more favorable mobility ratio.
2. Block high permeable swept areas and divert fluid into to un-swept areas.

During foam flooding, since gas contact more oil, mass transfer between gas and oil at the interface will also be essential for the mobilization of oil in the reservoir. Dissolution, viscosity reduction and swelling are mechanisms behind the oil mobilization (Farajzadeh et al., 2012). Brine and crude oil have a higher density than foam. However, these density

differences can cause gravity override during foam flooding in the reservoir (Tanzil et al., 2000).

Reservoir heterogeneity can cause poor sweep efficiency (Sheng, 2013a) and foam can reduce the gas mobility in reservoir areas with higher permeability, hence mitigate the effects of heterogeneity (Kam and Rossen, 2003). Foam has an increased ability to reduce gas mobility with increasing absolute permeability. Consequently, foam is stronger in high permeability zones than in lower permeability zones (Hirasaki, 1989).This is caused by non-wetting gas residing in high permeability areas, hence the injected flow gets diverted into areas with lower permeability (Sheng, 2013a).

Foam used as blocking agent face other demands than foam utilized to improve sweep efficiency. As blocking agent foam need to function as flow barrier and be capable to entirely fill a specified volume within all possible sites of gas flow. The greatest feasible mobility reduction for the longest period can be gained if the blocking foam remain in place and exert long-lasting stability (Kutay and Schramm, 2004).

A challenge in foam flooding processes is to select a suitable surfactant (Schramm, 2006). Characteristics required for a surfactant to be effective in a porous network under reservoir conditions according to Schramm (2006):

- "Good solubility in the brine at surface and reservoir conditions
- Good thermal stability under reservoir conditions
- Low adsorption onto reservoir rock
- Low partitioning into the crude-oil phase
- Strong ability to promote and stabilize foam lamellae
- Strong ability of the foam to reduce gas mobility in porous media
- Good tolerance of the foam to interaction with crude oil in porous media."

The economics of foam injection is dependent on how much surfactants are required to generate and establish foam flow within a porous media. Unwanted mechanisms of surfactant loss by partitioning into the crude-oil phase and through adsorption onto reservoir rock cannot be completely excluded (Schramm, 2006). In addition, surfactant retention also affects the economics of foam flooding. Both adsorption and retention of surfactant should be careful considered when choosing surfactant for foam flooding of a reservoir (Sydansk and Romero-Zeron, 2010).

5. Polymer Enhanced Foam

Polymer enhanced foam (PEF) is addition of a water-soluble polymer to a foam system (Sydansk, 1994a). Polymer enhanced foam can be generated by using the same type of gases and surfactants used in conventional foam. The addition of polymer increase the liquid phase viscosity hence improving the foam stability (Kutay and Schramm, 2004, Sheng, 2013a) by adsorbing at the interface like surfactants (Bureiko et al., 2014). The increased foam stability is caused by decreasing the rate of liquid drainage, reducing the rate of gas diffusion (Sydansk, 1994a) and reduce the gas permeability of the lamellae (Bureiko et al., 2014). PEF can be utilized to control the mobility ratio and enhance the sweep efficiency in an oil reservoir (Sydansk, 1994a). One can regulate the viscosity of the liquid phase in PEF by varying polymer concentration and molar mass. In addition, foam quality and foam texture will be affected by adding polymer to the aqueous foam. The choice of polymer type is based upon application, sweep efficiency or blocking and diverting fluids, and environmental properties such as the temperature, salinity, pH and shear conditions (Kutay and Schramm, 2004).

5.1 Polymers

A polymer added to the injection water is an EOR method referred to as polymer flooding. The purpose is to decrease the mobility of water. This leads to increased water viscosity and a reduction in the relative permeability to water. The result is a lower mobility ratio, which is more favorable for oil recovery due to improved volumetric sweep efficiency. Application of polymers is advantageous in reservoirs where the oil viscosity is high or in heterogeneous reservoirs (Lake, 2010, Zolotukhin and Ursin, 2000). It is of importance to understand and have knowledge about how reservoir and fluids will affect characteristics of the polymer solutions to optimize its efficiency and reduce uncertainties (Zolotukhin and Ursin, 2000).

Polymer has a molecular weight in the million, hence only a small amount of polymer (0.1 to 1 ppm) added to the water will increase its viscosity significantly (Lake, 2010, Latil et al., 1980). Polymer molecules are long chains of repeating organic molecular entities, referred to as monomers (Zolotukhin and Ursin, 2000, Sydansk and Romero-Zeron, 2010). The synthetic polymer hydrolyzed polyacrylamide , HPAM, and the biopolymer Xanthan are the most common used polymers in enhanced oil recovery (Lake, 2010, Sydansk and Romero-Zeron, 2010, Zolotukhin and Ursin, 2000). The viscosity of foam can be considerably improved by adding a polyacrylamide polymer (Kutay and Schramm, 2004).

In this thesis, HPAM will be utilized to enhance foam flooding. HPAM is a polyacrylamide that has been partly hydrolyzed. HPAM's physical features are due to its negative charged molecule caused by hydrolysis. The normal degree of hydrolysis is 30-35% which has been chosen to modify water solubility, viscosity and retention. The synthetic polymer will not be soluble in the aqueous phase if the hydrolysis is too low. If the hydrolysis is too high, HPAM will be sensitive to salinity. HPAM have the ability to increase the water viscosity due its large molecular weight (Lake, 2010). Polymers have shear-dependent viscosity and the viscosity decreases with increasing shear rate. The viscosity increasing property of synthetic polymers is affected by mechanical degradation, high temperature and high salinity. The synthetic polymer is elastic and can be exposed to mechanical degradation due to high shear rate at the injection well. Within a temperature range of 70-90 °C the synthetic polymer is stable. Above this temperature range it can be exposed to degradation. Reduced viscosity is caused by high salinity (Skarestad and Skauge, 2005). The latter is a challenge in many reservoirs. HPAM has low costs, is resistant to bacterial attacks and reduces permeability permanently (Lake, 2010).

5.1.1 Polymer Retention

Polymer retention includes all mechanisms causing removal of polymer molecules from water solution during flow through a porous network. Polymer molecules can be retained by the porous rock during polymer flooding due to interactions between the two of them. Consequently, the efficiency of the polymer flooding is reduced since polymer molecules will be removed completely or partially from the injected fluid leading to a lower viscosity compered to original polymer solution (Sorbie, 2013). The loss of this mobility control effect is significant at low polymer concentrations. In addition polymer retention can cause a delay in the velocity of the polymer front and create oil bank propagation (Lake, 2010). A positive consequence of polymer retention is that the permeability of the porous rock can be reduced in areas where retention occurs (Sorbie, 2013). The permeability reduction cause additional reduction of the mobility of polymer and water which will contribute to increased oil recovery (Zolotukhin and Ursin, 2000). Despite the permeability reduction, polymer retention generally has a negative impact on the oil recovery. Polymer retention depends on polymer type, molecular weight, rock composition, brine salinity, brine hardness, flow rate and temperature (Lake, 2010). Polymer retention will normally be lower during polymer flooding under reservoir conditions compared to experimental tests due to lower flow rates (Chang, 1978).

Polymer retention is caused by the following mechanisms (Sorbie, 2013):

- Adsorption on solid surfaces
- Mechanical trapping in pores
- Hydrodynamic retention

The three retention mechanisms are illustrated in **Figure 5.1**.

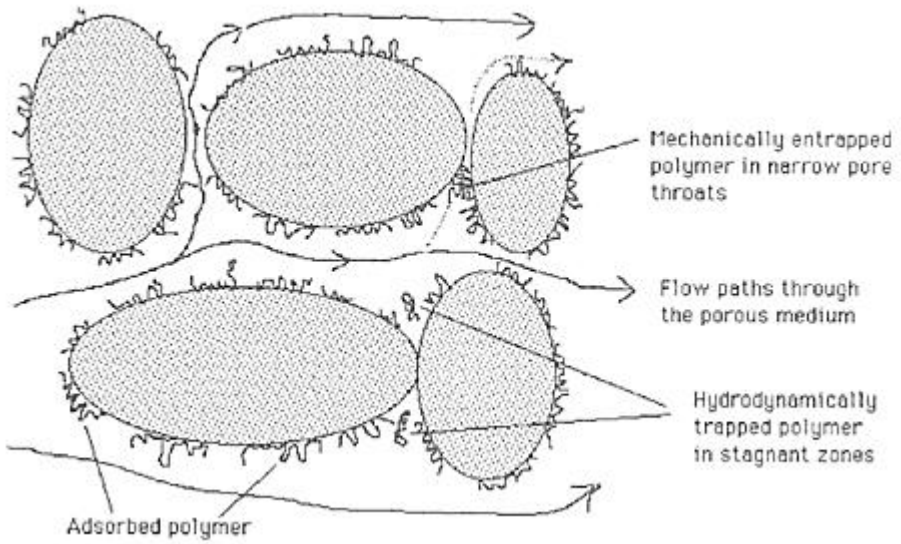

Figure 5.1 Schematic illustration of the three retention mechanisms in a porous network, namely adsorption, mechanical trapping and hydrodynamic retention (Sorbie, 2013).

Hydrodynamic retention and mechanical trapping can only occur when a polymer solution flow through a porous network (Sheng, 2013b). Hydrodynamic retention is observed as increasing polymer retention with increasing flow rate during experimental polymer flooding of cores. The mechanism is not well understood (Sorbie, 2013) and will not be further discussed, because it is most likely not contributing a lot to the total retention (Sheng, 2013b). Adsorption of polymer on solid rock surfaces and mechanical trapping in pores are important mechanism behind the overall polymer retention in a reservoir (Chang, 1978). Mechanical trapping in pores occur when large polymer molecules flow through narrow pore throats (Sheng, 2013b). Polymer adsorption onto the solid surface of the porous rock is caused by interactions between the polymer molecules and the porous rock (Sorbie, 2013).

Concerning polymer adsorption three results have been seen (Chang, 1978):

- Experimental polymer flooding compared with reservoir polymer flooding shows more polymer retention.
- In sand packs the adsorption is significantly higher than in consolidated cores.
- High water salinity cause more adsorption.

5.1.2 Inaccessible Pore Volume

Polymer molecules can be larger than some pores within a porous network. Hence, no flow of polymer molecules will pass through these narrow pore throats. Inaccessible pore volume, IPV, is defined as the volume of pores not available for polymer molecules (Sheng, 2013b) and can be as high as 30 % of the total pore volume (Chang, 1978). Both adsorption and IPV causes velocity differences between a polymer solution and water when flowing through a porous network (Chang, 1978). As mentioned in the previous chapter adsorption reduces the velocity of the polymer front compared to water (Chang, 1978), causing delayed breakthrough (Sheng, 2013b). IPV cause polymer solution to flow at a higher velocity than water (Chang, 1978), consequently reaching the outlet faster (Sheng, 2013b). Combination the two factors results in a smaller volume of polymer solution flowing through the porous network. IPV causes polymer flooding to advance and displace oil faster than expected based on porosity (Chang, 1978). Polymer molecular weight, permeability, porosity and pore size distribution are properties that affect IPV (Lake, 2010).

5.2 Surfactant- Polymer Interactions

The interaction between surfactant and polymer in bulk and at the interface between gas and lamellae in foam are complex. Electrostatic and/or hydrophobic forces control the interactions. Factors such as salt, surfactant or polymer concentration, molecule structure, the degree of branching, charge density and backbone rigidity affect the forces between surfactant and polymer (Bureiko et al., 2014). Surfactant adsorb to polymer to achieve a more energetically state than they do in micelles (Jenkins and Bassett, 1997).

5.3 The Structure of Polymer Enhanced Foam

Knowledge about the structure of polymer enhanced foam is required to understand how it will behave flowing in a porous network. In a porous rock, if the lamellae are parallel to the flow direction, they can stretch over several pores. Lamellae can also span across multiple pores. The structure of polymer enhanced foam lamellae flowing in a porous medium matches the structure of bulk foam. In a pore space the polymer enhanced foam is lamellar and is

orientated three-dimensionally. The thickness of lamellae is 1-12 μm. An anionic surfactant is used during the polymer enhanced foam by co-injection in sand packs in this thesis. The lamellae of polymer enhanced foam obtained from anionic surfactant have dimensions that are of the order of and smaller than pores. These lamellae appear as thin films, rod-like filaments and sheets aligned with the flow direction. The shape of these lamellae is illustrated in **Figure 5.2**. In enhanced oil recovery these lamellae can be used to mobility control since they effectively reduce the permeability of pores to injected fluids.

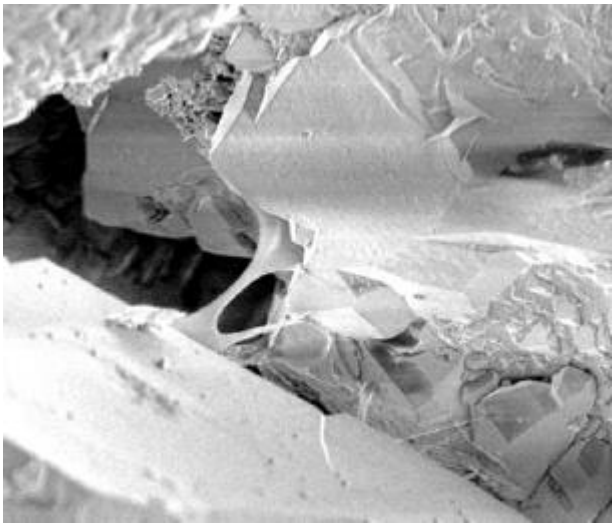

Figure 5.2: Low-energy scanning electron microscopy (SEM) picture of Berea sandstone pore with polymer enhanced foam lamellae obtained from anionic surfactant in the central part of the picture. In the lower right-hand of the picture multiple thin foam filaments can be seen (Kutay and Schramm, 2004).

6. In-situ Image Techniques

In this thesis the two in-situ imaging techniques x-ray computed tomography (CT) and positron emission tomography (PET) are used to obtain high spatial resolution images of events in the sand pack interior. CT can be used to characterize the internal structure of a porous sample without causing damage to the sample (Watanabe et al., 2011). Information obtained from CT-scanning can be used to decide the saturation and porosity in a porous sample (Withjack, 1988). PET can visualize in-situ fluid flow in a porous sample (Khalili et al., 1998, Fernø et al., 2015). The physics behind the two techniques are briefly discussed below.

6.1 X-ray Computed Tomography (CT)

A medical CT scanner, originally developed for clinical use, was utilized to characterize the sand packs in this thesis. Based on the use of an X-ray source and a series of detectors in X-ray computed tomography (CT) the technique can provide images that map the attenuation variation of the X-ray signal through a sample. The measured attenuation through a sample is dependent on the density of the sample. In **Figure 6.1** a schematic illustration of scan geometry where a rotating X-ray source emits radiation and detectors on the opposite side measure attenuation through the sample, which is the most common scan geometry for medical CT-scanners. Measuring the attenuation from a single angular orientation is referred to as a view. A two dimensional slice of the sample is obtained by combining multiple views from different angular orientations of the sample (Ketcham et al., 2001).

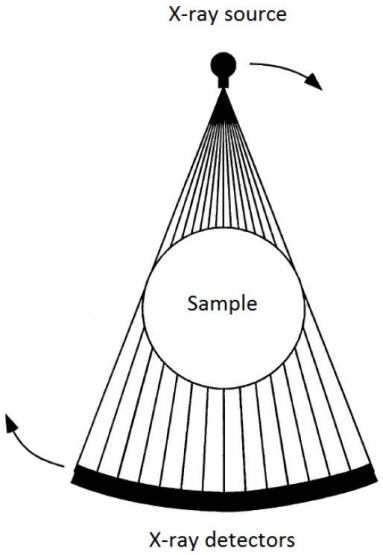

Figure 6.1: Schematic illustration of the X-ray Computer Tomography (CT) scan rotate–only geometry (Lie, 2013) modified from (Ketcham et al., 2001).

The emitted X-ray that passes through a sample is attenuated by scattering and adsorption. Beer- Lambert law describes the X-ray attenuation from monochromatic rays passing through a homogenous sample (Ketcham et al., 2001):

$$I = I_0 e^{-\mu_a x} \tag{6.1}$$

where I is the intensity after the X-ray have passed through the sample, I_0 is the intensity of initial X-ray , μ_a is the linear attenuation coefficient for the scanned sample and x is the thickness of the sample. The CT images are reconstructed by finding the linear attenuation coefficients for all the volume elements of the sample and mathematically converting them into corresponding CT values (Withjack, 1988). The CT value is dependent on the density of a sample. The CT value increases with increased density (Watanabe et al., 2011). In a final gray scale CT image the light areas indicates high attenuation or high CT value, whereas the darker areas indicate low attenuation or low CT value (Coles et al., 1995).

6.2 Positron Emission Tomography (PET)

In this thesis PET, firstly developed for medical diagnosing, is used to investigate the saturation development of surfactant+polymer solution during polymer enhanced foam by co-injection into a sand pack. PET utilizes emitted radiation from radioactive isotopes, called tracers, which can label a specific phase in a multi-phase flow system by adding it to the injected phase. The radioactive isotope decay through emission of positron and produces two photons emitted in opposite directions. A detector measures the radioactive and the tracer activity can be determined (Chaouki et al., 1997). Radioactive decay is process where an atom loses energy to reach a more favorable energy state by emitting alpha particles, beta particles, neutrons or gamma ray photons. Beta decay occurs when a proton rich atom reaches stability by converting a proton to an uncharged neutron by releasing a positive charged particle called positron. Simultaneously an electron is emitted from the atom to balance charge. The positron is an anti-particle to the electron that has the same mass and equal but opposite charge. The positron loses kinetic energy due to interactions with nearby matter and eventually the positron comes to rest and collide with an electron consequently annihilate each other. During the annihilate processes two gamma rays (photons), with energy of 511 keV each, are emitted in almost opposite directions from each other. The two emitted gamma rays form the basis for the PET scanner and decide where the annihilation has occurred. Based on such information from several radioactive decay processes the tracer activity can be found (Valk et al., 2006, Chaouki et al., 1997). PET is suitable image technique to map flow in a porous

media because 50 % of the gamma rays can pass through 11 mm steel (Chaouki et al., 1997). The tracers are produced by nuclear reactions in a cyclotron on site nearby the PET scanner due to limited lifetime of the radioactive isotopes. A cyclotron is a nuclear accelerator (Chaouki et al., 1997). In **Table 6.1** the positron-emitting isotope used to label the surfactant+polymer solution in this thesis are listed with relevant data.

Table 6.1: Positron emitting isotopes (p=proton, n=neutron, d=deuteron (^{2}H)) (Chaouki et al., 1997)

Nuclide	Half-life (min)	Beta decay fraction	Production route
^{18}FDG	110	1	^{18}O (p, n) ^{18}F or ^{16}O (^{3}He, p)^{18}F

The effect of that many gamma-ray couples are not emitted in exact opposite direction from each other coupled with average distance the positron travels before colliding with an electron induce a lower limit of spatial resolution that can be achieved with PET (Valk et al., 2006).

Part 2: Experimental Set-up and Procedures

This part of the thesis lists the materials and fluids used in the experiments. The experimental set-ups and equipment used are described. Preparations and procedures for performing the experiments are presented. **Table 2** presents an overview of the experiments. The majority of the experimental work was performed at The University of Bergen, Dept. of Physics and Technology and one experiment was performed at Haukeland University Hospital, Bergen.

- Sixteen foam coalescence tests.
- Five surfactant foam experiments and seven polymer enhanced foam experiments were performed by co-injection of N_2 gas and surfactant solution and by co-injection of N_2 gas and surfactant+polymer solution, respectively.
- A visualization study of Polymer Enhanced Foam by co-injection was performed by labeling the surfactant+polymer solution with ^{18}FDG.

Table 2: Experimental overview

Material	Experiment type	Location
Graded glass cylinder	Foam coalescence test	University of Bergen, Dept. of Physics and Technology
Sand pack	Surfactant Foam and Polymer Enhanced Foam by co-injection	University of Bergen, Dept. of Physics and Technology
Sand pack	Polymer Enhanced Foam in PET-CT	Haukeland University Hospital, Bergen

7. Foam Coalescence Test

A total of sixteen foam coalescence tests were performed to study foam stability by measuring the half-life of foam in vertical glass cylinders. Throughout the tests the surfactant solution (0.04 wt % in 10 wt % NaCl) volume (1.5 cm) was held constant and oil volume and oil type were varied to study the effect oil have on foam stability. **Table 7.1** lists an experimental overview.

Table 7.1: Experimental overview of the foam coalescence tests

Test	Oil type	Oil volume [cm]
1	-	0.0
2	n-Decane	0.1
3	n-Decane	0.2
4	n-Decane	0.2
5	n-Decane	0.2
6	n-Decane	0.2
7	-	0.0
8	-	0.0
9	n-Decane	1.0
10	n-Decane	1.0
11	n-Decane	0.1
12	n-Decane	1.5
13	n-Decane	3.0
14	Crude oil	0.1
15	Crude oil	1.5
16	Crude oil	3.0

7.1 Fluid Properties

Table 7.2 lists the fluid properties used in the foam coalescence tests. The surfactant solution was specially made to perform the foam coalescence tests. Brine was first prepared and mixed with an alpha olefin sulfonate (AOS $C14_{-16}$) to make a foaming surfactant solution. Different oils were used to compare the effect on foam stability. N_2 gas was used to generate foam.

Table 7.2: Fluid properties of surfactants, oils and N_2 gas at experimental (lab) conditions

Fluid	Content	Density[1)] [g/ml]	Viscosity[1)] [cP]	Condition
Surfactant	Distilled water 10 wt % NaCl 0.04 wt % Petrostep C-1 (AOS C_{14-16})	N/A	N/A	1 bar, 25 °C
n-Decane	$C_{10}H_{22}$	0.726	0.848	1 bar, 25 °C
Crude oil	N/A	0.778[2)]	N/A	1 bar, 25 °C
N_2 gas	>99.999 % N_2	0.001	0.017	1 bar, 25 °C

[1)] Density and viscosity values are gathered from (Lemmon E.W. , 2016). [2)] Values measured in the laboratory.

7.2 Materials

The half-life and stability of foam was studied through a transparent glass cylinder, see **Figure 7.1.** The total length of the glass cylinder was 50 cm and the inner diameter was 20.4 mm. Both ends of the glass cylinder consisted of a part with glass screw threads with inner diameter of 18mm. 3 cm from the inlet (bottom) a 3 mm thick porous glass filter was placed with pore size in the range 40-100 µm. A centimeter scale that starts from the porous frit ranging from 0-40 cm was imprinted in blue on the glass cylinder.

Figure 7.1: Glass cylinder with centimeter scale and fitted porous frit. The length was 50 cm and inner diameter was 20.4 mm.

A inlet Polyformaldehyde (POM) end-piece with 1/8 inch Swagelok male to 1/4 inch NPT , see **Figure 7.2**, was used to connect the glass cylinder to the mass flow controller to supply N_2 gas into the glass cylinder. The POM end-piece has outer diameter of 35 mm and inner diameter of 22.5 mm.

Figure 7.2: Inlet POM end-piece with 1/8 inch Swagelok male to 1/8 inch NPT. The outer diameter was 35 mm and the inner diameter was 22.5 mm.

7.3 Experimental Set-Up and Procedure for the Foam Coalescence tests

This chapter provides a detailed overview of the experimental set-up (see **Figure 7.3**), a list of equipment and the procedure for the foam coalescence tests.

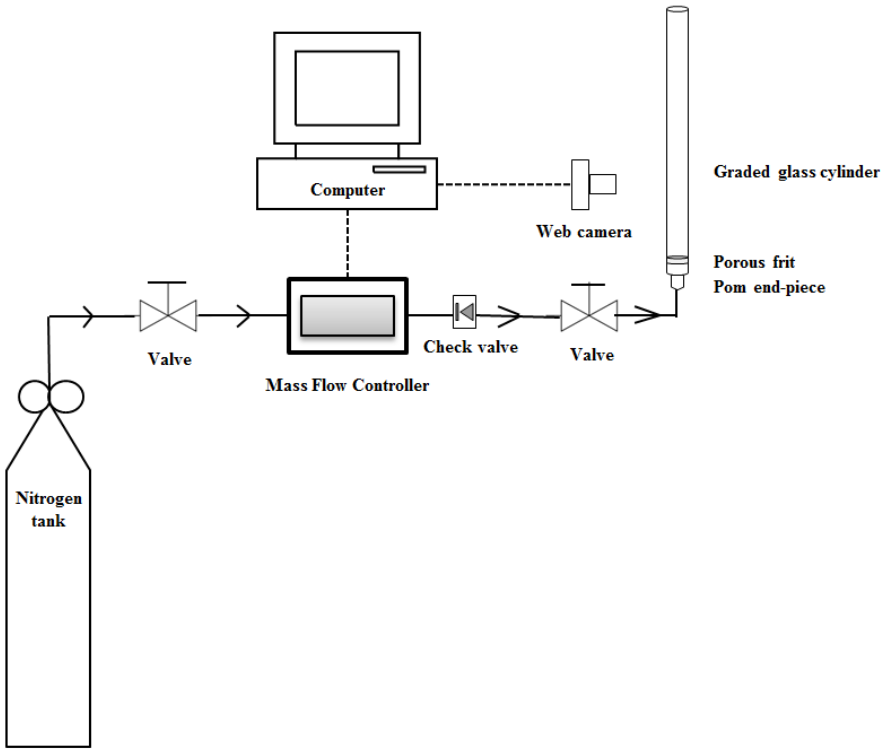

Figure 7.3: <u>Foam Coalescence test.</u> Schematic illustration of the experimental set-up used for the foam coalescence test. The dotted lines from the mass flow controller and web camera indicate data sampling. The arrow points indicate flow direction for N_2 gas.

List of equipment:

- Graded glass cylinder with a porous frit
- A rack to position the glass cylinder vertically
- EL-FLOW Mass Flow Controller Bronkhorst High Tech to control the flow of N_2 gas
- N_2 tank to supply gas through porous frit and generate foam
- Computer to control mass flow rate from N_2 tank
- Check valve to avoid back flow of fluids into mass flow controller
- Plastic tubing, Swagelok valves and fittings
- POM end piece to connect glass cylinder to the mass flow controller
- Thread tape and vacuum grease to avoid leakage between POM end-piece and glass cylinder
- Web camera to monitor foam height in the graded glass cylinder
- Stop watch

7.3.1 Procedure for the Foam Coalescence tests

The foam stability was studied by visual observations and by measuring the foam decay height above the liquid phase as function of time by using the experimental set- up illustrated in **Figure 7.3**. The foam was generated through a porous frit and 1.5 cm surfactant solution in a vertical glass cylinder by injection of 10 ml/min N_2 gas. The specified oil type and amount was poured into the glass cylinder 10 minutes after the surfactant solution. The purpose of this delay was to avoid forming of foam between the surfactant solution and oil. The time for the foam to reach 40 cm was recorded. With 40 cm foam, the N_2 gas flow was chocked and the foam decay height over time was monitored visually and recorded.

8. Surfactant Foam and Polymer Enhanced Foam

The objective was to evaluate the development of pressures during co-injection of N_2 gas and two different foaming solutions, one with and one without polymer added for foam stability. A total of eight sand packs were prepared and fourteen co-injections were conducted during the experimental work in this thesis. An experimental overview is presented in **Table 8.1**. The polymer enhanced foam by co-injection performed in sand pack SP7 is discussed in detail in chapter 8.5.

Table 8.1: An experimental overview of the co-injections

Sand pack name	Co-injection type
SP1	-
SP5	Surfactant Foam
SP5	Surfactant Foam
SP6	Surfactant Foam
SP6	Surfactant Foam
SP6	Surfactant Foam
SP2	Polymer Enhanced Foam
SP3	Polymer Enhanced Foam
SP4	Polymer Enhanced Foam
SP4	Polymer Enhanced Foam
SP4	Polymer Enhanced Foam
SP5	Polymer Enhanced Foam
SP5	Polymer Enhanced Foam
SP7	Polymer Enhanced Foam
SP8MAF[1)]	Polymer Enhanced Foam

[1)] *Experiment performed by Associated Professor Martin Fernø.*

8.1 Fluid Properties

The fluid properties at experimental conditions are listed in **Table 8.2**. Brine was prepared and degassed for 10 minutes before mixed with a surfactant to make the surfactant solution. The foaming solution with surfactant + polymer was prepared by first mixing brine and then the polymer was mixed in overnight. The surfactant was added and mixed in after degassing the polymer solution for 10 minutes.

Table 8.2: Fluid properties of brine, surfactant solution, surfactant + polymer solution and N_2 gas at experimental conditions

Fluid	Content	Density[1)] [g/ml]	Viscosity[1)][cP]	Condition
Brine	Distilled water 20 g/L NaCl	1.01[2)]	1.09[3)]	25°C,1bar
Surfactant	Distilled water 20 g/L NaCl, 1,52 g/L Steol CS-330 HA (Anionic surfactant)	N/A	N/A	25°C,1 bar
Surfactant + polymer	Distilled water 20 g/L NaCl, 1,52 g/L Steol CS-330 Ha (anionic surfactant) 270ppm SNF Floerger FA920 (HPAM)	N/A	N/A	25 °C,1 bar
N_2 gas	> 99.999 % N_2	0.001	0.017	25°C,1 bar

[1)]Density and viscosity data gathered from (Lemmon E.W. , 2016). [2)] Values measured in the laboratory. [3)] Chalk brine viscosity.

8.2 Materials

8.2.1 The Components of the Sand Pack

The sand pack was custom made by the mechanical workshop at the Dept. of Physics and Technology, University of Bergen, and consisted of the following pieces:

- A transparent plastic cylinder with two open ends. The total length of the cylinder was 50.03 cm with an inner diameter of 4.65 cm. Four pressure taps were positioned along the length of the cylinder to measure the fluid pressures along the sand pack, see **Figure 8.1**. From the inlet end of the plastic cylinder the pressure ports are named A, B, C and D. Plastic fittings were used.
- Two POM end pieces with distribution groves to distribute the injected fluids evenly along the sand pack. The POM end pieces were fitted with two O-rings and three 1/8 inch Swagelok male to 1/4 inch NPT inlet/outlet connectors each, see **Figure 8.2**. The length of the POM end pieces were 6.15 cm with diameter of 4.22 cm.
- Stretchy fabric filters were used to avoid sand leakage from inlet, outlet and pressure taps. The filters were placed between POM end-pieces and sand and in the four pressure taps, see **Figure 8.2**.
- Four treaded steel rods to tighten the two POM end pieces across the plastic cylinder and avoid gas or fluid leakage between POM end pieces and plastic cylinder. It was vital that both end pieces are in direct contact with the entire cross sectional area of the sand within the plastic cylinder to avoid fluid leakage.

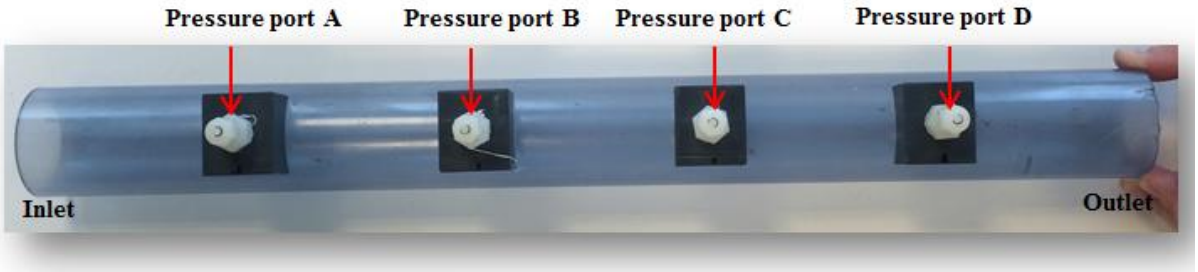

Figure 8.1: Custom made transparent plastic cylinder. Length 50.03 cm, inner diameter of 4.65 cm and both ends open. Four pressure taps were positioned on the cylinder. The pressure taps are named A, B, C and D. Inlet end and outlet end are indicated in the picture.

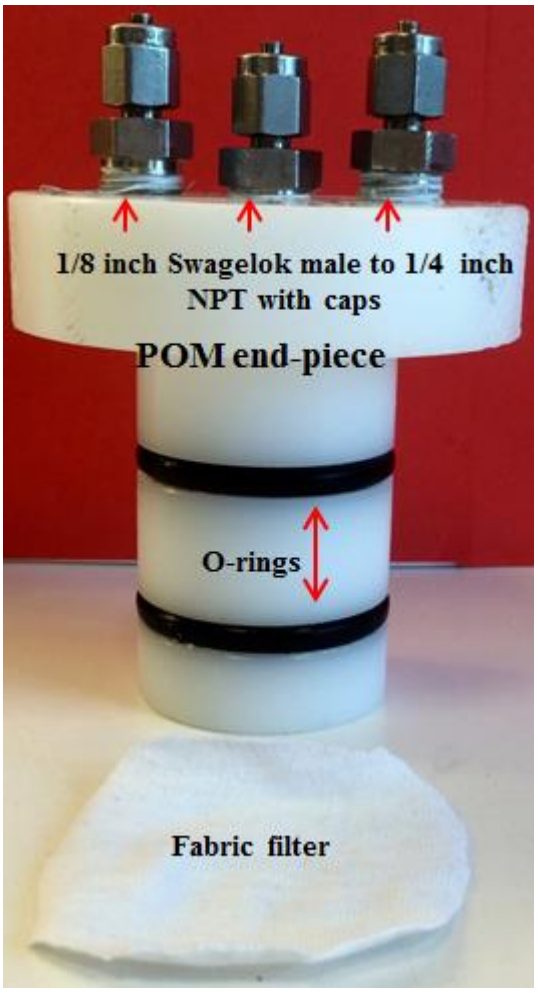

Figure 8.2: POM end-piece and stretchy fabric filter. The POM end piece was fitted with two O-rings and three 1/8 inch Swagelok male to 1/4 inch NPT inlet/outlet connectors. The length was 6.15 cm and the diameter was 4.22 cm.

8.2.2 Sand Grains

Quartz sand with grains size distribution in the range of 212-250 µm was used in the sand packs. The sand grain size range was obtained by sieving < 5000 µm Quartz sand through geological sieves, see **Figure 8.3**. The sand sieving was conducted in collaboration with fellow master student Håkon Kyte Haugland. The final sand grain size distribution was achieved by:

- *Sieving:* Two geological sieves with mesh size 250 µm and 212 µm were stacked on a closed sample collector. 1 dl of sand was hand sieved through the upper sieve (250 µm) and after sufficient time the upper sieve was removed and hand sifting was continued in the 212 µm sieve. Only piled up sand in sieve 212 µm was collected. The sieving process was repeated until enough 212-250 µm sand was collected.
- *Washing:* The collected sand was washed to improve the quality of the sieved sand by removing sand < 212 µm, silt and clay. The two geological sieves and an open sample collector were placed on a rack in a sink. 1 dl sand was first washed by water sprinkling from a shower head through the 250 µm sieve. Secondly the 250 µm sieve was removed and the washing continued for sufficient time through the 212 µm sieve. Sand < 212 µm, silt and clay were flushed through the sample collector and down the drain.
- *Drying:* The sand was dried at 80 °C for 7-10 days in a heating cabinet.

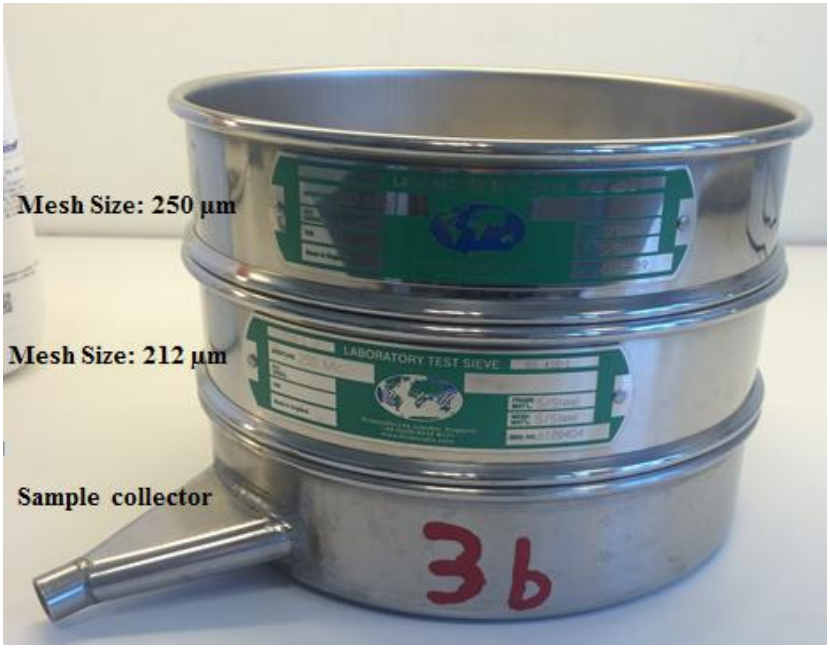

Figure 8.3: Geological sieves. Two geological sieves with mesh size 250 µm and 212 µm stacked on a closed sample collector.

8.3 Sand pack Preparations and Routine Analysis

8.3.1 Packing Procedure

Before packing the sand into the plastic cylinder, the inlet POM end-piece and fabric filter were inserted into the plastic cylinder. Vacuum grease was applied to the O-rings seals prior to the inserting. The sand pack was packed vertically filling it with sequences of 1 cm of sand at the time. Between each 1 cm of sand filling the plastic cylinder was shook and moved back and forth horizontally 20 times to improve packing of sand. Sand was packed from the inlet towards the outlet and was completed when the packed sand column reached 44 cm from the inlet POM end-piece. Then the outlet POM end-piece with fabric filter placed between sand and end-piece was installed. The four pressure taps along the plastic cylinder were closed during sand filling and stretchy fabric was placed in the bottom section of each of them. The two POM end-pieces were held fixed and in positioned by tightening four threaded steel rods placed symmetrically on the outside of the sand pack. An inlet valve was positioned just in front of the inlet POM end-piece and an outlet valve was positioned after the outlet POM end-piece. After each experiment all the parts of the sand pack were disconnected, cleaned with water and dried with air. **Figure 8.4** show a picture of a dry sand pack ready for use. In the picture arrows and colors indicate each position of the pressure ports. The pressure ports are named after distance from the start point of the sand pack. The start point is located at the interface between inlet POM end-piece and sand. Pressure port A (green) was placed 4.3 cm into the sand pack. Pressure port B (purple) was placed 14.3 cm into the sand pack. Pressure port C (turquoise) was placed 24.3 cm into the sand pack. Pressure port D (blue) was placed 33.5 cm into the sand pack.

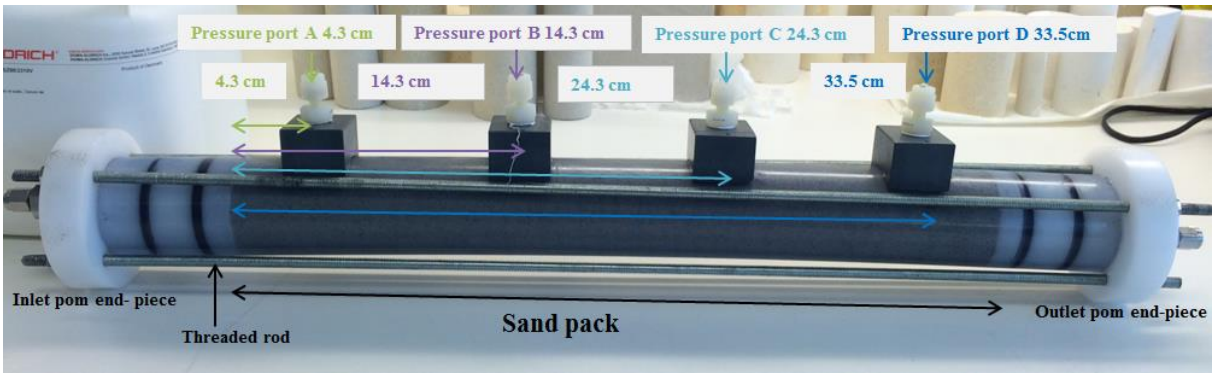

Figure 8.4: <u>Sand pack ready for use.</u> The two POM end-pieces were held fixed and in positioned by tightening four treaded rods placed symmetrically across the sand pack. The pressure ports A (green), B (purple), C (turquoise), and D (blue) were placed 4.3 cm, 14.3 cm, 24.3 cm and 33.5 cm into the sand pack, respectively.

8.3.2 Porosity Measurements

Porosity, $\emptyset$, is defined as:

$$\emptyset = \frac{V_p}{V_b} * 100\% \tag{8.1}$$

where V_p is the pore volume, i.e. the void space between sand grains $[cm^3]$ and V_b is the bulk volume, i.e. the total volume of the sand, $[cm^3]$. Calculating the porosity based on equation (8.1) involves measuring the pore volume and bulk volume of the sand pack in the laboratory.

The saturation method was used to measure the pore volume of the sand packs. The method involves determining the weight of the sand pack before and after brine saturation. The calculated difference in weight corresponds to the total volume of brine that has saturated the sand pack. Assuming the sand pack was 100 % saturated with brine and the density of the brine was known the pore volume, Vp, of the sand pack was calculated from:

$$V_p = \frac{\omega_{wet} - \omega_{dry}}{\rho_{brine}} \tag{8.2}$$

where ω_{dry} $[g]$ is the weight of sand pack before brine saturation i.e. dry, $\omega_{wet}[g]$ is the weight of the sand pack after brine saturation i.e. wet and ρ_{brine} $[g/ml]$ is the density of brine.

The experimental set-up shown in **Figure 8.5** was used to saturate the sand pack with brine in the following procedure:

1) *Vacuuming the sand pack:* All the air was evacuated from the horizontal positioned sand pack by vacuuming it until the pressure was below 600 mTorr. It is vital to get below this pressure to avoid underestimations of the pore volume.
2) *Saturate the sand pack:* During brine saturation the sand pack was positioned vertically. The vacuum pump dragged brine into the vertical positioned sand pack through an open valve positioned below the brine surface in a beaker.

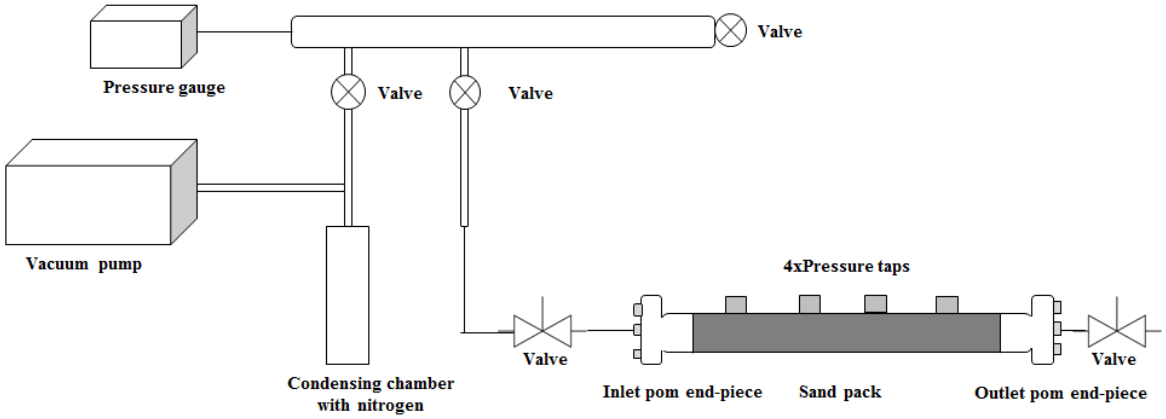

Figure 8.5: <u>Porosity measurements.</u> A Schematic illustration of the experimental set-up used for porosity measurements. The sand pack was vacuumed horizontally and saturated with brine in a vertical position. Liquid nitrogen in the condensing chamber was used to prevent brine for entering the vacuum pump.

8.3.3. Permeability Measurements

Permeability measurements were conducted by injecting brine into the sand pack with various injection rates and the corresponding differential pressure was measured. Assuming that the sand pack was initially 100% saturated with brine, the permeability can be calculated from Darcy's law. The Darcy law is defined as:

$$q = \frac{KA\Delta P}{\mu L} \tag{8.3}$$

where q is the flow rate $[cm^3/s]$, K is the absolute permeability [cm^2], A is the cross sectional area of the sand pack $[cm^2]$, ΔP is the differential pressure across the sand pack [Pa], μ is the viscosity of the fluid [Pa*s], and L is the length of the sand [cm].

Figure 8.6 shows the experimental set-up used for the permeability measurements. A Pharmacia LKP Pump P-500 was used to apply constant volumetric injection rates. Prior to starting the permeability measurements one pressure transducer was connected to the fluid injection line (Inlet) and four pressure transducers (A, B,C,D) were connected to the pressure ports along the sand pack via brine filled tubing. One by one the five tubes were filled with brine by injecting 50 ml/h brine while the rest of the system was closed. The connected pressure transducers at the inlet and at the four pressure ports (A, B, C, D) along the sand pack were used to log the corresponding differential pressure. A total of 11 flow rates were used by first increasing the flow rate stepwise after stabilization of differential pressure and then reversing it by going backwards from the highest flow rate (400ml/h) to the initial flow rate (20 ml/h). The measured differential pressures were plotted as function of q and a trend line was fitted through the data points. Based on the plotted linear trend line and Darcy's law (8.3) the permeability was calculated.

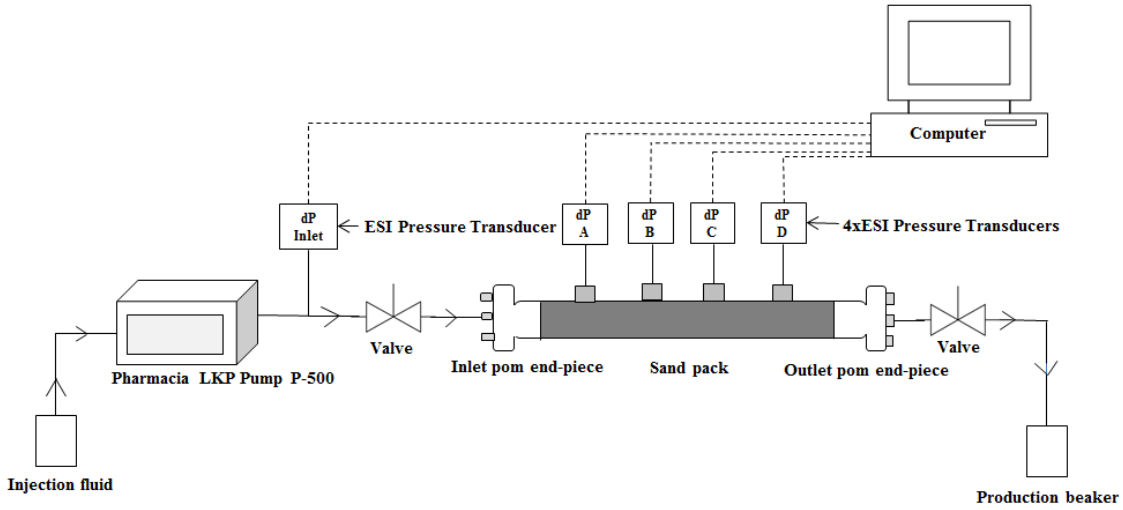

Figure 8.6: <u>Permeability measurements.</u> A schematic illustration of the experimental set-up used for permeability measurements. The dotted lines from the five ESI pressure transducers indicate data sampling. The same set-up was used to satisfy adsorption of surfactant and polymer on the sand grains as explained in section 8.3.4.

8.3.4 Adsorption

Prior to conducting the surfactant co-injection or the surfactant+polymer co-injection experiments, the sand packs were pre-flooded with 2 PV of the appropriate foam agent (surfactant solution or surfactant+polymer solution) to satisfy adsorption of surfactant and polymer on the sand grains. Note that during surfactant+polymer 2 PV of each fluid was injected, 4 PV in total. It is important to satisfy adsorption to avoid that the experimental results obtained from the co-injections are affected by unwanted mechanisms of surfactant loss and polymer loss due to adsorption on the sand grains and retention by the porous medium. A lower surfactant concentration due to loss of surfactants can reduce the foaming ability of the surfactant solution, the surfactant+polymer solution as well as the stability of the foam. Completely or partial removal of polymer molecules due to interactions with the porous medium can result in a lower viscosity compared to the original surfactant+ polymer solution and hence reduced stability of the foam. The experimental set-up used to satisfy adsorption is shown in **Figure 8.6**.

Sand packs SP4, SP5 and SP6 were used for repeat co-injections during several experiments and followed a slightly different procedure. Three polymer enhanced foam experiments were conducted on SP4. Adsorption was satisfied prior to the first experiment by following the procedure described above. Minimum 5 PV of surfactant + polymer solution was flooded through SP4 at constant injection rate after each experiment to displace N_2 gas to residual saturation. Note that the adsorption is still satisfied even if the gas saturation goes up. Two surfactant foam experiments and two polymer enhanced foam experiments were conducted on SP5. Adsorption was satisfied initially by injecting 2 PV surfactant solution with constant injection rate, followed by injection of 2 PV with surfactant+polymer solution with constant injection. Finally, 2 PV surfactant solution was flooded through SP5 at constant injection rate prior to the first surfactant foam experiments. The experiment was directly followed by a polymer enhanced foam experiment, which again was followed by a foam experiments. The final experiment on SP5 was a polymer enhanced foam experiment. Three foam experiments were conducted on SP6. Adsorption was satisfied prior to the first experiment by following the procedure described above. Minimum 5 PV of surfactant solution was flooded through SP6 with constant injection rate after each experiment to displace N_2 gas to residual saturation.

8.4 Set-Up and Procedure for Surfactant Foam and Polymer Enhanced Foam

This chapter provides a detailed overview of the experimental set-up (see **Figure 8.7**), list of equipment and the procedure for the surfactant foam and polymer enhanced foam by co-injections.

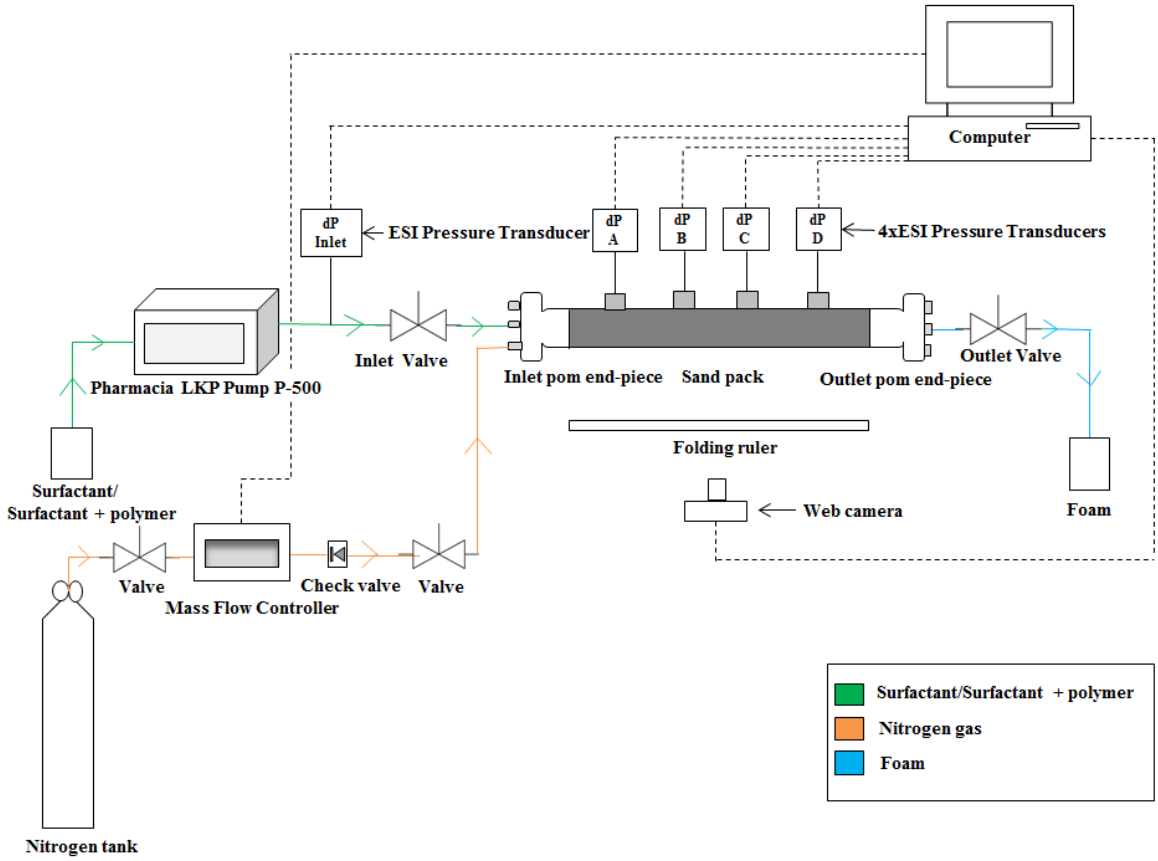

Figure 8.7: <u>Surfactant foam and polymer enhanced foam by co-injection.</u> A schematic illustration of the experimental set-up used for foam and polymer enhanced foam by co-injection. The dotted lines from ESI pressure transducers, mass flow controller and web camera indicate data sampling. The arrow points indicate fluid flow direction. The four ESI pressure transducers along the sand pack are indicated as A, B, C and D.

List of equipment:

- Pharmacia LKP Pump P-500
- EL-FLOW Mass Flow Controller Bronkhorst High Tech for flow control of N_2 gas
- N_2 tank
- 2 x Manometer placed on the N_2 tank
- ESI digital USB pressure transducer, pressure range 0-4 bar
- 2 x ESI digital USB pressure transducer, pressure range 0-2.5 bar
- 2 x ESI digital USB pressure transducer, pressure range -1-2.5 bar
- Computer for pressure logging and operating the mass flow controller
- Swagelok valves, tubing and fittings
- Web camera to monitor N_2 gas front
- Folding ruler to measure the position of N_2 gas front.

8.4.1 Procedure for Surfactant Foam and Polymer Enhanced Foam by Co-injection

This chapter will refer to the experimental set-up as illustrated in **Figure 8.7**. The sand pack was placed horizontally and the mass flow controller and Pharmacia pump was connected to the inlet POM end-piece via two separate fittings. Inlet valve and outlet valve was opened prior to the co-injection and ESI pressure log was started to record the zero pressure and the recorded pressures were calibrated according to this. Polymer enhanced foam by co-injection by N_2 gas and surfactant+polymer solution was conducted at a constant total volumetric injection rate of 200 ml/h, and gas fractional flow was constant at fg=0.9. A production beaker at the outlet collected produced fluids and contained some oil to reduce foam accumulation. The pressures were monitored using five absolute pressure transducers located along the sand pack during the co-injection. The Inlet pressure transducer, was placed 10 cm upstream from the sand pack on the fluid injection line, and the four remaining pressure transducers (A, B, C, D) were placed along the sand pack. A web camera and a folding ruler were used to capture the N_2 gas front position as it propagates through the transparent sand pack before breakthrough. The surfactant foam by co-injection experiments followed the same procedure as the polymer enhanced foam by co-injection experiments, but the foaming solution contained only surfactant.

8.5 Polymer Enhanced Foam Visualized in PET-CT

The medical PET-CT scanner used in this thesis is located at Haukeland University Hospital in Bergen. The PET-CT scanner is primarily used for patients that go through cancer treatment during the weekdays. The objective was to investigate the saturation development of the surfactant+polymer solution labeled with ^{18}FDG during polymer enhanced foam by co-injection into SP7 and correlate it with pressure data. Experiments conducted by the reservoir physics group at UIB are performed during weekends. Two CT scans, 0.6 mm slice and 2 mm slice, were conducted on the dry sand pack SP7 before it was prepared in the laboratory at UIB as described in section 8.3.2, 8.3.4 and 8.3.4 to conduct a polymer enhanced foam by co-injection experiment in the PET-CT scanner. Two CT scans, 0.6 mm slice and 2 mm slice, were conducted on the saturated SP7 before the polymer enhanced foam experiment and PET recording was started. The CT scans with 0.6 mm slice on dry and saturated can be compared and based on density data obtained from these two scans the pore structure can be described and porosity of SP7 can be calculated. PET data alone cannot identify shape and density in SP7. By combining CT scan that has the same resolution as PET (0.2 mm slice) a 3D visualization of SP7 and injected fluid can be created. One co-injection with N_2 gas and surfactant+polymer solution was conducted in the medical PET-CT scanner. Radioactive ^{18}FDG was used as a tracer labeling the injected surfactant+polymer solution during the co-injection.

8.5.1 Experimental Set-Up and Procedure

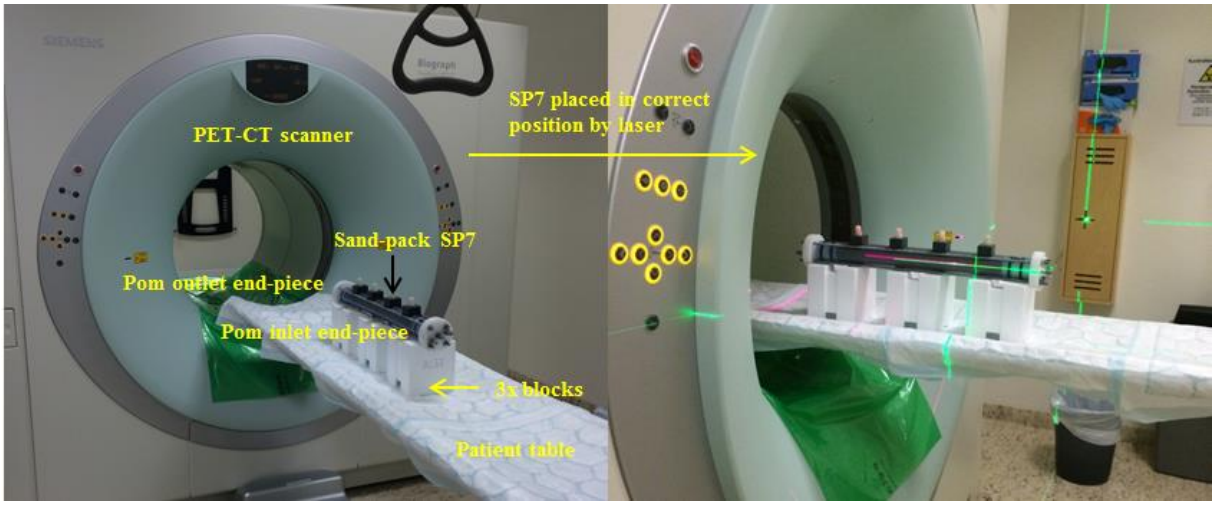

Figure 8.8: CT-scan of dry sand pack SP7. The picture on the left hand-side show SP7 positioned on 3 blocks at the patient table. The picture on the right hand-side show how SP7 was position in the CT scanner by laser.

The experimental set-up used during the polymer enhanced foam by co-injection experiment in the PET-CT scanner was very similar to the other co-injections, see **Figure 8.7**. The sand pack was positioned horizontally on the patient table in the PET-CT scanner as illustrated in **Figure 8.8** along with the mass flow controller, pump and production beaker. The nitrogen tank, beaker with surfactant+polymer solution and computer were placed on the floor next to the PET-CT scanner. The equipment used to conduct the experiment is listed in chapter 8.4 and the Simens Biograph^{TM} True Point^{TM} medical PET-CT scanner was used.

Polymer enhanced foam by co-injection by N_2 gas and surfactant+polymer solution was conducted at a constant total volumetric injection rate of 200 ml/h, and gas fractional flow was constant at f_g=0.9. Immediately after co-injection was started 5.5 ml radioactive ^{18} FDG was mixed into the surfactant+polymer solution. ^{18}FDG was produced in a cyclotron controlled by a radiologist and delivered via pipe network connected to a hot cell located at a separate lab than the PET-CT scanner. The produced ^{18}FDG was delivered to the PET-CT lab in a small vial. The Pharmacia pump injected the radioactive ^{18} FDG surfactant + polymer solution at constant flow rate of 20 ml/h. The pressures were monitored using five absolute pressure transducers located along the sand pack during the co-injection.

Part 3: Results and Discussion

The results from the experimental work are presented and discussed in this part of the thesis. This part is divided into three chapters. Chapter 9 includes visual observations and results from the foam coalescence tests and discussion of the results. In chapter 10 the results from the co-injections with surfactant and surfactant+polymer are presented and discussed. Basic sand pack properties from routine analysis are presented first, followed by individual experimental results and discussions. In chapter 11 the uncertainties related to the experiments will be discussed. The equations used for uncertainty calculations are found in Appendix A.

9. Foam Coalescence Tests

In this chapter the experimental results and visual observations from the foam coalescence tests are presented and discussed. The tests were designed to visually investigate the stability of foam with or without the presence of different oils by measuring the half-life of decay foam height in a vertical glass cylinder. The literature describes that foam stability is the ability foam has to resist bubble collapse and coalescence (Romero-Zeron and Kantzas, 2007). A detailed description of destruction mechanisms and properties affecting foam stability is explained in Section 4.4. The experimental set-up and procedure are explained in chapter 7.3.

9.1 Visual Observations of Foam Stability in the Absences of Oil

Figure 9.1 shows foam decay at 4 different times of a foam column stabilized by surfactant without oil during foam coalescence test 8. The foam was generated up to 21.9 cm in the graded glass cylinder. The images provide visual observations of changes in foam texture and foam height during foam decay and of destruction mechanisms causing reduced foam stability.

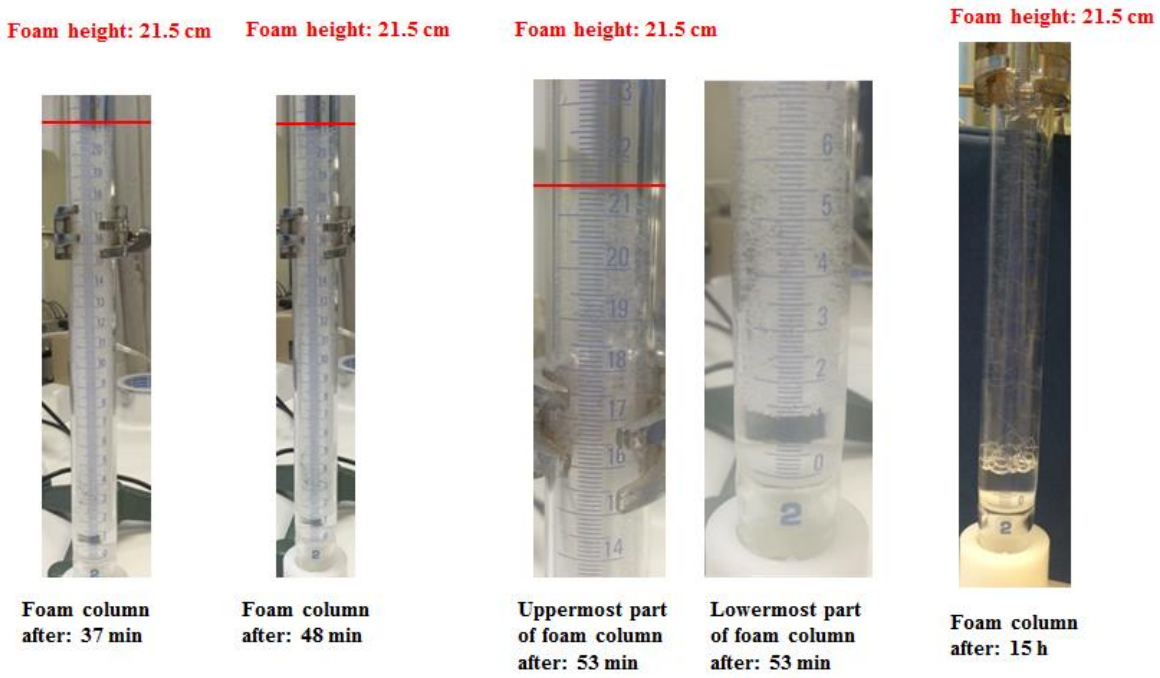

Figure 9.1: Foam decay at different times of a foam column stabilized by surfactant in the absences of oil during foam coalescence test 8.

Foam coalescence test 8 in **Figure 9.1** illustrates the general visual observations obtained from the three foam coalescence tests performed without oil. During in-situ foam generation the foam height increased with a relatively constant rate. After 3 min and 40 seconds the generated foam reached 21.9 cm. Within 16 minutes the initial height of the foam column was changed from 21.9 cm to 21.5 cm. From this stage the foam column remained at constant height (21.5 cm) during the rest of the foam coalescence test (22 hours). Hence, it was not possible to quantify foam stability by measuring the half-life of the foam column height. After 37 minutes the uppermost part of the foam column consisted of dry grey-like foam that could remind of a cobweb. The lowermost part of the foam column consisted of wetter, white foam. After 48 minutes the uppermost part of the foam column still consisted of dry grey-like foam, but was clearly becoming more transparent. The lowermost part of the foam column still consisted of wetter white foam, but was become slightly dryer relatively to after 37 minutes. After 53 minutes the same trend as described above continued and the entire foam column became gradually dryer. The foam texture after 37, 48 and 53 minutes consisted of relatively small bubbles at the bottom compared with the uppermost bubbles. Foam that consist of bubbles of large sizes and with a wide range of bubbles size distribution are expected to become unstable (Lake, 2010, Sheng, 2013a). After 15 hours the foam was divided into two parts. The uppermost part of the foam column consisted of transparent foam with large bubbles indicating unstable foam. The lowermost foam column consisted of wetter foam

compared to the uppermost foam, but it was also transparent and consisted of relatively large bubbles indicating unstable foam. During the next five hours the foam column continued to split up into several parts and the uppermost foam column consisted of dry and big bubbles which gradually disappeared. Based on the three foam coalescence tests without oil two general observations were obtained:

- Foam column have constant height during foam decay.
- Foam decay is caused by liquid drainage indicated by a gradually development of dryer foam.

9.2 Visual Observations of Foam Stability in the Presence of Oil

Foam decay in the presence of two different oils, n-Decane and crude oil, was monitored by imaging foam columns at different times. The effect of the amount of the two oils was also studied during the foam coalescence test. **Table 9.1** lists the thirteen foam coalescence tests that were conducted in the presence of oil. In order to understand foam decay and the destruction mechanism causing reduced foam stability visual observations of changes in foam texture and foam height will be descried next.

Table 9.1: An overview of the foam coalescence tests conducted in the presence of different oils and amount of oils

Test	Oil type	Oil volume [cm]
2	n-Decane	0.1
3	n-Decane	0.2
4	n-Decane	0.2
5	n-Decane	0.2
6	n-Decane	0.2
9	n-Decane	1.0
10	n-Decane	1.0
11	n-Decane	0.1
12	n-Decane	1.5
13	n-Decane	3.0
14	Crude oil	0.1
15	Crude oil	1.5
16	Crude oil	3.0

9.2.1 Visual Observations of Foam Stability with Different Amounts of n-Decane

Figure 9.2 shows foam decay at different times of a foam column stabilized by surfactant in the presence of 0.1 cm n-Decane during foam coalescence test 11.

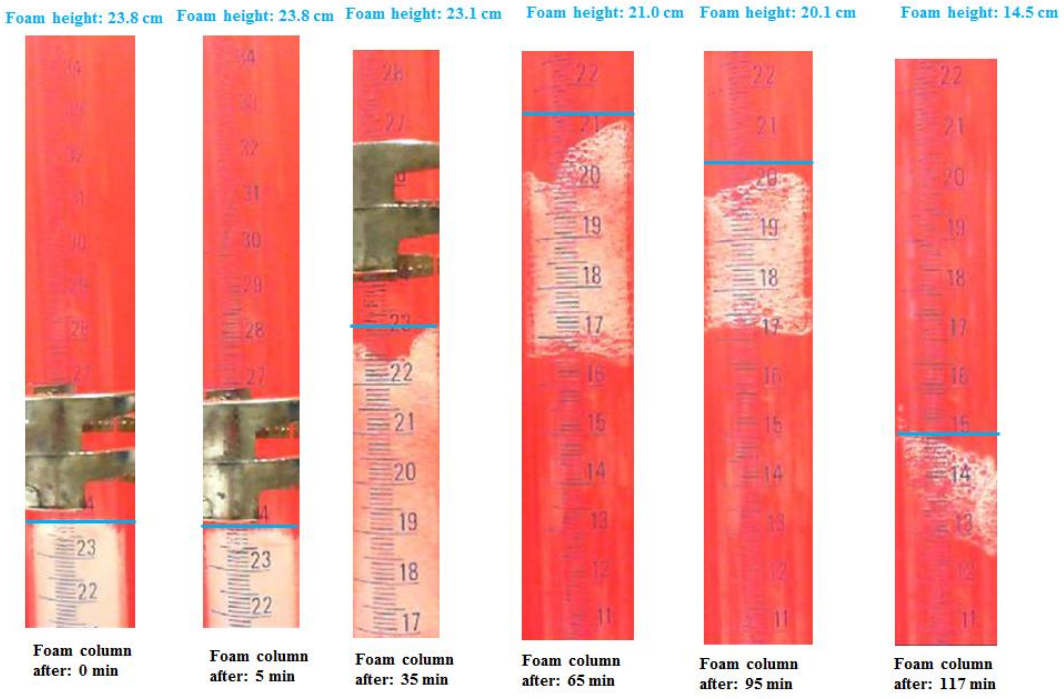

Figure 9.2 (a): Foam decay at different times of the uppermost foam column stabilized by surfactant in the presence of 0.1 cm n-Decane during foam coalescence test 11. The blue lines indicate the uppermost height of the foam column.

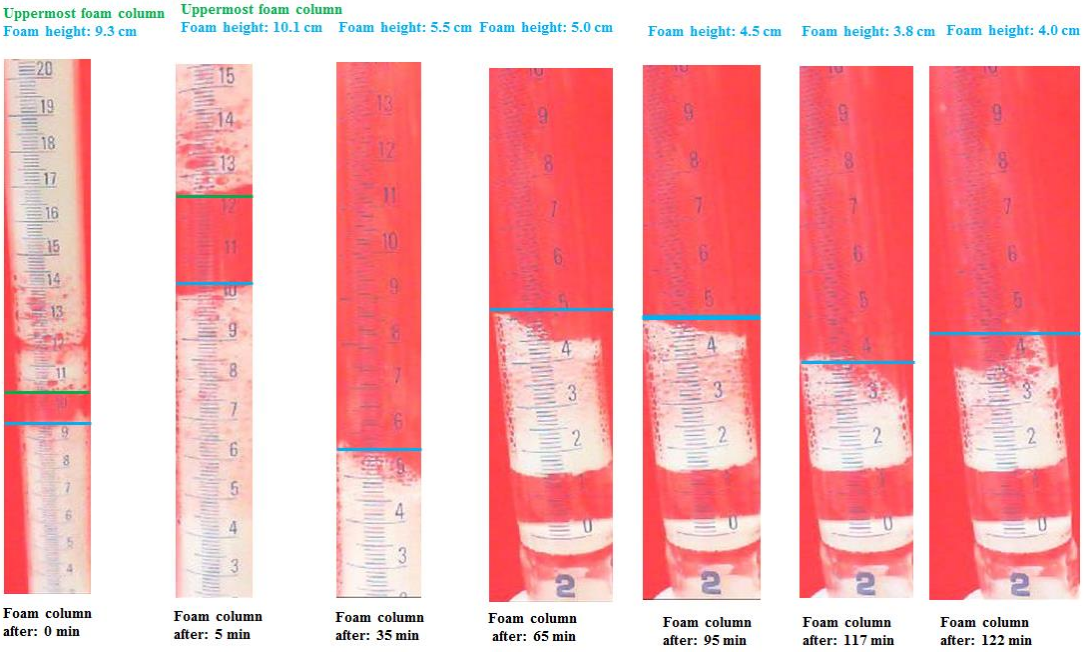

Figure 9.2 (b): Foam decay at different times of the lowermost foam column stabilized by surfactant in the presence of 0.1 cm n-Decane during foam coalescence test 11. Green indicates the lower limit of the uppermost foam column, whereas blue indicates the foam height of the lowermost foam column.

Foam coalescence test 11 in **Figure 9.2** illustrates the general visual observations obtained from the ten foam coalescence tests performed with n-Decane. During in-situ foam generation the foam height increased with a relatively constant rate. After 3 min and 35 seconds the in-situ foam generation was stopped as the foam column was split into two parts. The initial height of the foam column was 23.8 cm. **Figure 9.2 (a)** and **(b)** shows the foam decay at different time steps of the uppermost foam column and of the lowermost foam column, respectively. Both the uppermost foam column and lowermost foam column decayed due to liquid drainage from gravity and bubble collapse. The bubble collapse was probably caused by n-Decane spreading on the lamellae. Liquid drainage was observed as fluid droplets along the glass cylinder that was released from the foam and gravity dragged the foam towards the lowermost foam column. After 122 min, see **Figure 9.2 (b)**, the uppermost foam merged with lowermost foam. After 6 hours and 22 minutes the foam column was completely decayed. During foam coalescence test 11 the foam texture consisted of relatively small and uniform sized bubbles. The results from foam coalescence test 11 illustrate the general behavior of foam decay in the presence of n-Decane. However, some differences are worth mentioning with respect to amount of n-Decane present. The foam was raised with a slower rate as the amount of n-Decane increased and foam column was divided into several parts. After 38 minutes when 1.5 cm n-Decane was present the foam column was divided into three parts, whereas when 3.0 cm n-Decane was present the foam column was divided into three parts after only 23 minutes. In addition, the time it took to reduce foam height to zero was decreased as the amount of n-Decane increased. It took 3 hours and 19 minutes before the entire foam column with 1.5 cm n-Decane entirely collapsed, whereas it took 2 hours and 29 minutes before the entire foam column with 3.0 cm n-Decane collapsed. The foam texture in the presence of 3.0 cm n-Decane consisted of bubbles of different size, at the top of the foam column the bubbles were small compared to those below, whereas in the other tests with less amount of n-Decane the bubbles were relatively uniformed sized. Based on the ten foam coalescence tests with n-Decane present two general observations were obtained:

- Foam column splits into several parts during the foam decay regime.
- Foam collapse due to gravity, liquid drainage and the presence of n-Decane.

Comparison of the foam column stabilized by surfactant in chapter 9.1 with the foam column stabilized by surfactant in the presence of n-Decane indicates interesting differences. The foam column height was constant during the foam decay regime without n-Decane, whereas the height of the foam column with n-Decane decreased. The foam column without n-Decane

decayed due to liquid drainage and was completely collapsed after 20 hours, while the foam column with n-Decane collapsed entirely within 7 hours.

9.2.2 Visual Observations of Foam Stability with Different Oils

Figure 9.3 shows foam decay at different times of a foam column stabilized by surfactant in the presence of 0.1 cm crude oil during foam coalescence test 14. Blue indicates the foam height. Green denotes the lower limit of the uppermost column. Purple indicates a weak zone in the foam column and more specially the area where the foam column first was divided in two during the foam decay regime.

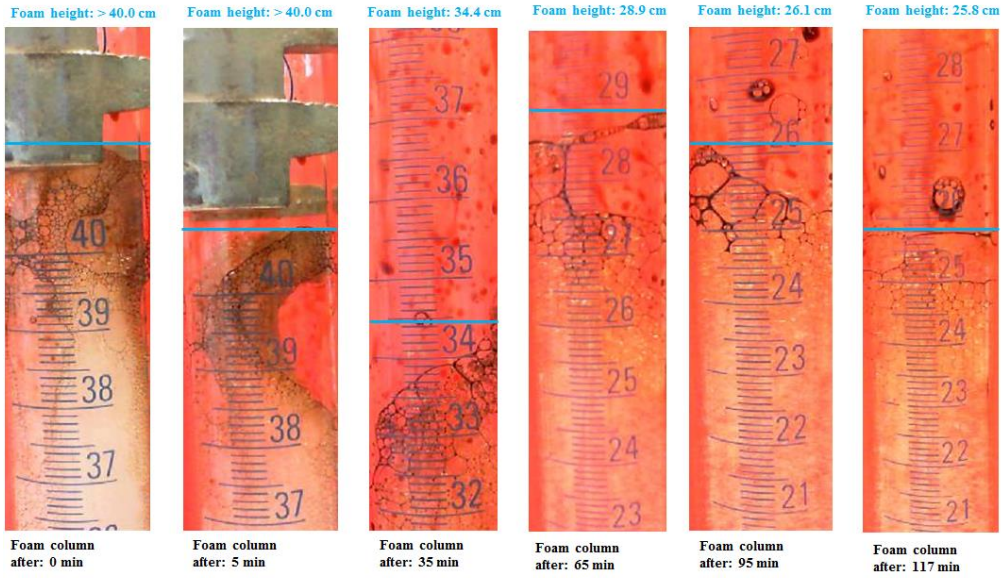

Figure 9.3 (a): Foam decay at different times of the uppermost foam column with 0.1 cm crude oil (test 14). Blue indicates the foam height of the uppermost foam column.

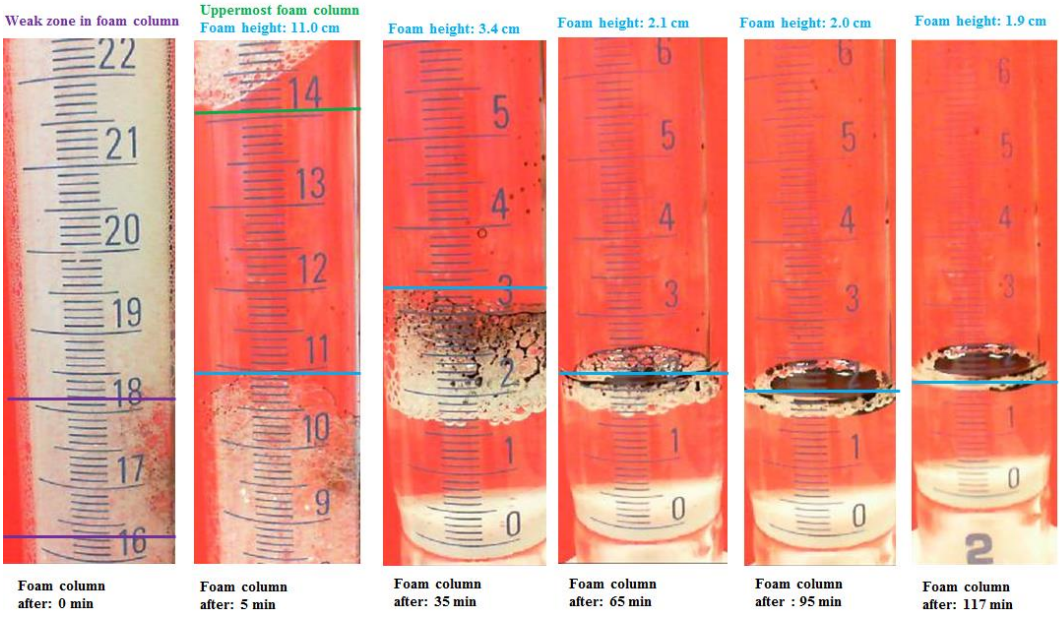

Figure 9.3 (b): Foam decay at different times of the lowermost foam column with 0.1 cm crude oil (test 14). Blue indicates the foam height of the uppermost foam column, purple indicates a weak zone in the foam column and green denotes the lower limit of the uppermost foam column.

Foam coalescence test 14 in **Figure 9.3** illustrates the general visual observations obtained from the three foam coalescence tests performed with crude oil. During in-situ foam generation the foam height increased with a relatively constant rate. After 12 minutes and 35 seconds the generated foam reached 45 cm. The generated foam entered the foam decay regime relatively soon after gas injection was stopped. Within two minutes the foam column was divided into two parts due to bubble collapse. This was initiated by crude oil spreading on the lamellae and will be further discussed below. The foam column was divided into two in the weak zone indicated by purple in **Figure 9.3 (b)** and resulted in gap between the uppermost and lowermost foam column. Further into the foam coalescence test the foam column was divided into three parts. After 1 hour and 40 minutes there were only foam left between 17 cm to 26.1 cm, and this foam gradually collapsed due to gravity and liquid drainage. Liquid drainage was observed as fluid droplets coming out of the foam along the glass cylinder wall. Another factor that might have contributed to reduced foam longevity was the crude oil. It was observed that the crude oil was spreading on the lamellae in the uppermost foam column (**Figure 9.3 (a)**). Crude oil spreading on the lamellae can initiate lamellae rupture and changes in foam texture due to bubble coalescence. **Figure 9.4** shows the foam column after 2 minutes into the foam decay regime and illustrates the differences in foam texture due to the presence of crude oil in the foam texture. The foam texture was characterized with non-uniform bubble size distribution in areas where crude oil were spreading on the lamellae and a narrower bubble size distribution in the areas with no or less crude oil present.

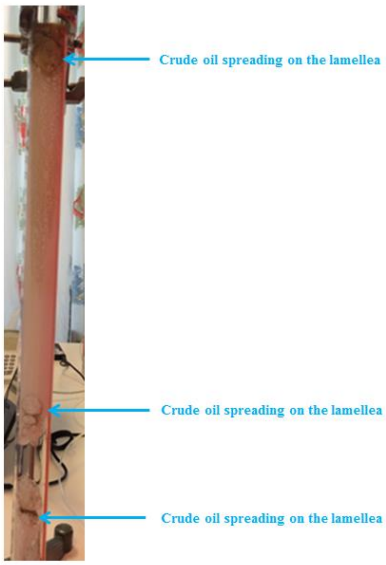

Figure 9.4: Foam column with 0.1 cm crude oil after 2 minutes into the foam decay regime. Blue arrows indicate oil spreading on the lamellae in the foam structure.

The results from foam coalescence test 14 (**Figure 9.3**) show the general behavior of foam decay in the presence of crude oil: the decay rate increased as the amount crude oil present decreased. The overall trend of the foam decay was similar in the presence of n-Decane (chapter 9.2.1) and crude oil based on the visual observations: the foam column was split into several parts during the decay regime and the foam collapsed due to gravity, liquid drainage and the presence of oil. Although n-Decane could not be visually observed (clear color) it is likely that the foam stability was affected by the presence of n-Decane due to increased decay rate compared to the foam column stabilized with surfactant without oil. A second indication that emphasizes the detrimental effect n-Decane has on foam stability was observed during foam generation when the foam column was split in two parts and the foam generation was stopped, see **Figure 9.2 (b)** at t=0 min. The split up of the foam column can have been caused by oil spreading on the lamellae, as identical change in foam texture in the foam column was observed for the foam column in presence of crude oil in **Figure 9.4**.

The decay rate of foam column varied in the presence of the n-Decane and crude oil. Based on the assumption that the foam columns in **Figure 9.2** and **9.3** were continuous, then decay in percentages can be calculated, for instance after 117 minutes. The initial height of foam column stabilized by surfactant in the presence of 0.1 cm n-Decane was 23.8 cm and was reduced by 40.3 % after 117 minutes. The initial height of foam column stabilized by surfactant in the presence of 0.1 cm crude oil was 45 cm and was reduced by 42.7 % after 117 min. The foam column stabilized by surfactant in the presence of 0.1 cm n-Decane was entirely collapsed after 6 hours and 22 minutes, whereas when 0.1 cm crude oil was present it took 5 hours and 30 minutes before all the foam was entirely collapsed. Hence based on comparison of the visual observations in **Figure 9.2** and **9.3** the decay rate was faster in the presence of crude oil compared to n-Decane.

9.3 Quantify Foam Stability by Half-life Measurements

The foam stability can be evaluated during foam coalescence tests by measuring the half-life of the foam height. **Figure 9.5** shows a comparison of the normalized height of five foam columns stabilized by surfactant in the presence of different amounts of n-Decane as a function of time. 0.1 cm n-Decane was present in test 11 and is indicated by red. 0.2 cm n-Decane was present in test 5 and is indicated by green. 1.0 cm n-Decane was present in test 10 and is indicated by grey. 1.5 cm n-Decane was present in test 12 and is indicated by blue. Finally 3.0 cm n-Decane was present in test 13 and is indicated by the purple line. The overall trend for the decay of the normalized height of the five foam columns were that the height

decreased toward t=150 min. The steep drop in normalized height indicates a sudden drop in the foam column height. This result could have been caused by splitting and merging of the foam columns and that the foam column was split into several parts at different time steps as the amount of n-Decane increased as explained in chapter 9.2.1. A second reason can be that only the uppermost part of the foam column height was measured as a function of time despite that the foam column no longer was continues. After t=150 min the normalized height of the five foam columns decreased more slowly which can indicate that all the foam has merged into the lowermost foam column at the bottom of the vertical glass cylinder. In addition, variations with respect to the time it took to reduce the normalized foam height towards zero were observed. It was expected that result in **Figure 9.5** would indicate that the half-life of the foam decay height decreased as the amount of n-Decane increased due the visual observations observed in chapter 9.2.1. It was also expected that the half-life would have been longer for foam columns stabilized by surfactant without oil compared to with oil. This comparison was not possible due to the height of the foam column without oil remained constant during the foam decay regime as explained in chapter 9.1. Comparison of half-life with crude oil and n-Decane was expected to show that the half-life was shorter for crude oil compared to n-Decane based on the visual observations in chapter 9.2.2. With different amounts of crude oil the height of the foam column decreased during foam decay. However, due to splitting of the foam column and difficulties in defining the foam height (see chapter 9.2.2) the comparison of half-lifes was not possible.

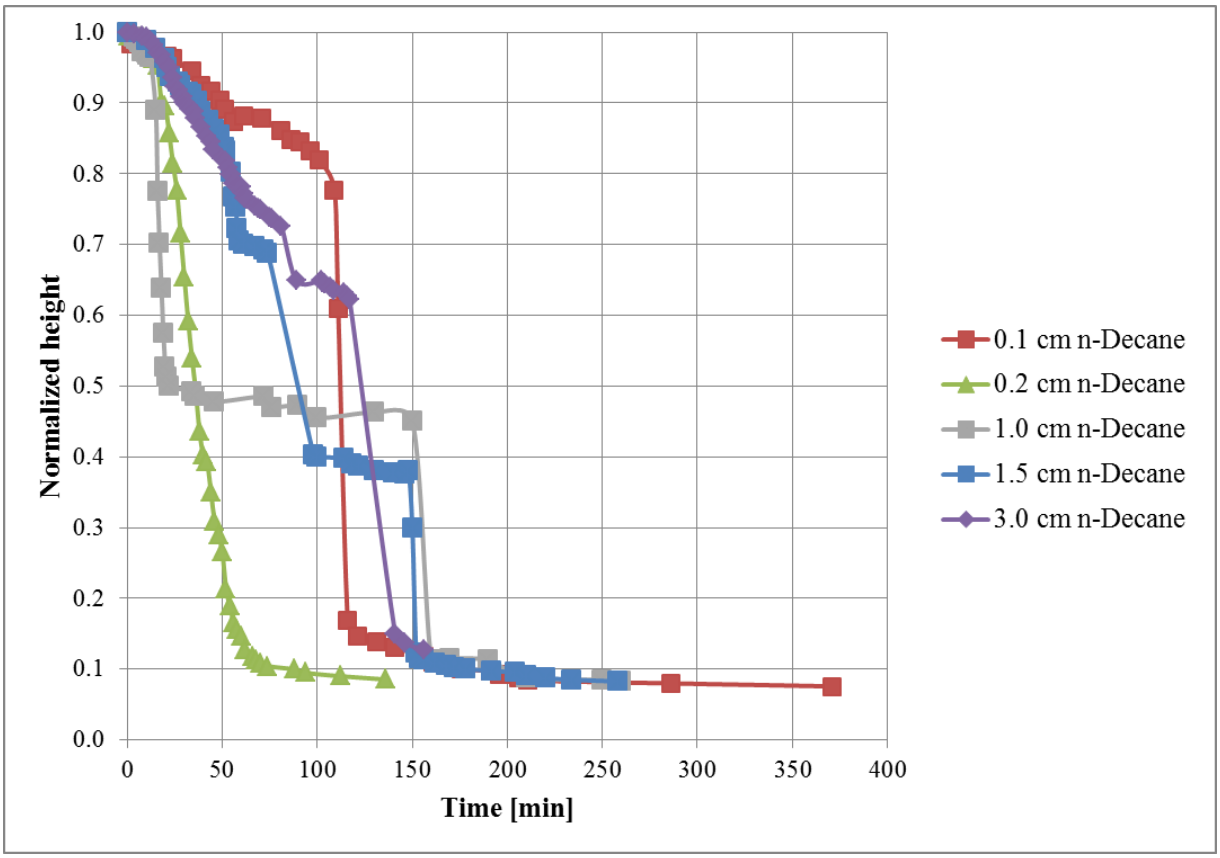

Figure 9.5: Comparison of the normalized height of five different foam columns stabilized by surfactant in the presence of different amounts of n-Decane as a function of time. 0.1 cm n-Decane was present in test 11 and is indicated by red. 0.2 cm n-Decane was present in test 5 and is indicated by green. 1.0 cm n-Decane was present in test 10 and is indicated by grey. 1.5 cm n-Decane was present in test 12 and is indicated by blue. 3.0 cm n-Decane was present in test 13 and is indicated by purple.

Figure 9.6 shows a comparison of the normalized height of two foam columns stabilized by surfactant with 0.1 cm of n-Decane. 0.1 cm n-Decane was present in test 2 and is indicated by green. 0.1 cm n-Decane was present in test 11 and is indicated by red. The decay of the normalized height of the two foam columns with the same amount of n-Decane indicate that the split up of the foam columns was random, but that the decay rate was decided by fixed mechanisms as explained in chapter 9.2.1. The foam column in test 2 was divided into two parts within the first minute, but merged together relatively fast and stayed continuous for the rest of the test (185 min). The foam column in test 11 was divided into two parts after t=5 min. The uppermost foam column height was measured during the foam decay regime. The uppermost foam column merged with lowermost foam column after t=116 min. The foam column remained continuous for the rest of the test (371 min). The decay of the normalized height of the two foam columns were difficult to compare directly, but it was possible to compare the total foam height when the decay rates in the two tests were equal. Between 25-115 minutes the decay rate for both test 2 (green) and test 11 (red) was 0.0002. The total

height of the foam column in test 2 was 7.5 cm at t=25 min, whereas in test 11 the total foam height was 8.9 cm at t=25 min. A similar trend with respect to total foam height was observed between 120 -190 minutes where the decay rate was 0.001 for both tests. The total height of the foam column in test 2 was 3.0 cm at t=120 min, whereas in test 11 the total foam height was 3.5 cm at t=120 min. This indicates that the foam height was proportional to the decay rate.

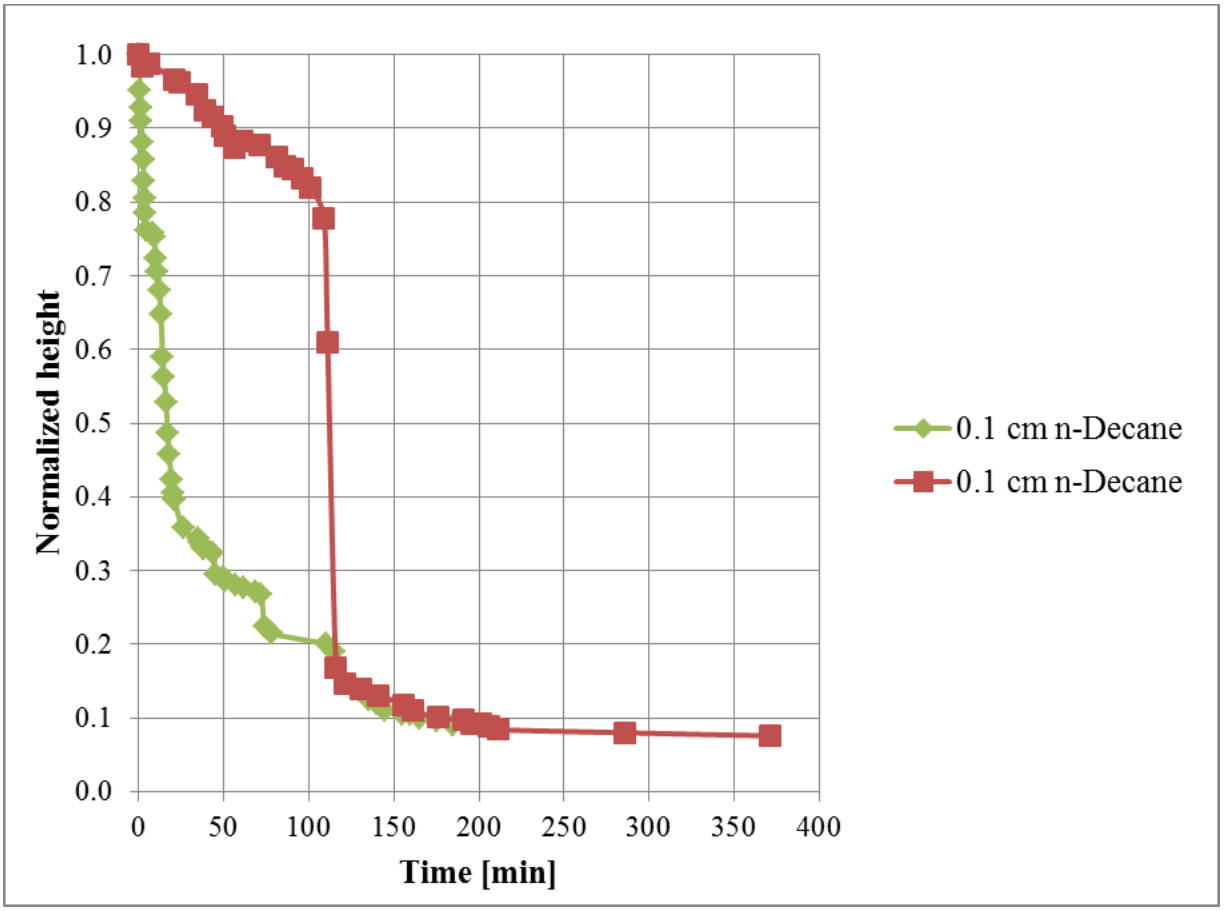

Figure 9.6: Comparison of the normalized height of two different foam columns stabilized by surfactant in the presence of 0.1 cm n-Decane as a function of time.

The initial plan was to test the stability of surfactant foam and polymer enhanced foam in the foam coalescence tests. However, as the results of the half-life measurements of foam height decay could not be quantified, further work in this thesis is focused on foam behavior in unconsolidated sand.

10. Surfactant Foam and Polymer Enhanced Foam

In this chapter the experimental results from surfactant foam and polymer enhanced foam will be presented and discussed. The experiments were performed to evaluate the development of pressures during co-injection of N_2 gas and a foaming solution. The foaming solution contains either surfactant or surfactant and polymer. The purpose was to study in-situ foam generation and foam flow behavior at core scale to evaluate the potential of polymer enhanced foam for IEOR. Two advantages in foam flow behavior are described in the literature (Farajzadeh et al., 2012):

1) Stable displacement front by increasing the viscosity of the displacing fluid that result in a more favorable mobility ratio.
2) Block high permeable zones in the reservoir.

By adding a polymer to the foam system the viscosity of the liquid phase increases, hence, improved foam stability can be obtained (Kutay and Schramm, 2004). Chapter 8.4 explains the experimental procedure in detail. All the experiments were performed in unconsolidated sand packs with a constant total injection rate of 200 ml/h. The foam and polymer enhanced foam were generated in-situ by co-injection of N_2 gas and foaming solution at constant gas fractional flow, f_g =0.9.

10.1 Sand Pack Properties

The basic properties of the sand packs were measured experimentally as described in chapter 8.3. All the sand packs consist of Quartz sand with grain size 212-250 μm and were packed according to the explained procedure in chapter 8.3.1. **Figure 10.1** displays the permeability plotted against porosity. The plot gives a good illustration of the range of properties that exist in the sand packs used in the experiments. The random variations of porosity and permeability within the sand pack are likely caused by heterogeneities. The heterogeneities have probably occurred due to inconsistency during the packing of the sand packs, as the sand packs consisted of sand grains of the same material and size range. A standard procedure for sand packing need to be developed to obtain homogenous sand packs. An advantage with respect to homogenous sand packs is that direct comparison of foam generation and flow behavior can be established. This was however, not the focus of this thesis.

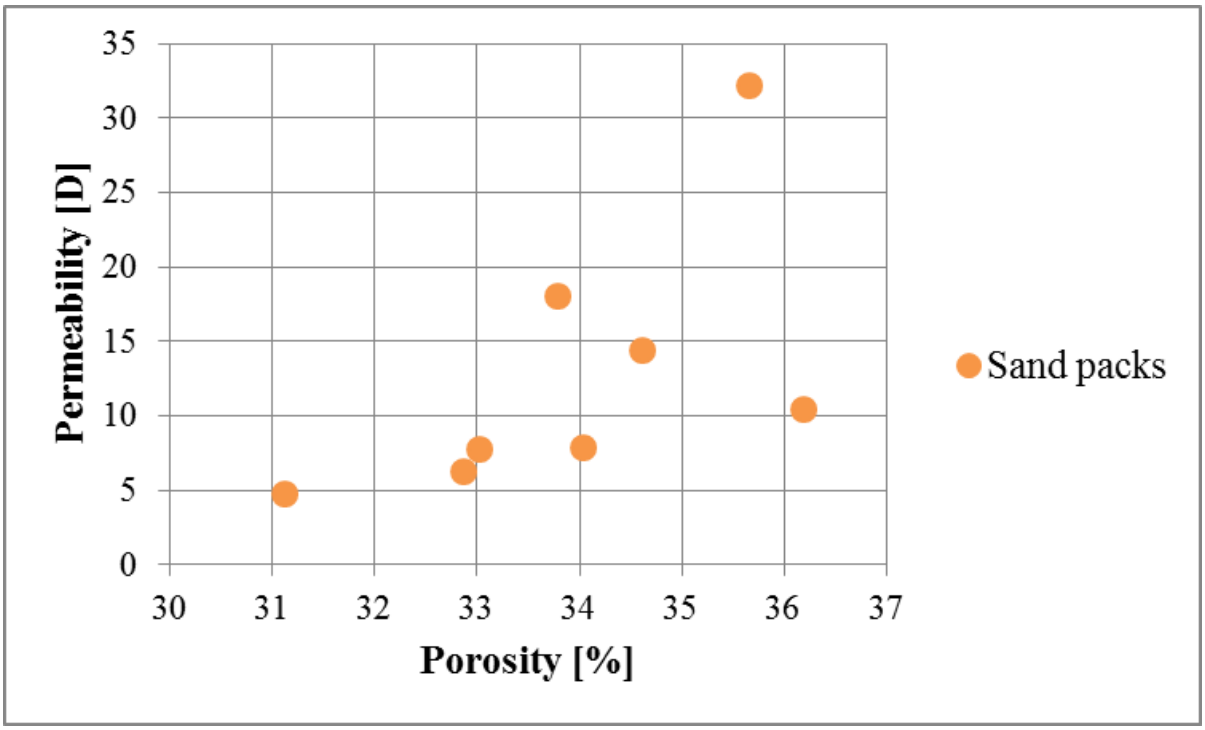

Figure 10.1: The permeability plotted against porosity to compare the sand packs used in the experiments. With respect to permeability there were large variations within the sand pack that ranged from 4.8-32.2 D, whereas the porosity ranged only from 31-36 %.

Table 10.1 lists the estimated properties for the sand packs used in the experiments. The use of different pressure transducers range causes the variations in the listed uncertainties during permeability measurements. **Table A.1** in Appendix A lists the uncertainties in the pressure transducers and will not be further discussed.

Table 10.1: Sand pack data

Sand pack	Length[1)] [cm]	Diameter[1)] [cm]	PV[2)] [ml]	Porosity[3)] [%]	Permeability[4)] [D]
SP1	38.0 ± 0.1	4.65 ± 0.02	233.49 ± 0.1	36.2 ± 0.1	10.40 ± 0.03
SP2	38.0 ± 0.1	4.65 ± 0.02	223.35 ± 0.1	34.6 ± 0.1	14.40 ± 0.05
SP3	37.8 ± 0.1	4.65 ± 0.02	228.89 ± 0.1	35.7 ± 0.1	32.2 ± 0.1
SP4	38.6 ± 0.1	4.65 ± 0.02	215.44 ± 0.1	32.9 ± 0.1	6.3 ± 0.2
SP5	38.2 ± 0.1	4.65 ± 0.02	214.20 ± 0.1	33.0 ± 0.1	7.71 ± 0.02
SP6	38.1 ± 0.1	4.65 ± 0.02	218.63 ± 0.1	33.8 ± 0.1	18.0 ± 0.1
SP7	38.3 ± 0.1	4.65 ± 0.02	221.36 ± 0.1	34.0 ± 0.1	7.91 ± 0.02
SP8MAF	38.0 ± 0.1	4.65 ± 0.02	200.87 ± 0.1	31.1 ± 0.1	4.81 ± 0.02

[1)] Uncertainty listed in table A.1 in Appendix A, [2)]Uncertainties are calculated based on equation A.5 in Appendix A, [3)] Uncertainties are calculated based on equation A.3 in Appendix A, [4)] Uncertainties are calculated based in equation A.11 in Appendix.

10.2 Influence of Permeability

The permeability of the sand packs was experimental measured as explained in chapter 8.3.3. Local heterogeneities caused by permeability variations within the sand packs were observed by calculating the permeability across different sections of the sand packs. How these permeability variations affect foam will be presented and discussed in this chapter. At pore level foamed gas will tend to flow through high permeable and high porosity areas (Apaydin and Kovscek, 2001). Permeability variations in a porous medium can influence the ability foam has to control gas mobility, foam stability and foam generation. Foam reduces the gas mobility more efficiency with higher permeability. This quality improves the ability foam has to control channeling due to permeability variations (Hirasaki, 1989). Foam stability is better in high permeable zone where the lamellae are more stable since the capillary pressure is lower than the critical capillary pressure (Khatib et al., 1988). Foam generation by the snap-off is the most dominant mechanism in heterogeneous porous medium and is dependent on the degree of permeability contrast (Tanzil et al., 2000).

The sand packs were divided into four sections based on the position of the five pressure ports placed along the sand pack. The purpose was to examine the permeability in different parts of the sand pack. **Table 10.2** lists the intervals and length of each interval of the four sections in the sand packs.

Table 10.2: The intervals and length of each interval of the four sections in the sand packs

Section	Location in sand pack	Length of section[1)] [cm]
1	Inlet – A	4.3 ± 0.1
2	A - B	10.0 ± 0.1
3	B - C	10.0± 0.1
4	C - D	9.2 ± 0.1

[1)] Uncertainty listed in table A.1 in Appendix A

Table 10.3 lists the permeability of each sand pack and the permeability in the four sections of each sand pack as defined in **Table 10.2**. The permeability of each of the eight sand packs was calculated by Darcy´s law and by the plotted linear trend line, denoted as K slope, as explained in section 8.3.3. Permeability measurements across section 2, 3 and 4 were not available for SP1, SP2 and SP3 as only two pressure transducers were connected to the sand packs. One pressure transducer was connected to the fluid injection line (Inlet), the other was connected to pressure port A. During the permeability measurements of SP8MAF only three pressure transducers were available and they were connected to the fluid injection line (Inlet), pressure port B and C.

The permeability listed within the different sections of each sand pack differs from each other and this illustrates local heterogeneities within each of the eight sand packs.

Table 10.3: The permeability of each sand pack and the permeability in the four sections of each sand pack

Sand pack	K [D][1)]	K slope [D][2)]	K [D] Section 1[1)]	K [D] Section 2[1)]	K [D] Section 3[1)]	K [D] Section 4[1)]
SP1	10.53 ± 0.04	10.40 ± 0.03	11.7 ± 0.3	N/A	N/A	N/A
SP2	15.0 ± 0.1	14.40 ± 0.05	10.2 ± 0.2	N/A	N/A	N/A
SP3	33.6 ± 0.1	32.2 ± 0.1	12.2 ± 0.3	N/A	N/A	N/A
SP4	5.56 ± 0.02	6.3 ± 0.2	3.6 ± 0.1	19.4 ± 0.6	10.0 ± 0.1	2.98 ± 0.03
SP5	7.49 ± 0.1	7.71 ± 0.02	2.05 ± 0.05	29.1 ± 0.3	17.1 ± 0.2	37.5 ± 0.4
SP6	17.9 ± 0.1	18.0 ± 0.1	13.4 ± 0.3	62.4 ± 0.7	26.7 ± 0.3	20.9 ± 0.2
SP7	11.61 ± 0.05	7.91 ± 0.02	9.4 ± 0.2	25.3 ± 0.3	18.2 ± 0.2	19.9 ± 0.2
SP8MAF	4.81 ± 0.02	4.81 ± 0.02	8.6 ±0.1[3)]	N/A	6.0 ± 0.1	N/A

[1)] Uncertainties are calculated based in equation A.9 in Appendix A. [2)] Uncertainties are calculated based in equation A.11 in Appendix A. [3)] Permeability across Inlet and B and the length of the section was 14.3 cm.

Figure 10.2 shows the permeability as a function of each section for sand pack SP4 (blue), SP5 (red), SP6 (green), SP7 (purple) and SP8MAF (turquoise). The plot illustrates the range of permeability variations within each sand pack. The random distribution of permeability within SP4 (blue), SP5 (red), SP6 (green) and SP7 (purple) indicate local heterogeneities and that the sand packs are not homogenous. The large permeability variations within in each sand pack were probably caused by inconsistency during the packing of the sand packs, as the sand packs consisted of sand grains of the same material and size range. Inconsistency during the packing procedure can have caused areas with tighter packing of the sand grains and areas with void space between the sand grains. The void space can have caused channeling through the sand pack. High conductivity leads to low differential pressure across the area and high permeability, whereas in areas with tighter packing the permeability should be lower. An example of poor packing was observed in SP5 (red) where the permeability in section 1 was 2.05 D, whereas in section 4 the permeability was 37.5 D. This indicates that SP5 (red) was packed tighter in section 1 compared to section 4 and consisted of local heterogeneities. SP8MAF (turquoise) was more homogenous than SP4 (blue), SP5 (red), SP6 (green) and SP7 (purple) due to the fact that variation in permeability between section 2 and 3 was only 2.6 D, whereas the permeability variation between the sections in SP4 (blue), SP5 (red), SP6 (green) and SP7 (purple) were significantly larger. In addition, the permeability (4.81 D) and porosity (31.1%) of SP8MAF (turquoise) were the lowest compared to the rest of sand packs. This indicates that SP8MAF was better packed. The range of permeability variations (2-12 D) was

lowest in section 1 for all the sand packs. This indicates that the packing was better in this section compared to section 2, 3 and 4.

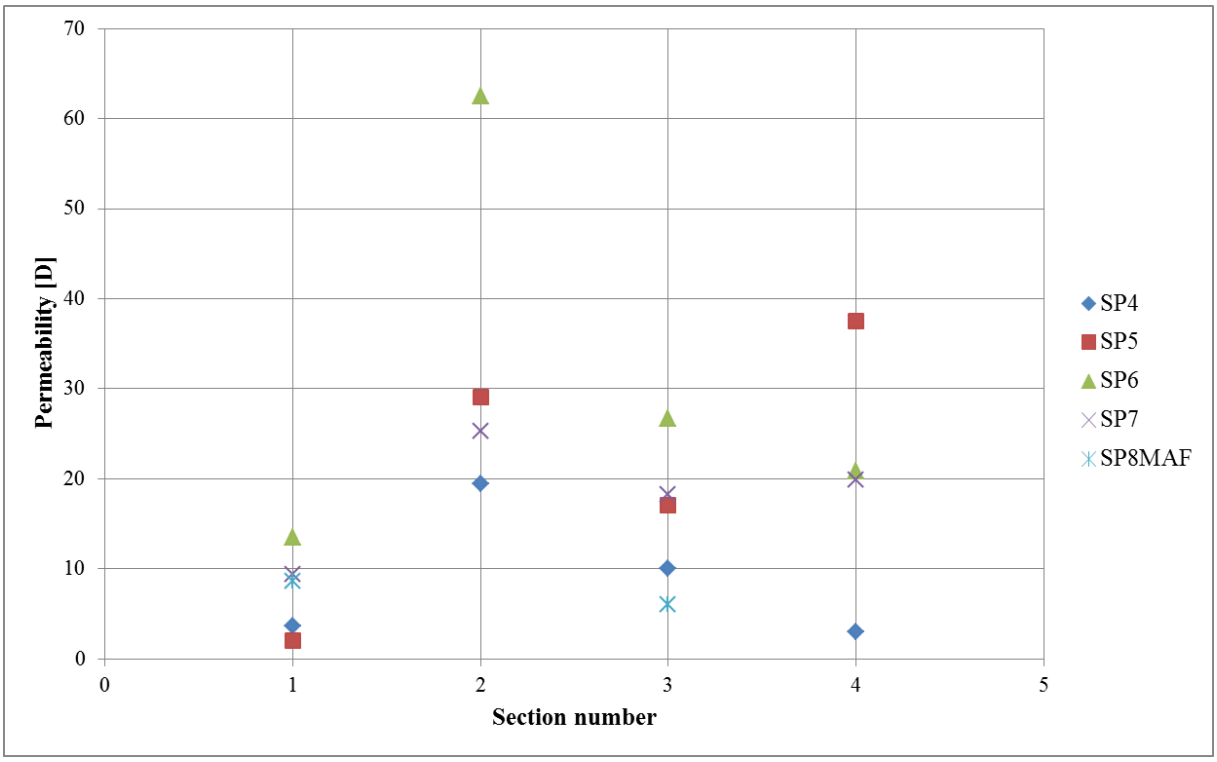

Figure 10.2: The permeability as a function of each section for sand pack SP4 (blue), SP5 (red), SP6 (green), SP7 (purple) and SP8MAF (turquoise) to illustrate permeability variations within each sand pack. Large permeability variations within SP4 (blue), SP5 (red), SP6 (green) and SP7 (purple) and less permeability variations within SP8MAF (turquoise) were observed.

10.3 An Introduction to Surfactant Foam and Polymer Enhanced Foam

A total of fourteen co-injections were conducted in this thesis and are listed in **Table 10.4**. Experimental procedures and details of the experimental set-up are provided in chapter 8.4. Some of the co-injections were less successful due experimental problems and will not be emphasized further in the discussion. The experimental results are however included in Appendix B.

Table 10.4: An experimental overview of the co-injections

Sand pack name	Experiment	Co-injection type
SP5	6	Surfactant Foam
SP5	8	Surfactant Foam
SP6	10	Surfactant Foam
SP6	11	Surfactant Foam
SP6	12	Surfactant Foam
SP2	1	Polymer Enhanced Foam
SP3	2	Polymer Enhanced Foam
SP4	3	Polymer Enhanced Foam
SP4	4	Polymer Enhanced Foam
SP4	5	Polymer Enhanced Foam
SP5	7	Polymer Enhanced Foam
SP5	9	Polymer Enhanced Foam
SP7	13	Polymer Enhanced Foam
SP8MAF[1)]	14	Polymer Enhanced Foam

[1)] *The experiment was performed by Associated Professor Martin Fernø.*

Figure 10.3 shows an example of how the results of the monitored absolute pressures [millibar] are plotted as function of time [PV] at five locations along a sand pack (SP6) in this thesis. The absolute pressures are indicated by name and location with respect to sand pack. Ambient (room) temperature was logged during the experiments (indicated by grey lines in the figures) and varied between daytime and nighttime during the co-injection, but did not affect the results. The behavior of the five measured absolute pressures was that they increased before they decreased and became stable. The development in absolute pressure can provide information about the co-injection and about when or if the system reach stable conditions.

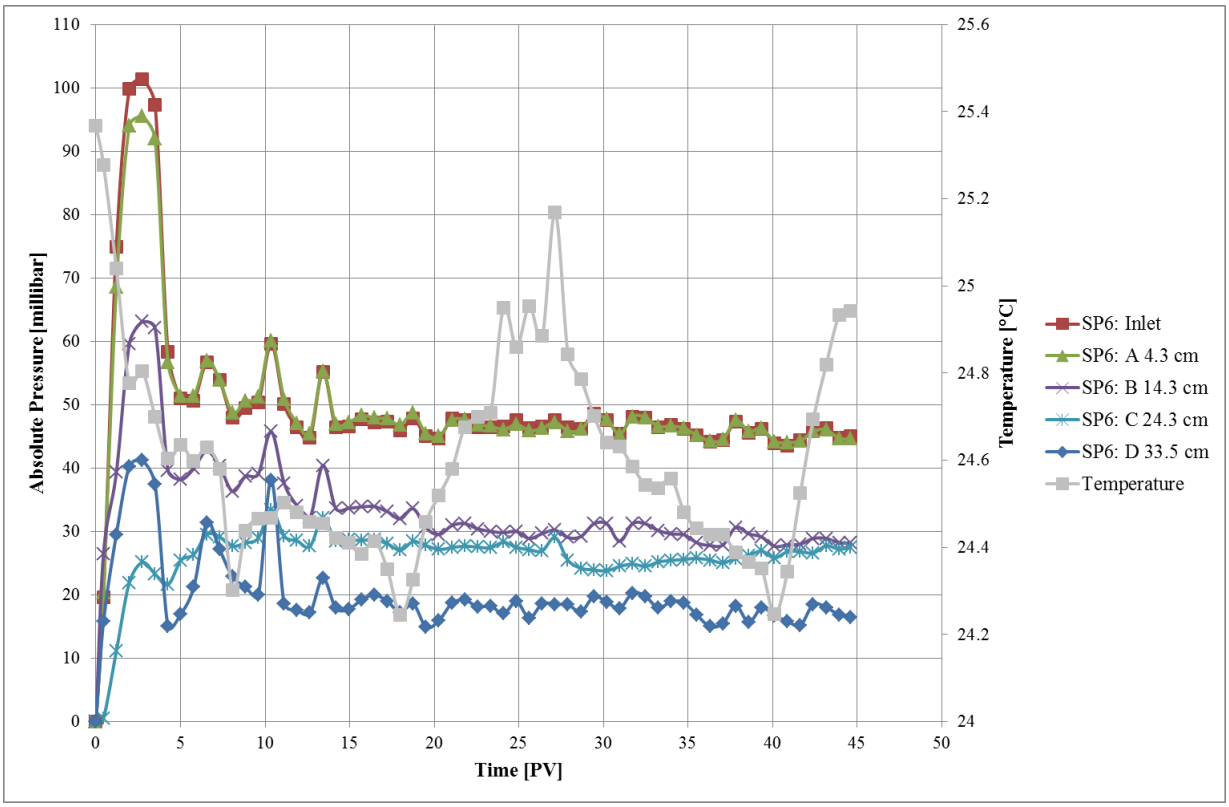

Figure 10.3: Absolute pressures [millibar] as a function of time [PV] measured in five different locations along the sand pack during co-injection into SP6 (experiment 11). The first pressure transducer, named Inlet (red lines) was placed 10 cm upstream from the sand pack on the fluid injection line. Pressure transducer A (green lines) was placed 4.3 cm into the sand pack. Pressure transducer D (blue lines) was placed 33.5 cm into the sand pack and was the pressure transducer located closest to the outlet end. Ambient (room) temperature was logged during the experiment (grey lines).

The sand packs were divided into four sections based on the position of the five pressure ports placed along the sand pack. The purpose was to investigate the development in the pressure gradient across different sections in a sand pack during co-injection. The four pressure gradients were calculated from the absolute pressure measurements in each pressure port. The

four pressure gradients are calculated between pressure ports: Inlet and A, A and B, B and C, C and D. **Table 10.5** lists the location, color code and length of each interval of the four sections in the sand packs.

Table 10.5: The intervals, color code and length of each interval of the four sections in a sand pack.

Section	Location in sand pack	Color code	Length of section[1)] [cm]
1	Inlet – A	Red	4.3 ± 0.1
2	A - B	Green	10.0 ± 0.1
3	B - C	Purple	10.0± 0.1
4	C - D	Blue	9.2 ± 0.1

[1)] *Uncertainty listed in table A.1 in Appendix A*

Figure 10.4 shows an example of how the four calculated pressure gradients [millibar/cm] are plotted as a function of time [PV] in this thesis. The four pressure gradients were calculated from the absolute pressure measurements and represent the sections defined in **Table 10.5**. The behavior of the three pressure gradients across section 1, 2 and 3 was that they increased before they decreased and became stable during the co-injection, whereas the pressure gradient across section 4 decreased before it increased and became stable. During monitoring and investigations of the development in the pressure gradients it is important to notice whether they become stable or not. The stabilization is dependent on the co-injection type and section of the sand pack. The pressure gradients develop differently depending on the section of the sand pack. The shape of the pressure gradient curve can indicate how the foam behaves in unconsolidated sand. Based on the pressure gradients the apparent viscosity of foam in each section across a sand pack can be calculated by Darcy's law (4.6) and be compared.

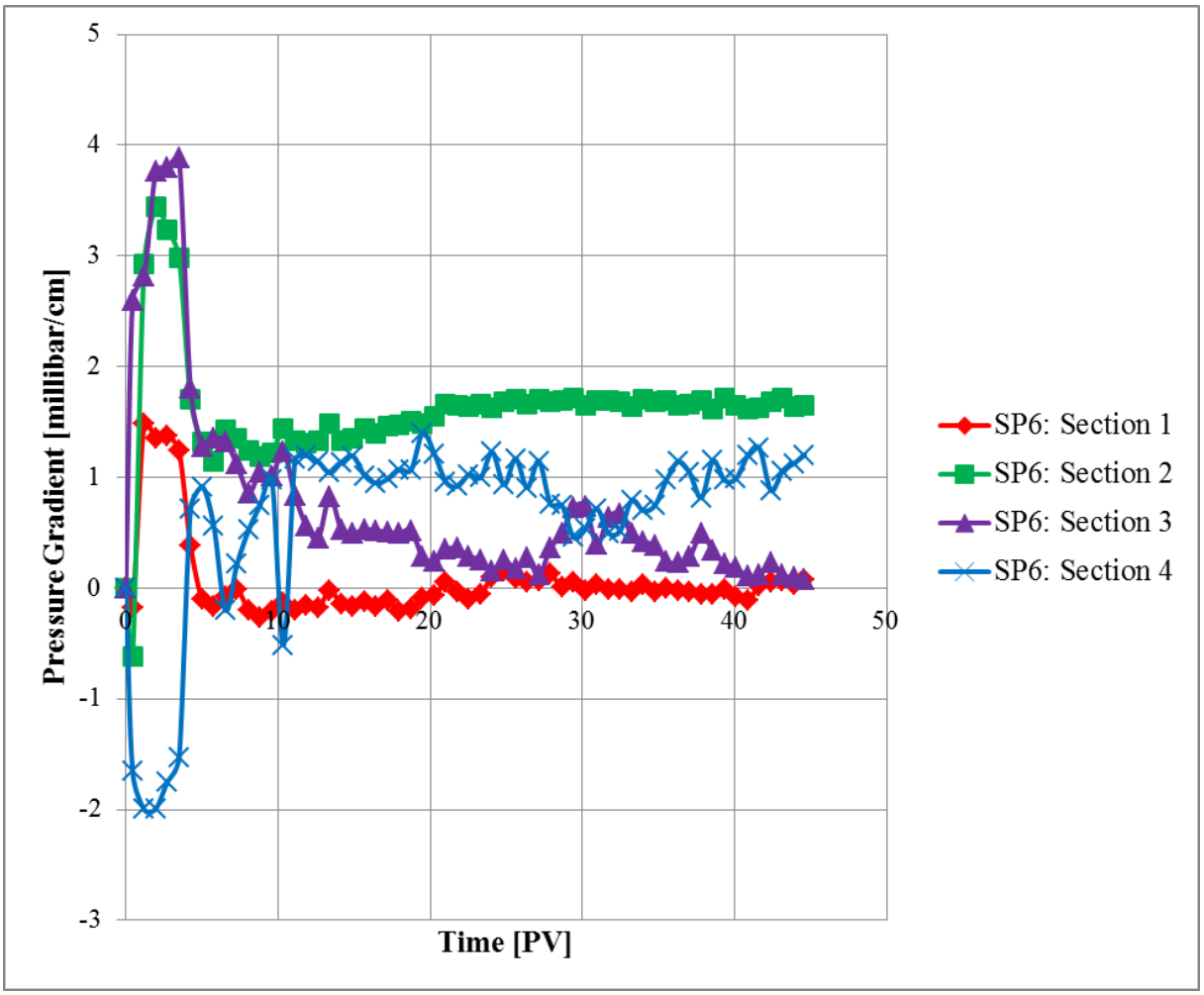

Figure 10.4: The pressure gradient [millibar/cm] across four different locations in sand pack SP6 as a function of time [PV] during co-injection (experiment 11). The four pressure gradients were measured between pressure ports Inlet –A (red), A- B (green), B – C (purple) and C – D (blue) and are referred to as section 1 (red), section 2(green), section 3 (purple) and section 4 (blue), respectively.

The pressure data gathered during the co-injections were logged every tenth second and the experiments were carried out over several days. The result presented in this thesis are smoothed out by first reducing the logged raw data pressures from every 10 seconds to every 600 seconds followed by averaging every five data points.

10. 4 Surfactant Foam by Co-injection

Surfactant foam by co-injections of N_2 gas and surfactant solution were performed to serve as benchmark for the polymer enhanced foam experiments. Sand packs with satisfied adsorption as explained in chapter 8.3.4 were used in the experiments, and some of the sand packs were used for repeat injections during several experiments. The objective was to investigate the development in absolute pressure in each of the five pressure ports placed along the sand pack and the development in the calculated pressure gradient across the four sections of the sand pack during co-injection. The stabilization of absolute pressures at plateau values is of particular interest, and is an important distinction between surfactant foam and polymer enhanced foam as discussed in chapter 10.5. Investigations of the development in pressure gradient across the four sections in a sand pack during co-injection is important, as the literature reports that the transition from weak to strong foam, i.e. foam generation, happens suddenly and is indicated by a strong increase in pressure gradient (Lee and Kam, 2013). Two surfactant foam experiments are presented and discussed in this chapter. For each co-injection, two plots are presented:

- The absolute pressures measured at five specific locations along the sand pack as a function of time
- The calculated pressure gradients across the four sections in the sand pack as functions of time.

Figure 10.5 shows the development in absolute pressures at the various locations during co-injection of N_2 gas and surfactant solution into sand pack SP5 (experiment 6). Pressure development was monitored at five different locations along SP5, using absolute pressure transducers (see chapter 10.3 for details). The absolute pressures measured at all the five locations increased until t=7 PV were reached and a stable value was observed until t=10 PV. After t=10 PV a gradual increase in the absolute pressures at each location along the sand pack was observed toward t=23 PV and the co-injection was ended. The total increase in absolute pressure between t=10-23 PV was 10 millibar at each location in SP5. The small fluctuations in the absolute pressures after t=7 PV may be caused by gas-foam slugs. Alternating production of gas and foam was also observed in the outlet tubing during the co-injection.

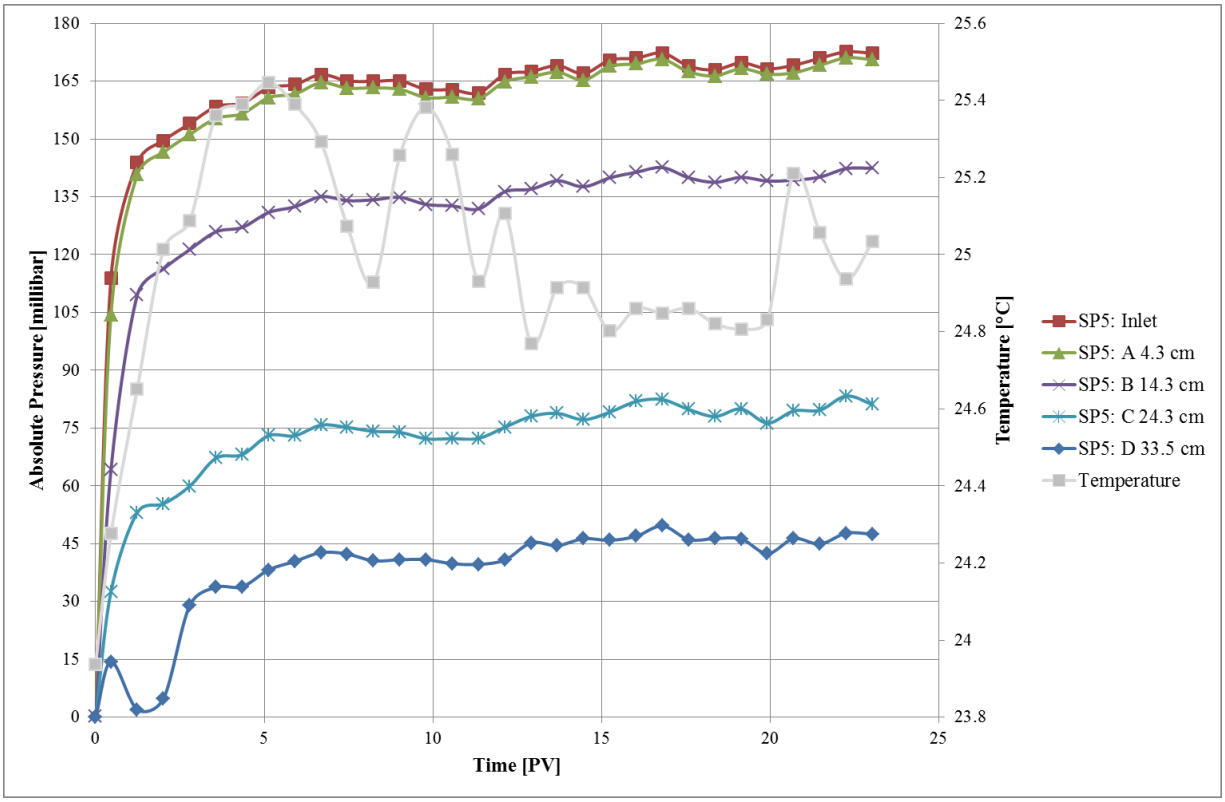

Figure 10.5: Absolute pressures [millibar] as a function of time [PV] measured in five different locations along the sand pack during co-injection into SP5 (experiment 6). The measured absolute pressures increased and reached a stable value at t=7 PV. After t=10 PV the absolute pressures increased.

Figure 10.6 shows the calculated pressure gradient across four different sections in sand pack SP5 during co-injection (experiment 6). The four pressure gradients were calculated from the absolute pressure measurements in each pressure port and represent the sections defined in **Table 10.5**. The pressure gradients across the four sections increased rapidly before they decreased and became stable, which is typical for surfactant foam. The observed fluctuations after stabilization can indicate foam generation. During foam generation some lamellae are created while others are destroyed simultaneously and this process can contribute to fluctuations in the pressure gradient (Ransohoff and Radke, 1988). The stabilized pressure gradient in section 1 (red) was 0.8 millibar/cm at t=1 PV. The pressure gradient in section 2 (green) stabilized at 2.8 millibar/cm at t=1 PV, whereas the pressure gradient in section 3 (purple) stabilized around 6 millibar/cm at t=3 PV. The pressure gradient in section 4 (blue) stabilized around 3.5 millibar/cm at t=3 PV.

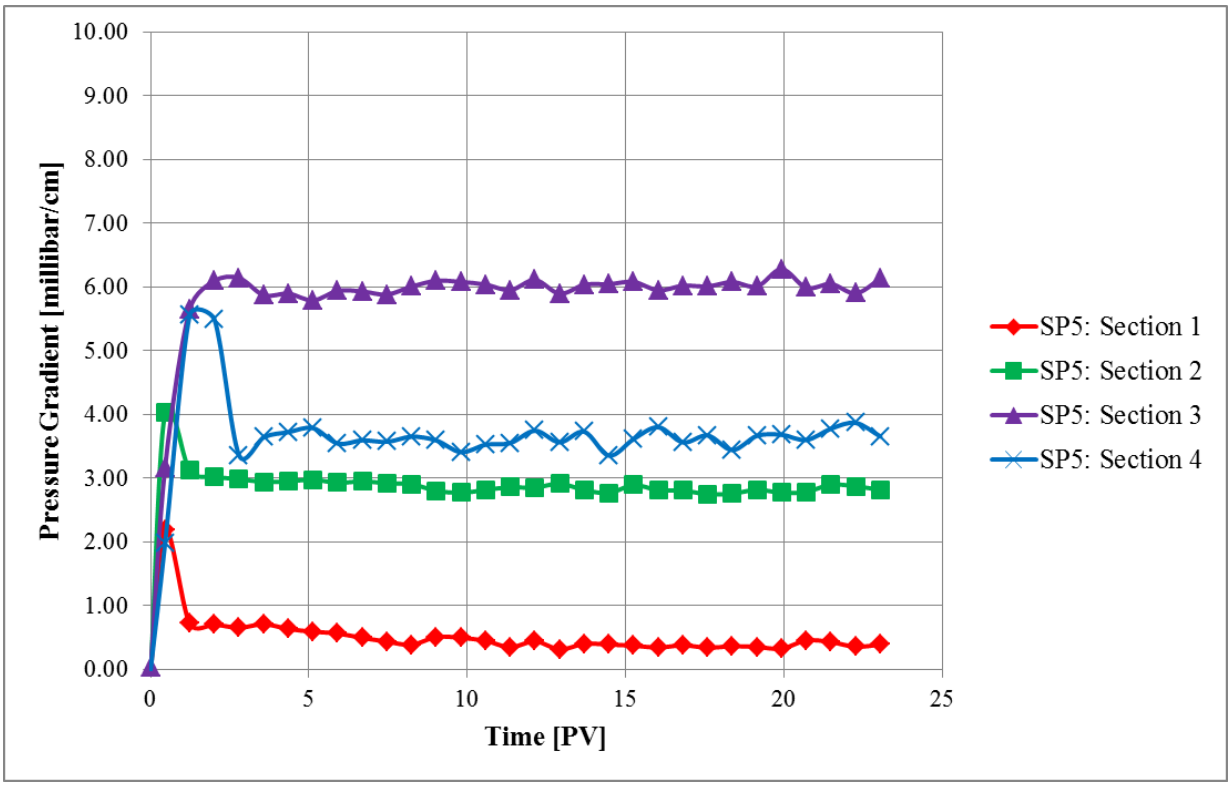

Figure 10.6: The pressure gradient [millibar/cm] across four different locations in sand pack SP5 as a function of time [PV] during co-injection (experiment 6). The pressure gradients across the four sections increased rapidly before it decreased and became stable

The apparent viscosity for surfactant foam was calculated by Darcy's law (4.6) for SP5 to compare flow and foam ability in the four sections. The permeability and the apparent foam viscosity in the four sections across SP5 are listed in **Table 10.6**

Table 10.6: The permeability and the apparent foam viscosity in the four sections across sand pack SP5

Section	1	2	3	4
K [D]	2.05	29.1	17.1	37.5
μ_{app} **[cP]**	0.2	24.7	31.6	41.3

The viscosity of N_2 gas was 0.017 cP and the apparent foam viscosity in the four sections were higher than viscosity from gas only. This indicates that surfactant foam was generated in all four sections across SP5. The apparent foam viscosity in section 2, 3 and 4 were significantly higher than the apparent foam viscosity in section 1. This indicates that stronger foam was generated in section 2, 3 and 4 compared to the generated foam in section 1. In section 1 the pressure gradient stabilized at 0.8 millibar/cm, the permeability was 2.04 D and the apparent viscosity was 0.2 cP. In section 4 the pressure gradient stabilized at 3.5 millibar/cm, the permeability was 37.5 D and the apparent viscosity was 41.3 cP. This indicates that the apparent foam viscosity increased with higher permeability and consequently stronger foam was generated in section 4 compared to section 1. However, stronger foam was generated in section 3 compared to section 2 even though the permeability was higher in section 2 than it was in section 3. In section 2 the pressure gradient stabilized at 2.8 millibar/cm, the permeability was 24.7 D and the apparent foam viscosity was 24.7, whereas in section 3 the pressure gradient stabilized at 6 millibar, the permeability was 17.1 D and the apparent foam viscosity was 31.6 D.

Figure 10.7 shows the development in absolute pressures at five locations during co-injection of N_2 gas and surfactant solution into sand pack SP6 (experiment 12). Sand pack SP6 was previously used for two co-injections of N_2 gas and surfactant solution (experiment 10 and 11). Experiment 10 and 11 were less successful due to experimental problems and will not be emphasized further in the discussion, but the experimental results are included in Appendix B and chapter 10.3, respectively. 5 PV of surfactant solution was injected into SP6 before the co-injection was started to re-saturate the sand pack with surfactant solution. The absolute pressures measured at each location (Inlet, A, B, C and D) stabilized at close to constant values after t=2 PV, and the stable trend continued towards t=40 PV. The fluctuations in pressures may have been caused by foam accumulating ahead of the outlet tubing: foam

accumulating at the outlet creates a barrier that restricts flow and this might suggest the cause for the observed increased pressure. The pressure decreased when foam in contact with the outlet tubing was removed. During the co-injection the production beaker was replaced two times with a new production beaker which could also have caused fluctuations in the absolute pressures. Alternating production of gas and foam was also observed at the production end in this experiment, thus gas-foam slugs may also have influenced the pressures. The absolute pressures in pressure port C (turquoise) and D (blue) have an unexpected behavior until t=18 PV where the absolute pressure measured in pressure port D was higher than the absolute pressure in pressure port C.

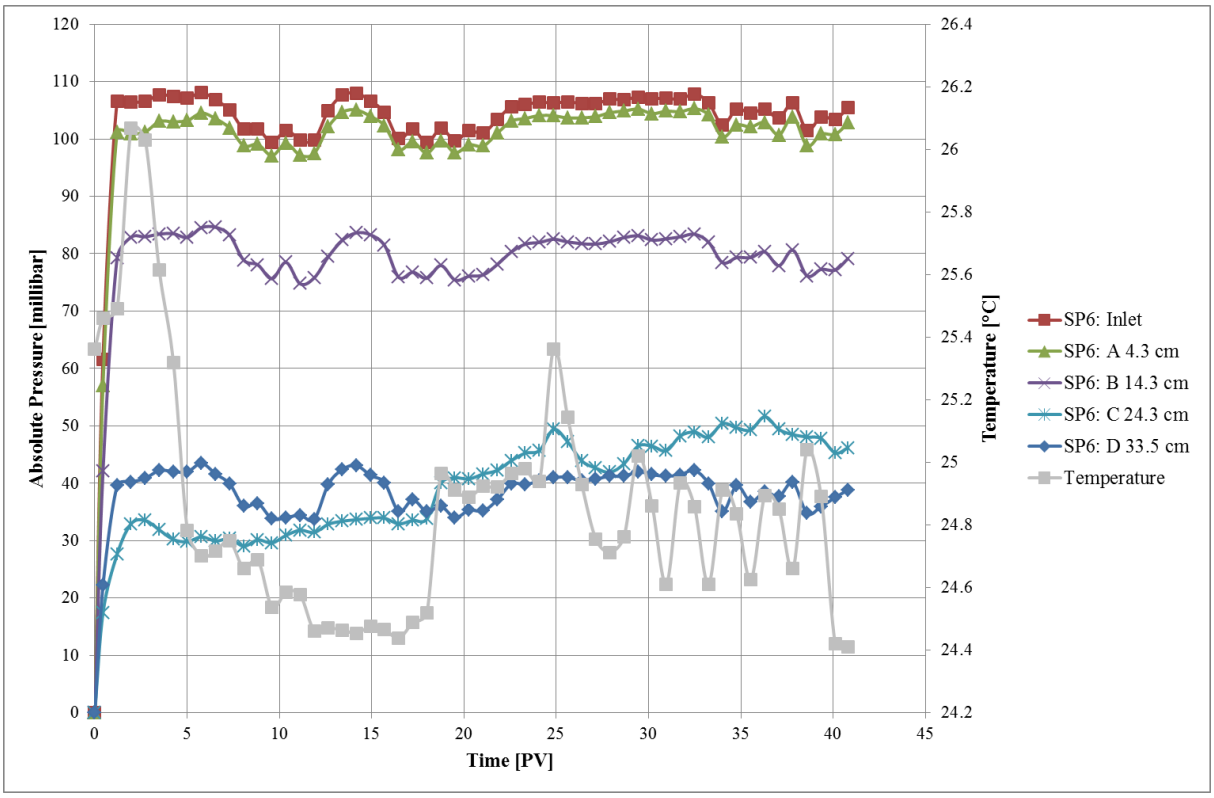

Figure 10.7: Absolute pressures [millibar] as a function of time [PV] measured in five different locations along the sand pack during co-injection into SP6 (experiment 12). The absolute pressures stabilized at close to constant values after t=2 PV, and the stable trend continued towards t=40 PV.

Figure 10.8 shows the calculated pressure gradient across three different sections in sand pack SP6 during co-injection (experiment 12). The general behavior of the pressure gradients across section 1 and 2 were: The pressure gradient increased rapidly before it decreased and became stable. This is typical for surfactant foam. The pressure gradient in section 1 (red) stabilized at 0.7 millibar/cm at t=10 PV. The pressure gradient in section 2 (green) stabilized at 2 millibar/cm at t=5 PV, whereas the pressure gradient in section 3 (purple) decreased from 5-3 millibar/cm over 35 PV injected. The decreasing trend in pressure gradient can indicate unstable foam.

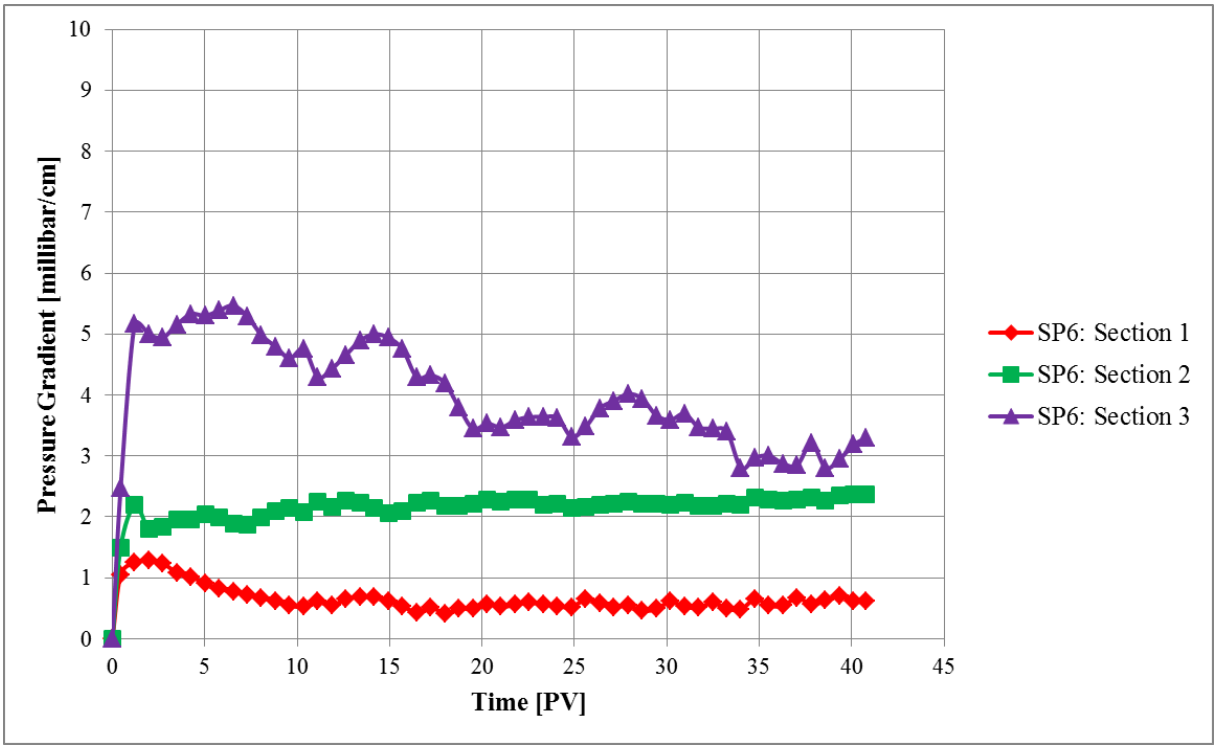

Figure 10.8: The pressure gradient [millibar/cm] across three different locations in sand pack SP6 as a function of time [PV] during co-injection (experiment 12). The pressure gradients across section 1 and 2 reached stable values and the pressure gradient across section 3 decreased.

The apparent viscosity for surfactant foam was calculated by Darcy's law (4.6) for SP6 to compare flow and foam ability in the three sections. The permeability and the apparent foam viscosity in the three sections across SP6 are listed in **Table 10.7**

Table 10.7: The permeability and the apparent foam viscosity in the three sections across sand pack SP6

Section	1	2	3
K [D]	13.4	62.4	26.7
μ_{app} **[cP]**	2.5	44.5	26.5

The viscosity of N_2 gas was 0.017 cP and the apparent foam viscosity in the three sections were higher than gas. This indicates that surfactant foam was generated in all 3 sections across SP6. The apparent foam viscosity in section 2 and 3 were significantly higher than the apparent foam viscosity in section 1. This suggests that stronger foam was generated in section 2 and 3 compared to the generated foam in section 1. In section 1 the pressure gradient stabilized at 0.7 millibar/cm, the permeability was 13.4 D and the apparent viscosity was 2.5 cP. In section 2 the pressure gradient stabilized at 2 millibar/cm, the permeability was 62.4 D and the apparent viscosity was 44.5 cP. In section 3 the pressure gradient did not become stable during the co-injection, the permeability was 26.7 D and the apparent viscosity was 26.5 cP. This indicates that the apparent viscosity varied with the permeability. The apparent foam viscosity increased with higher permeability and consequently strongest foam was generated in section 2 where the permeability was highest.

10. 5 Polymer Enhanced Foam by Co-injection

So far, the development in pressures during co-injections of N_2 gas and surfactant solution has been investigated. Now the focus will shift to what happened when a polymer was added to the surfactant solution. The objective was to investigate the development in absolute pressure in each of the five pressure ports placed along the sand pack and the development in the calculated pressure gradient across the four sections of the sand pack during co-injection. Investigations on whether the absolute pressure in each pressure port along a sand pack becomes stable at plateau values or if it continues to increases during the co-injection of N_2 gas and surfactant+polymer solution will be specially emphasized in this chapter. The observed difference in stabilization is compared with surfactant solution in chapter 10.6. Four polymer enhanced foam experiments are presented and discussed in this chapter. For each co-injection two plots are presented:

- The absolute pressures measured at five specific locations along the sand pack as a function of time.
- The calculated pressure gradients across the four sections in the sand pack as functions of time.

Figure 10.9 shows the development in absolute pressures at five locations during co-injection of N_2 gas and surfactant+polymer solution into sand pack SP4 (experiment 3). The absolute pressures measured at each location (Inlet, A and B) increased fast within t=1 PV. After t=1 PV the general trend was a gradual increase in the absolute pressures. During the co-injection the production beaker was replaced two times with a new production beaker which could have caused fluctuations in absolute pressures. Foam was not observed in the outlet tubing before t=8.5 PV and during the co-injection the N_2 gas front was observed as a segregated front in the sand pack. The front evolved faster in the uppermost part of the sand pack compared to the lowermost part of the sand pack. In addition, light and dark stripes appeared behind the front. Gas represented light areas and dark areas represented surfactant+polymer solution. The delayed N_2 gas front can have been caused by a gas leak in the system. Foam was expected to be observed earlier in the outlet tubing as the volumetric injection rate was 200 ml/h (F_g=0.9) and the pore volume of SP4 was 215.44 ml. This indicates that the f_g was probably lower than expected during the co-injection. During the co-injection it was observed that when the N_2 gas reached the location of pressure port A at t=2 PV the measured absolute pressure increased before the pressure suddenly decreased at t=5 PV and became stable. At t=15 PV the absolute pressure in pressure port A increased again. The absolute pressure monitored in port B increased fast within t=1 PV before it decreased and stabilized. At t= 4 PV the absolute pressure monitored in port B increased which was probably caused by the arrival of N_2 gas front before it decreased and stabilized. At t=10 PV the absolute pressure in pressure port B increased again.

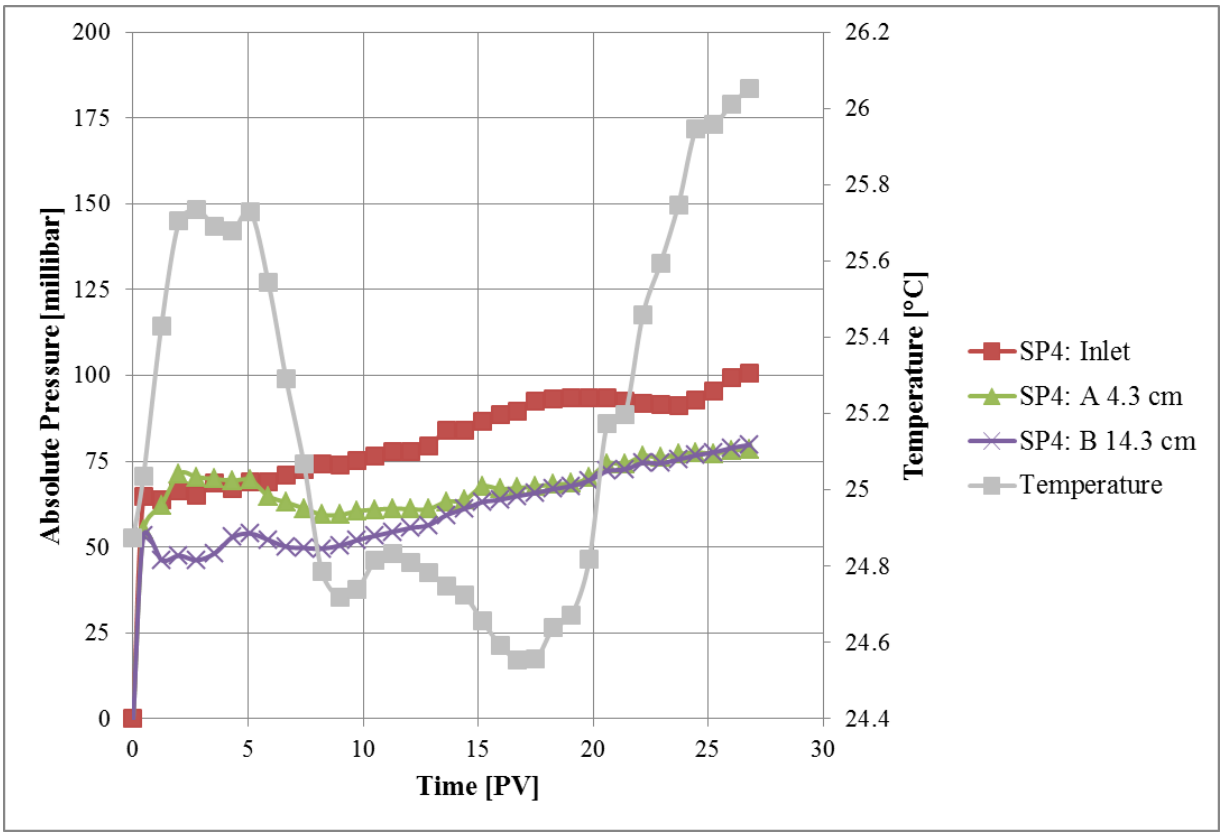

Figure 10.9: Absolute pressures [millibar] as a function of time [PV] measured in three different locations along the sand pack during co-injection into SP4 (experiment 3). The three absolute pressures increased during the co-injection.

Figure 10.10 shows the calculated pressure gradient across two sections in sand pack SP4 during co-injection (experiment 3). The pressure gradient across section 1 (red) increased at the onset of co-injection before it decreased at t=0.5 PV to a negative pressure gradient which can have been caused by the mentioned gas leak. At t=3.5 PV the pressure gradient in section 1 (red) increased from -1.0-6.8 millibar/cm over 14 PV injected, before it decreased and fluctuated towards the end of the co-injection (t=27 PV). The pressure gradient in section 2 (green) increased until t=2.5 PV and decreased from 2.5-0 millibar/cm over 24 PV injected. The fluctuations observed in the pressure gradients across the two sections might suggest foam generation.

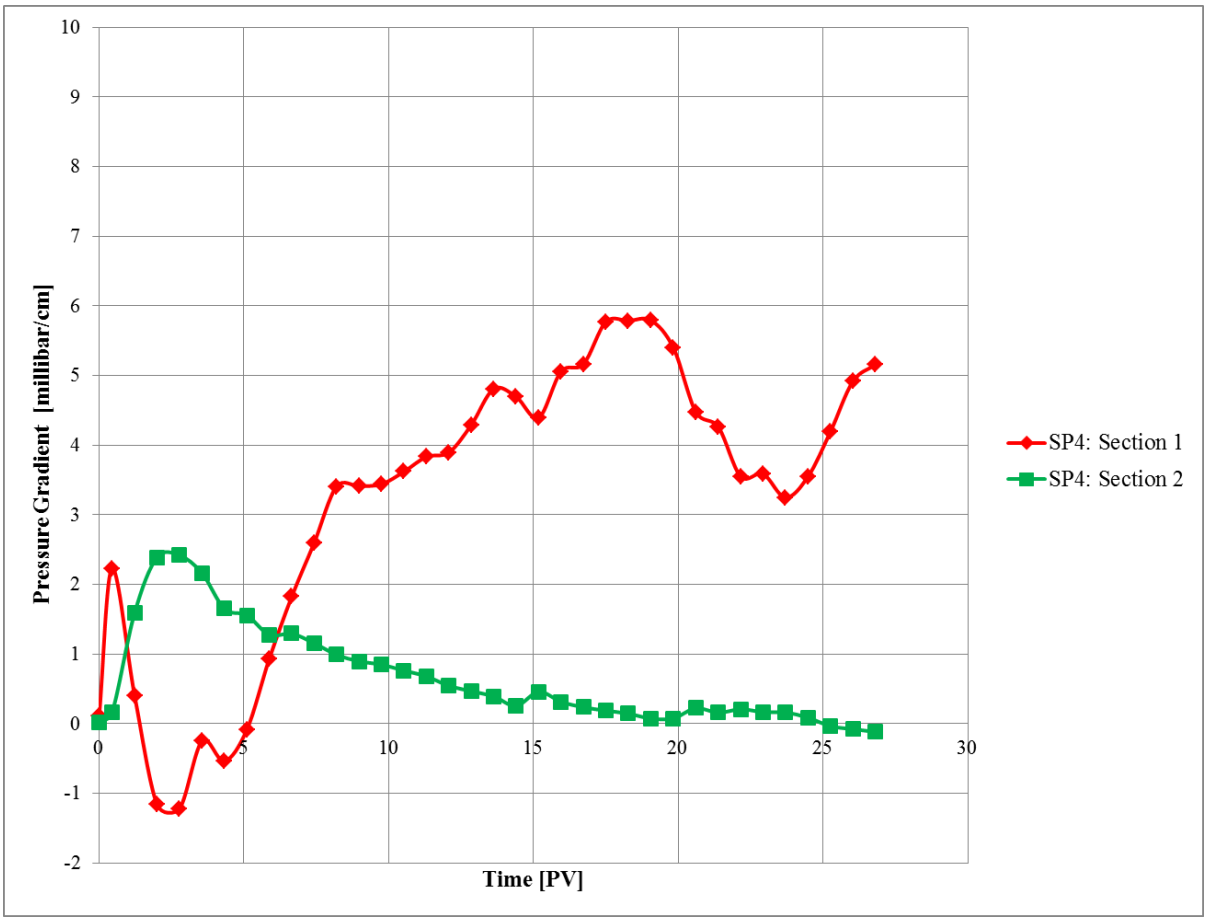

Figure 10.10: The pressure gradient [millibar/cm] across two different locations in sand pack SP4 as a function of time [PV] during co-injection (experiment 3). The pressure gradient across section 1 (red) increased, whereas the pressure gradient across section 2 (green) decreased.

The apparent viscosity for polymer enhanced foam was calculated by Darcy's law (4.6) for SP4 to compare flow and foam ability in the two sections. The permeability and the apparent foam viscosity in the two sections across SP4 are listed in **Table 10.8**.

Table 10.8: The permeability and the apparent foam viscosity in the two sections across sand pack SP4

Section	**1**	**2**
K [D]	3.6	19.4
$\boldsymbol{\mu_{app}}$ **[cP]**	5.6	0.5

The viscosity of N_2 gas was 0.017 cP and the apparent foam viscosity in the two sections were higher than gas indicating that polymer enhanced foam was generated in section 1 and 2 across SP4. The apparent foam viscosity in section 1 was ten times higher than the apparent viscosity in section 2. This indicates that stronger foam was generated in section 1 compared to section 2. In section 1 the pressure gradient did not become stable during the co-injection, but the trend was increasing. The permeability was 3.6 D and the apparent viscosity was 5.6 cP. In section 2 the pressure gradient decreased towards 0 millibar/cm during the co-injection. A decreasing behavior of pressure gradient indicates unstable foam and the apparent foam viscosity was lowest (0.5 cP) in this section despite the highest permeability (19.4 D).

Figure 10.11 shows the development in absolute pressures at five locations during co-injection of N_2 gas and surfactant+polymer solution into sand pack SP4 (experiment 5). SP4 was previously used for two co-injections of N_2 gas and surfactant+polymer solution (experiment 3 and 4). Experiment 4 was less successful due to experimental problems and will not be emphasized further in the discussion, however the experimental results are included in Appendix B. 5 PV of surfactant+polymer solution were injected into SP4 before the co-injection was started to re-saturate the sand pack with surfactant+polymer solution. The absolute pressures measured at each location (Inlet, A, B, C and D) increased until t=18 PV. This increase was much slower than during the co-injections of N_2 gas and surfactant solution in chapter 10.4 where the absolute pressures increased until t=7 PV (experiment 6) and t=2 PV (experiment 12). At t=18 PV a jump in the absolute pressures was observed that probably was caused by an adjustment in the pressure from the N_2 tank. After t=18 PV the recorded absolute pressures developed differently. The absolute pressure measured at Inlet, pressure port C and pressure port D increased slightly with 25 millibar at each location, whereas the absolute pressures at pressure port A and B decreased with 10-25 millibar at each location.

Given the assumption that the saturation of surfactant+polymer solution was constant, then the increase observed in absolute pressure (Inlet, C and D) can indicate a reduction in the relative permeability of gas caused by trapped gas. This indication was based upon that trapped lamellae can block large areas in the porous media initially available for flow, resulting in reduced relative permeability of gas (Radke and Gillis, 1990). Trapping a large portion of the gas is the main mechanism behind the ability foam has to reduce the gas mobility (Hirasaki, 1989). During the co-injection the production beaker was replaced one time with a new production beaker. This could have caused fluctuations in the absolute pressures. Alternating production of gas and foam was also observed at the production end in this experiment, thus gas-foam slugs might also have influenced the pressures.

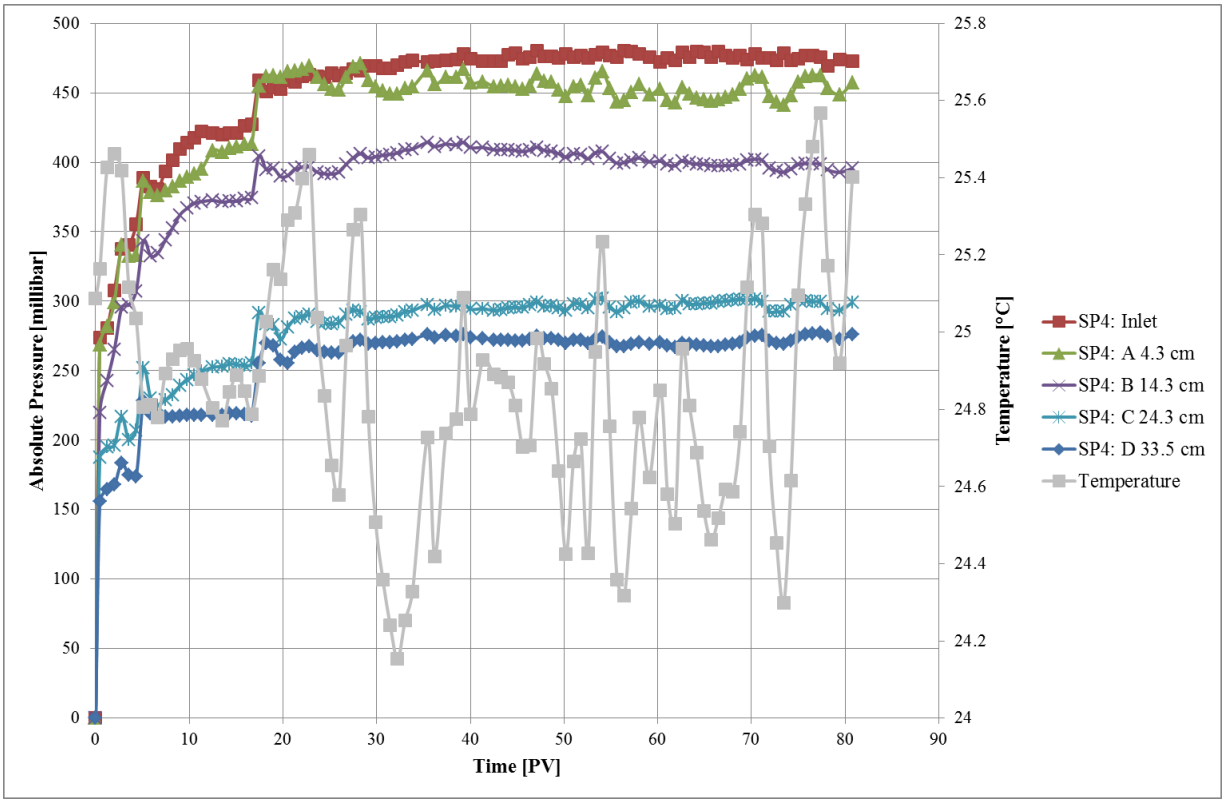

Figure 10.11: Absolute pressures [millibar] as a function of time [PV] measured in five different locations along the sand pack during co-injection into SP4 (experiment 5). The five absolute pressures increased until t=18 PV. After t=18 PV the absolute pressure at Inlet, pressure port C and D increased, whereas the absolute pressures decreased at pressure port A and B.

Figure 10.12 shows the calculated pressure gradient across four different sections in sand pack SP4 during the co-injection (experiment 5). The pressure gradients increased rapidly before they decreased until t=18 PV. The fluctuations between t=18-30 PV can be ignored due to experimental artifact. After t=30 PV the pressure gradients across section 1 (red), 2 (green) and 4 (blue) increased, whereas the pressure gradient across section 3 (purple) decreased. However, the general trend was characterized by fluctuations in the pressure gradients. Fluctuations may be caused by the preceding two co-injections of N_2 gas and surfactant+polymer solution performed in SP4. Even though 5 PV of surfactant+polymer solution was injected into SP4 before the co-injection was started, residual trapped gas can create flow barrier in SP4. The mobilization of trapped gas requires large pressure gradients (Radke and Gillis, 1990) and the addition of a polymer to the surfactant solution can increases the foam stability by reducing the permeability of the lamellae (Bureiko et al., 2014).

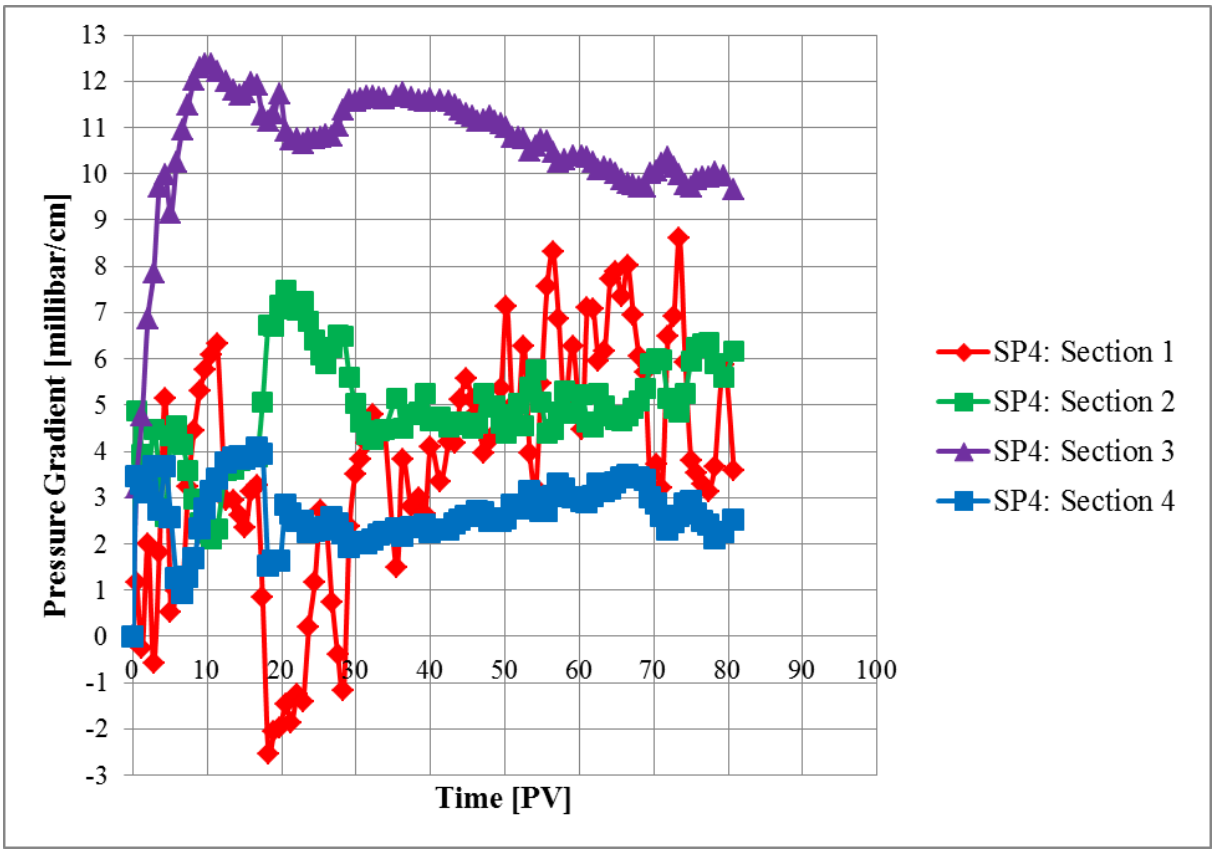

Figure 10.12: The pressure gradient [millibar/cm] across four different locations in sand pack SP4 as a function of time [PV] during co-injection (experiment 5). The four pressure gradients fluctuated during the co-injection.

The apparent viscosity for polymer enhanced foam was calculated by Darcy's law (4.6) for SP4 to compare flow and foam ability in the four sections. The permeability and the apparent foam viscosity in the four sections across SP4 are listed in **Table 10.9**.

Table 10.9: The permeability and the apparent foam viscosity in the four sections across sand pack SP4

Section	**1**	**2**	**3**	**4**
K [D]	3.6	19.4	10	2.98
$\boldsymbol{\mu_{app}}$ **[cP]**	3.9	36.1	29.1	2.3

The viscosity of N_2 gas was 0.017 cP and the apparent foam viscosity in the four sections were higher than gas. This suggests that polymer enhanced foam was generated in all the four sections across SP4. The apparent foam viscosities in section 2 and 3 were significantly higher than the apparent viscosities in section 1 and 4. This indicates that stronger foam was generated in section 2 and 3 compared to section 1 and 4. The highest permeability (19.4 D) and apparent foam viscosity (36.1cP) were observed in section 2, whereas the lowest permeability (2.98 D) and apparent foam viscosity (2.3 cP) were observed in section 4. This indicates as seen previously for the apparent viscosity for surfactant foam (experiment 12) in chapter 10.4 that the apparent foam viscosity increased with higher permeability.

Figure 10.13 shows the development in absolute pressures at four locations during co-injection of N_2 gas and surfactant+polymer solution into sand pack SP5 (experiment 9). During this co-injection the same increasing behavior in absolute pressures were observed as for the previously presented co-injections (experiment 3 and 5) in this chapter. SP5 was previously used for three co-injections: N_2 gas and surfactant solution (experiment 6), N_2 gas and surfactant+polymer solution (experiment 7) and N_2 gas and surfactant solution (experiment 8). The experimental results from experiment 6 was presented and discussed in chapter 10.4. The experimental results from experiment 7 and 8 will be presented and discussed in chapter 10.6. The absolute pressures measured at the four locations (A,B,C and D) during the co-injection into SP5 increased until t=10 PV and afterwards the absolute pressures continued to increase uniformly probably due to gas trapping, like in **Figure 10.11**.The total increase in absolute pressure was 15-30 millibar at each location in SP5.

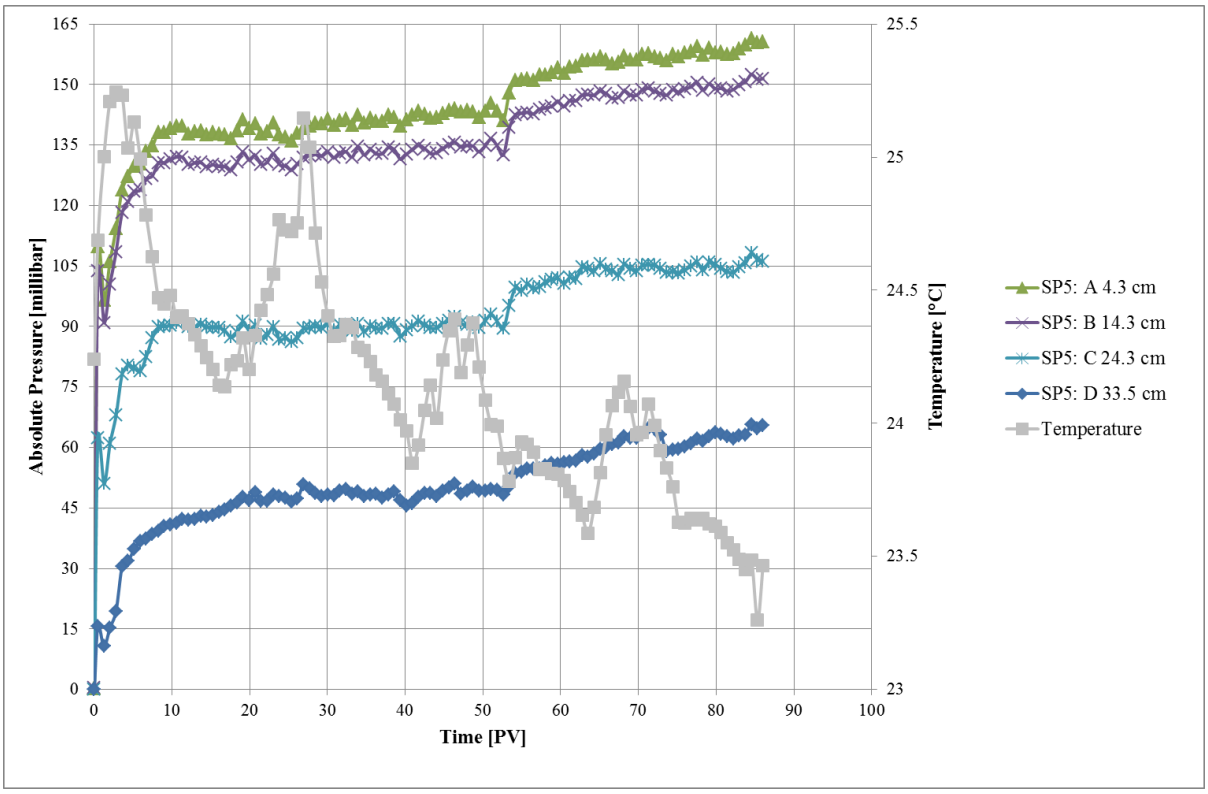

Figure 10.13: Absolute pressures [millibar] as a function of time [PV] measured in four different locations along the sand pack during co-injection into SP5 (experiment 9). The absolute pressures increased at each location in SP5 during the co-injection.

Figure 10.14 shows the calculated pressure gradient across three sections in sand pack SP5 during co-injection (experiment 9). All the pressure gradients increased fast (within t=1 PV) before they gradually stabilized. The stabilized pressure gradient across section 2 (green) was 1 millibar/cm at t=30 PV. The stabilized pressure gradient across section 3 (purple) was 4.2 millibar/cm at t=20 PV. The stabilized pressure gradient across section 4 (blue) was 4.5 millibar/cm at t=30 PV. However, the pressure gradient across section 4 (blue) fluctuated more than the pressure gradients across section 2 (green) and 3 (purple).

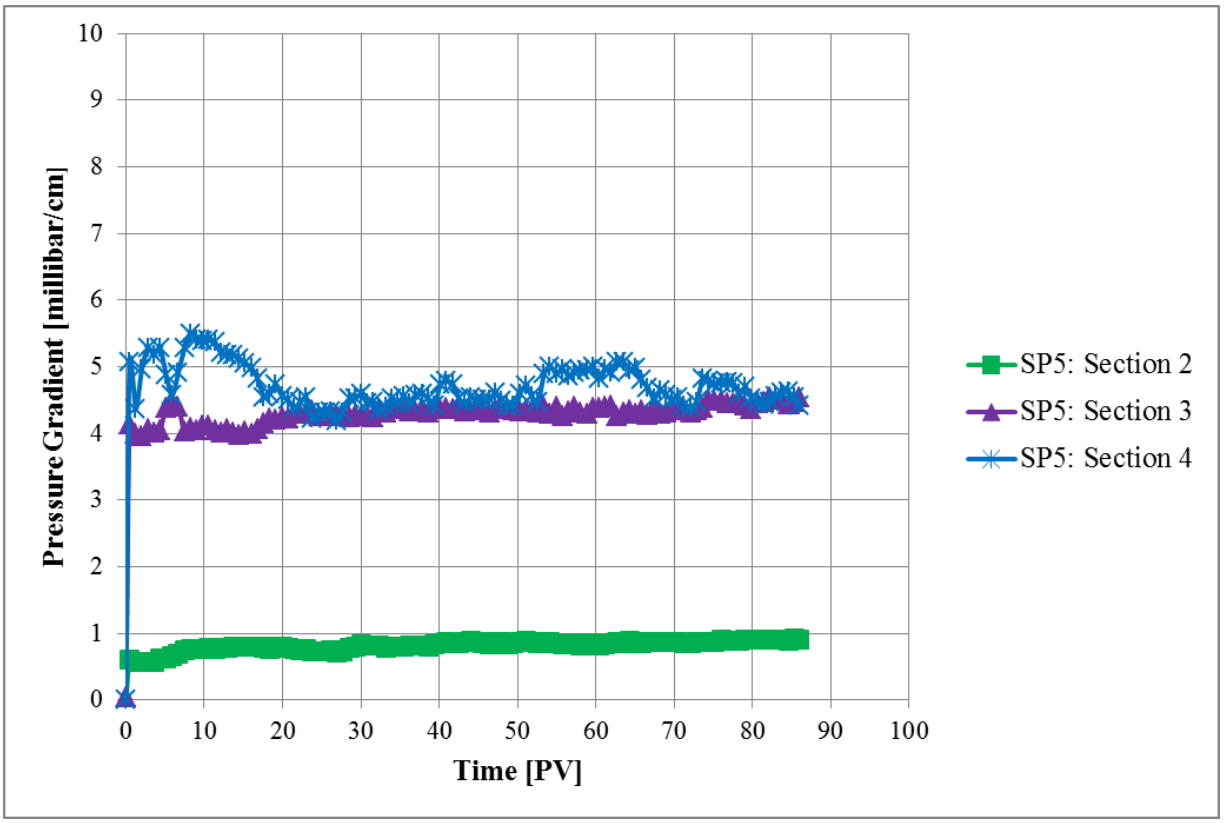

Figure 10.14: The pressure gradient [millibar/cm] across three different locations in sand pack SP5 as a function of time [PV] during co-injection (experiment 9). The three pressure gradients across SP5 became stable during the co-injection.

The apparent viscosity for polymer enhanced foam was calculated by Darcy's law (4.6) for SP5 to compare flow and foam ability in the three sections. The permeability and the apparent foam viscosity in the three sections across SP5 are listed in **Table 10.10**.

Table 10.10: The permeability and the apparent foam viscosity in the three sections across sand pack SP5

Section	2	3	4
K [D]	29.1	17.1	37.5
μ_{app} [cP]	8.0	23.4	49.9

The viscosity of N_2 gas was 0.017 cP and the apparent foam viscosity in the three sections were higher than gas indicating that polymer enhanced foam was generated in all three sections across SP5. The apparent viscosity in section 3 and 4 were higher than the apparent foam viscosity in section 2. This indicates that stronger foam was generated in section 3 and 4 compared to the generated foam in section 2. In section 2 the pressure gradient stabilized at 1 millibar/cm, the permeability was 29.1 D and the apparent foam viscosity was 8.0 cP. In section 4 the stabilized pressure gradient was 4.5 millibar, the permeability was 37.5 D and the apparent foam viscosity was 49.9 D. This indicate as previously observed both for surfactant foam (experiment 12) in chapter 10.4 and polymer enhanced foam (experiment 5) that the apparent foam viscosity increased with higher permeability. However, as observed during co-injection of N_2 gas and surfactant solution (experiment 6) in chapter 10.4 stronger foam was generated in section 3 compared to section 2 even though the permeability was higher in section 2 compared to section 3. This is caused by the lower stabilized pressure gradient (1 millibar/cm) in section 2 compared to the higher stabilized pressure gradient (4.2 millibar) in section 3.

The co-injection into SP8MAF (experiment 14) presented in **Figure 10.15** and **10.16** was conducted by Associated Professor Martin Fernø. **Figure 10.15** shows the development in absolute pressures at four locations (Inlet, B, C and D) during co-injection of N_2 gas and surfactant+polymer solution. The general trend for the absolute pressures was a uniform increase that was similar to the observed trend in **Figure 10.13**. However, the absolute pressure in each location in **Figure 10.15** reached significantly higher pressures during a shorter amount of time compared to the absolute pressures in each location in **Figure 10.13.** For example, the absolute pressure in pressure port B increased towards 1800 millibar during 30 PV injected in **Figure 10.15**, whereas the absolute pressure in pressure port B increased towards 150 millibar during over 80 PV injected in **Figure 10.13**. This could be caused by the lower permeability (4.81 D) and porosity (31%) across SP8MAF compared to SP5 (K=71.71 D and Ø=33 %), see **Table 10.1** and **10.3**. In addition, the permeability across the section 1* and section 3 were relatively similar compared to the large variations in permeability across the four sections in SP5. This indicate that SP8MAF was more homogenous compared to SP5, see **Table 10.3**. The fluctuation in the absolute pressures observed between t=22-28 PV can have been caused by foam accumulating ahead of the outlet tubing: foam accumulating at the outlet creates a barrier to flow and may therefore have caused increasing pressures. The pressure decreased when foam that was in contact with the outlet tubing was removed

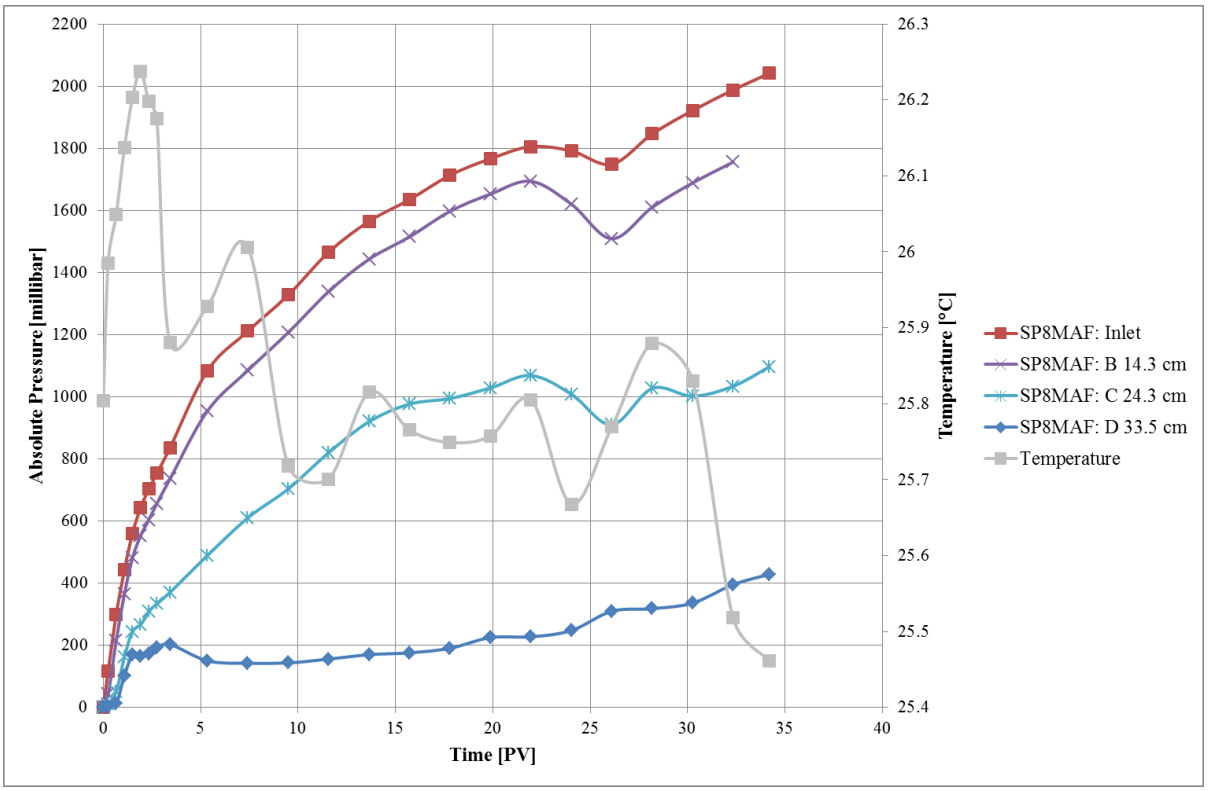

Figure 10.15: Absolute pressures [millibar] as a function of time [PV] measured in four different locations along the sand pack during co-injection into SP8MAF (experiment 14). All the absolute pressures increased during the co-injection.

Figure 10.16 shows the calculated pressure gradient across three sections in sand pack SP8MAF during co-injection (experiment 14). The three pressure gradients were calculated from the absolute pressure measurements and are represented in the following sections: Section 1* (yellow), Section 3 (purple) and Section 4 (blue). Section 1* (yellow) represents the calculated pressure gradient between pressure port Inlet and B. The pressure gradient across section 1* (yellow) increased until t=5 PV before it stabilized at 9 millibar/cm at t=5 PV. The pressure gradients across section 3 (purple) and 4 (blue) increased until t= 15 PV before they stabilized at 60 millbar/cm and 88 millibar/cm, respectively. The fluctuations observed between t=22-28 PV was caused by foam accumulating ahead of the outlet tubing as explained above. The gradual increasing trend observed in experiment 14 was also observed during the first 15 PV injected in **Figure 10.12** (experiment 5), whereas in **Figure 10.14** (experiment 9) the pressure gradients increased fast (within t=1 PV) before they gradually became stable. Repeat injections during several experiments were previously performed on both SP4 (experiment 5) and SP5 (experiment 9). However, the observed difference in the development in pressure gradients in **Figure 10.12** and **10.14** can might have been caused by that SP4 in experiment 5 were re-saturated with surfactant+polymer solution prior to the co-injection, whereas SP5 in experiment 9 was.

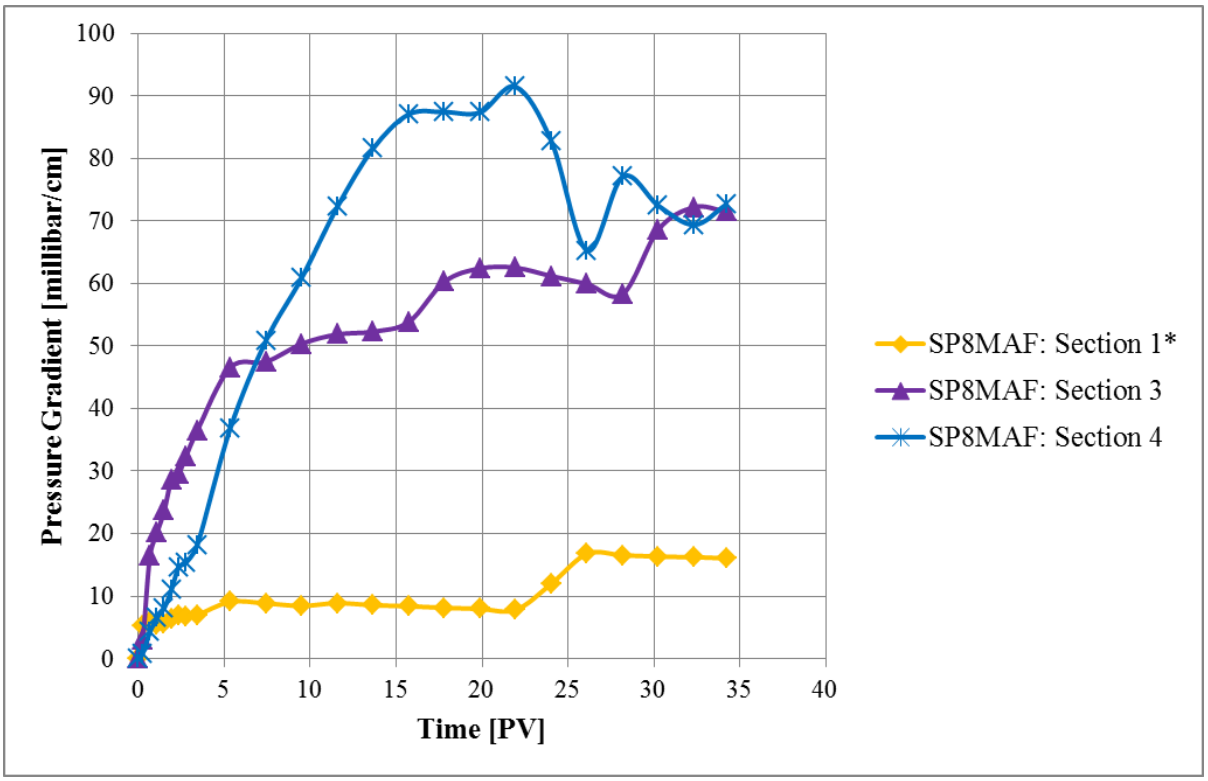

Figure 10.16: The pressure gradient [millibar/cm] across three different locations in sand pack SP8MAF as a function of time [PV] during co-injection (experiment 14). The pressure gradient across section 1* stabilized, whereas the pressure gradients across section 3 and 4 increased during the co-injection.

The apparent viscosity for polymer enhanced foam was calculated by Darcy's law (4.6) for SP8MAF to compare flow and foam ability in section 1* and 3. Section 4 was not included as no pressure transducer was connected to pressure port D during the permeability measurements. The permeability and the apparent foam viscosity in the three sections across SP5 are listed in **Table 10.11**.

Table 10.11: The permeability and the apparent foam viscosity in the three sections across sand pack SP8MAF

Section	**1***	**3**
K [D]	8.6	6
$\boldsymbol{\mu_{app}}$ **[cP]**	41.634	129.402

The viscosity of N_2 gas was 0.017 cP and the apparent foam viscosity in section 1* and 3 were higher than gas. This indicates that polymer enhanced foam was generated in both sections across SP8MAF. The apparent viscosity in section 3 was higher than the apparent foam viscosity in section 1*. This indicates that stronger foam was generated in section 3 compared to the generated foam in section 1*.

10.6 Surfactant Foam versus Polymer Enhanced Foam

The effect of surfactant foam by co-injection and polymer enhanced foam by co-injection on the development in absolute pressure in each of the five pressure ports placed along a sand pack and the development in the pressure gradient across the four different sections of the sand pack are compared in this chapter.

Figure 10.17 shows the development in absolute pressures at five locations during co-injection. The co-injection was performed continuously into sand pack SP5 and was divided into three injections:

- Injection 1: Co-injection of N_2 and surfactant solution (experiment 6)
- Injection 2: Co-injection of N_2 gas and surfactant+polymer (experiment 7)
- Injection 3: Co-injection of N_2 and surfactant solution (experiment 8)

The change of injected foaming agent is indicated with vertical dashed lines.

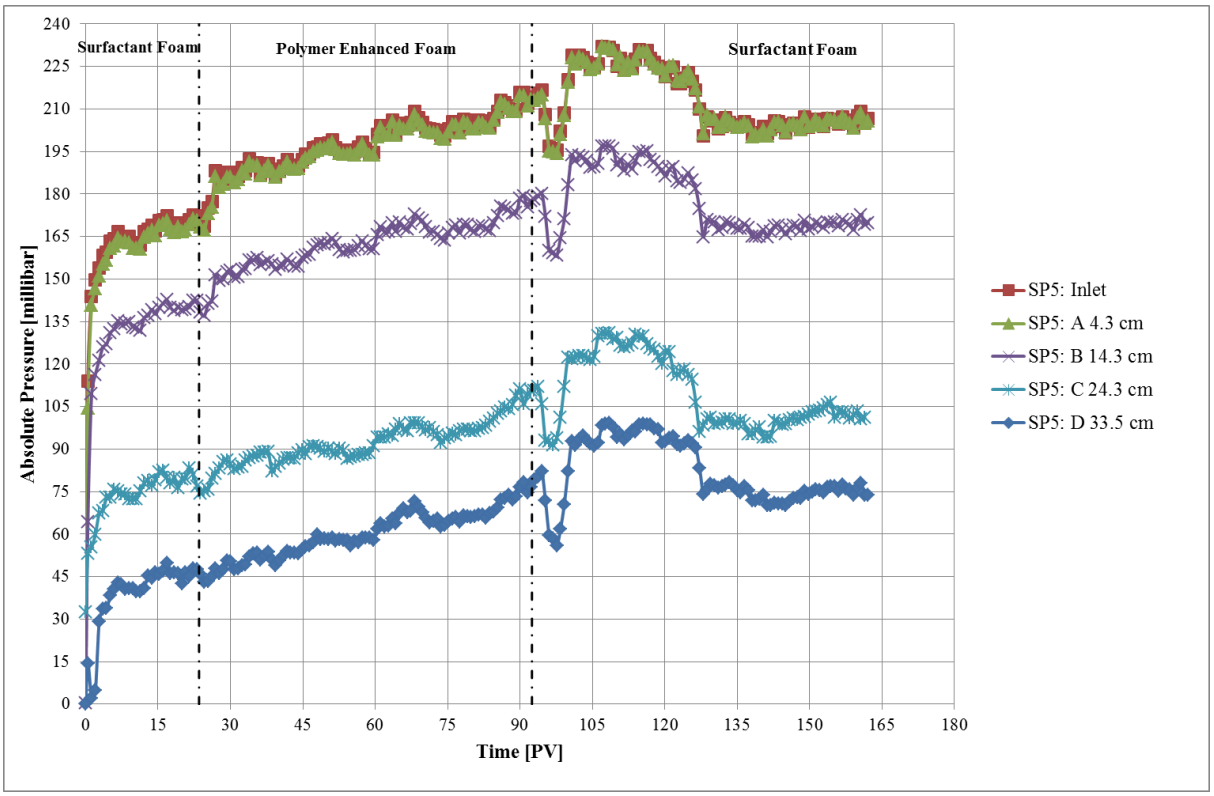

Figure 10.17: Absolute pressures [millibar] as a function of time [PV] measured in five different locations along the sand pack during co-injection into SP5 (experiment 6, 7 and 8). The change of injected foaming agent is indicated with vertical dashed lines.

The general trend observed in the absolute pressures during the 3 co-injections was:

- Injection 1- surfactant foam: Absolute pressures increased and stabilized.
- Injection 2 - polymer enhanced foam: Absolute pressure increased uniformly.
- Injection 3 - surfactant foam: Absolute pressure increased and stabilized.

A detailed presentation of the result and discussion of the absolute pressures measured at five locations (Inlet, A, B, C and D) during injection 1-surfactant foam (experiment 6) was presented in chapter 10.4. A detailed presentation of the result and discussion of the absolute pressures measured at five locations (Inlet, A, B, C and D) during injection 2- polymer enhanced foam (experiment 7) and during injection 3-surfactant foam (experiment 8) are presented in this chapter.

Injection 2 - polymer enhanced foam by co-injection was started at t=23.5 PV and was ended at t=92.5 PV. During the co-injection of N_2 gas and surfactant+polymer solution a uniform increasing trend in the absolute pressures were observed and the total increase in absolute pressures was 30-50 millibar at each location in SP5. The uniform increasing trend in the absolute pressures was probably caused by gas trapping. Fluid samples were taken during the co-injection and can have caused the fluctuations in the absolute pressure. Alternating production of gas and foam was observed at the production end in this experiment, thus gas-foam slugs may have influenced the absolute pressures.

Injection 3- surfactant foam by co-injection was started at t=92.5 PV and was ended at t=162 PV. During the co-injection of N_2 gas and surfactant solution the absolute pressures became stable at t=100 PV. The stable trend continued towards t=122 PV before a sudden drop in absolute pressures was observed. At t=127 PV the absolute pressures reached a stable trend again. Alternating production of gas and foam was also observed at the production end in this experiment, thus gas-foam slugs may have influenced the absolute pressures.

Figure 10.18 shows the calculated pressure gradient across four different sections in sand pack SP5 during co-injection (experiment 6, 7 and 8). The change of injected foaming agent is indicated with vertical dashed lines.

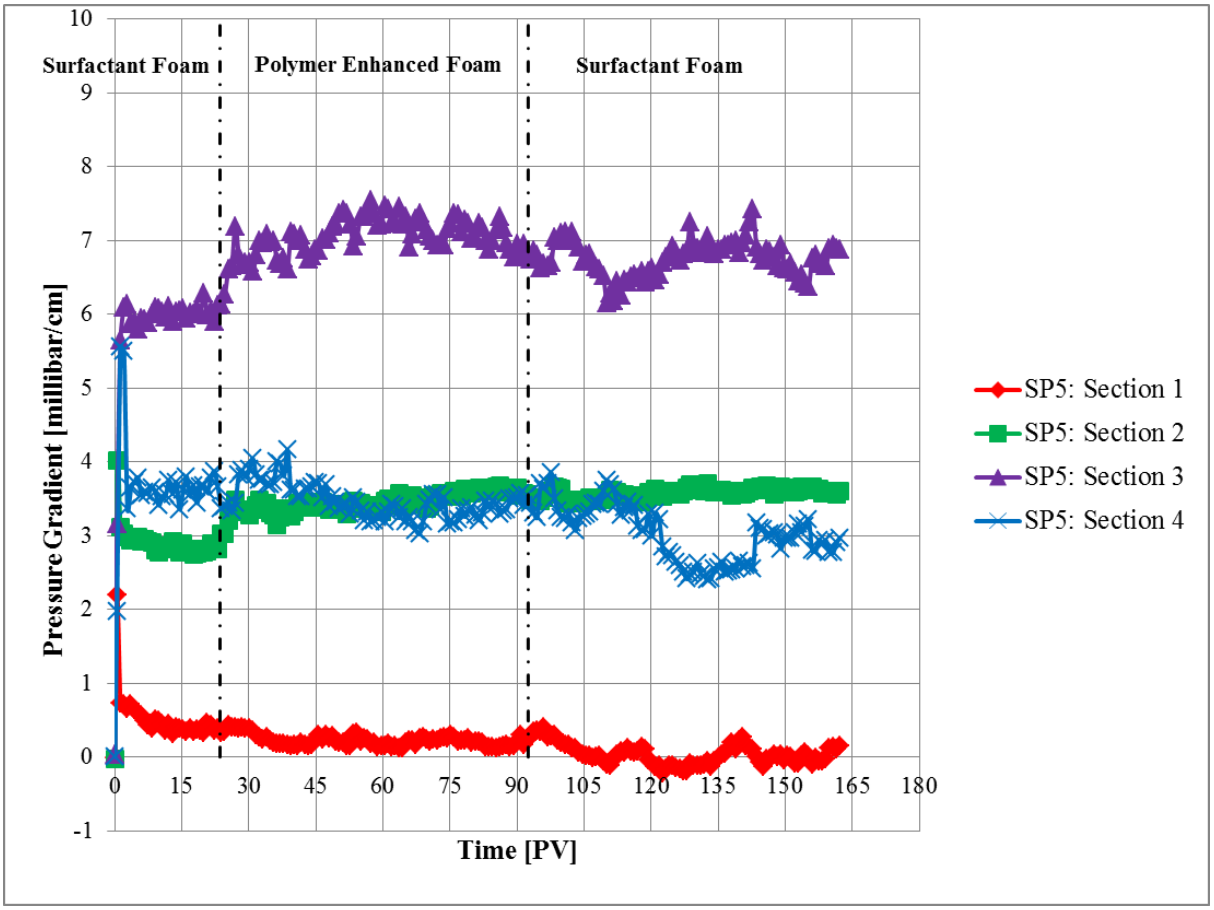

Figure 10.18: The pressure gradient [millibar/cm] across four different locations in sand pack SP5 as a function of time [PV] during co-injection (experiment 6, 7 and 8). The change of injected foaming agent is indicated with vertical dashed lines.

The general behavior of the pressure gradient across the four sections in SP5 during the co-injections was:

- Injection 1 - surfactant foam: Pressure gradient increased before it decreased and became stable.
- Injection 2 - polymer enhanced foam: Pressure gradient increased before it became stable.
- Injection 3 - surfactant foam: Pressure gradient increased before it decreased and became stable.

However, all the pressure gradients were fluctuating with varying degree after stabilization during the 3 different injections. The pressure gradients across section 1 (red), 3 (purple) and

4 (blue) were more stable during injection 1 compared to injection 2 and 3. The pressure gradient across section 2 (green) was very stable throughout the entire co-injection compared to the pressure gradients across section 1 (red), 3 (purple) and 4 (blue).

The apparent foam viscosities were calculated by Darcy's law (4.6) for the three co-injections to compare flow and foam ability in the four sections. The permeability and the apparent foam viscosity in the four sections across SP5 during the three co-injections are listed in **Table 10.12**.

Table 10.12: The permeability and the apparent foam viscosity in the four sections across sand pack SP5 during injection 1, 2 and 3.

Section	**1**	**2**	**3**	**4**
K [D]	2.05	29.1	17.1	37.5
Injection 1: μ_{app} [cP]	0.2	24.7	31.6	41.3
Injection 2: μ_{app} [cP]	0.2	31.3	35.3	40.6
Injection 3: μ_{app} [cP]	0.1	31.6	35.5	33.5

The viscosity of N_2 gas was 0.017 cP and the apparent foam viscosity across the four sections during all the three co-injections were higher than gas. This indicates that surfactant foam was generated during injection 1 as discussed in chapter 10.4, and that polymer enhanced foam and surfactant foam were generated during injection 2 and 3, respectively. The apparent foam viscosity in section 2, 3 and 4 were significantly higher than the apparent foam viscosity in section 1 during the three injections. This indicates that stronger foam was generated in section 2, 3 and 4 compared to the generated foam in section 1. The apparent foam viscosity increased in section 2 and 3 during injection 2 compared to injection 1. However, in section 4 the apparent foam viscosity decreased during injection 2 compared to injection 1. The apparent foam viscosity in section 1 remained at 0.2 cP during injection 2. This indicates that polymer enhanced foam were stronger than surfactant foam in section 2 and 3, but not in section 1 (same strength) and 4 (less strong). The apparent foam viscosity in section 2 and 3 during injection 3 were similar to the apparent foam viscosity during injection 2, whereas the apparent foam viscosity decreased in section 1 and 4 during injection 3 compared to injection 2. This indicates that surfactant foam was weaker in section 1 and 4 compared to the polymer enhanced foam during injection 2, but not in section 2 and 3 (same strength). In addition, as previously observed for surfactant foam (experiment 12) and polymer enhanced foam (experiment 5) the apparent foam viscosity increased with higher permeability. This was

observed for section 1 and 4 during the three co-injections. However, stronger foam was generated in section 3 compared to section 2 even though the permeability was higher in section 2 compared to section 3. This was also observed during the polymer enhanced foam by co-injection into SP5 that was discussed in chapter 10.5.

10.7 Polymer Enhanced Foam Visualized in PET-CT

One co-injection of N_2 gas and surfactant+polymer solution was conducted at Haukeland University Hospital using sand pack SP7 (experiment 13). The experiment involved labeling the surfactant+polymer solution with the nuclear tracer ^{18}FDG. The fundamentals about PET-CT scanner are briefly discussed in chapter 6. The objective was to investigate the saturation development of the surfactant+polymer solution labeled with ^{18}FDG during co-injection and correlate it with pressure data. A CT scan was performed on the saturated SP7 before the co-injection and PET recording were started. PET data alone cannot identify the shape and density of SP7. By combining CT scan and PET images with equal resolution a 3D visualization of the injected surfactant+polymer solution can be created. The half-life of ^{18}FDG is 110 min. During the PET recording the detected radiation decreases due the disintegration of ^{18}FDG. The PET scanner takes this into account by calculating the same delivered signal despite the reduction in radiation from ^{18}FDG. The PET scanner was set to measure signals for 8 hours to obtain satisfying signals. 16.6 cm of SP7 was recorded by the PET scanner and the recorded interval was divided into 83 slices. The total length of SP7 was 38.3 cm and the location for PET recording was set to start at 12.5 cm and ended at 29.1 cm. This interval includes pressure port B and C, located 14.3 cm and 24.3 cm into SP7. This area of SP7 is referred to as section 3 (see **Table 10.5** for details) and is of particular interest because based on the previous polymer enhanced foam by co-injections foam generation occurred in this section. In this chapter the monitored pressure during the co-injection will be presented first, followed by 1 D saturation profiles and the final presentation will be both the 2D and 3D visualizations of saturation development.

Figure 10.19 shows the development in absolute pressures at five locations during co-injection of N_2 gas and labeled surfactant+polymer solution into sand pack SP7 (experiment 13). The absolute pressures increased fast (reached maximum at t=2 PV) before they decreased and stabilized. From t=9 PV a uniform increasing trend in the absolute pressures were observed at locations Inlet, A, C and D, whereas the pressure in location B remained stable. The same increasing behavior has also been observed for absolute pressures in the previously discussed co-injections of N_2 gas and surfactant + polymer (**Figure 10.9**, **10.11**, **10.13**, **10.15** and **10.17**) in chapter 10.4 and 10.5.

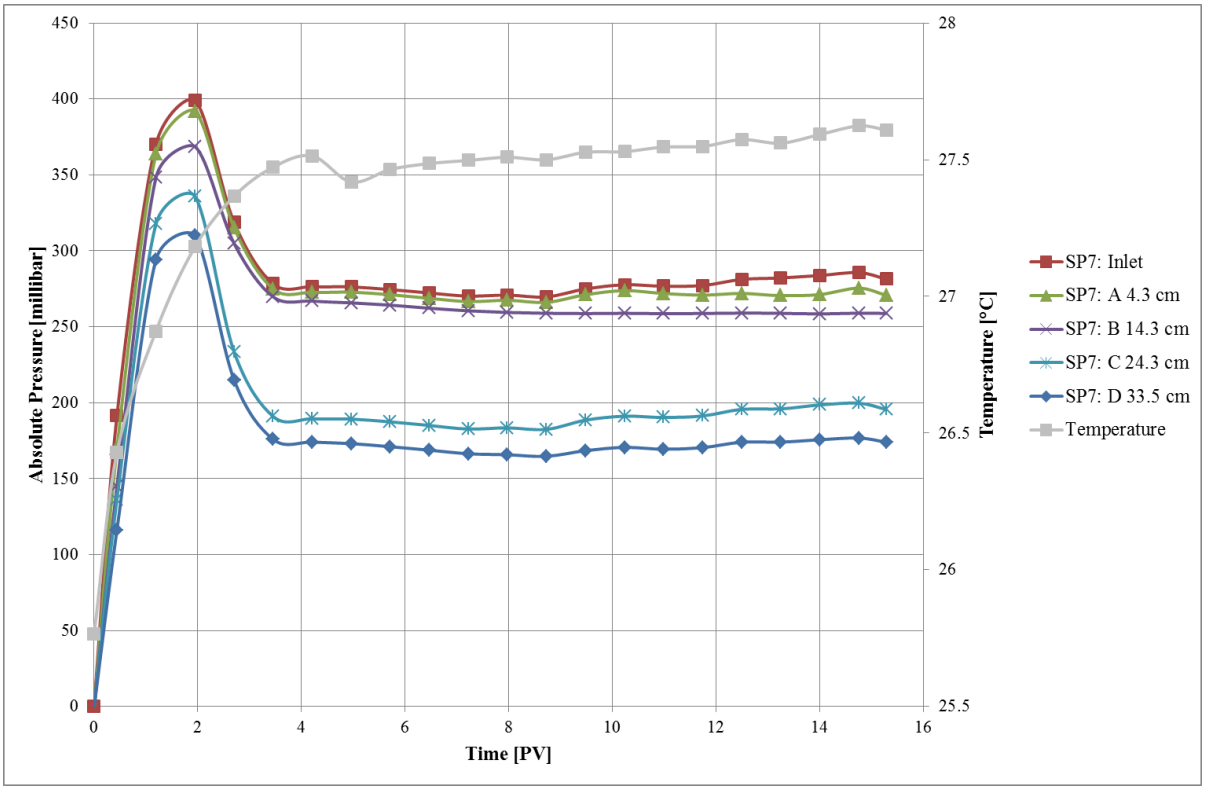

Figure 10.19: Absolute pressures [millibar] as a function of time [PV] measured in five different locations along the sand pack during co-injection into SP7 (experiment 13). The absolute pressures increased before they decreased and stabilized. From t=9 PV the absolute pressure in Inlet, A, C and D increased, whereas the absolute pressure in B remained stable.

Figure 10.20 shows the calculated pressure gradient across four different sections in sand pack SP7 during co-injection (experiment 13). The pressure gradients across section 1 (red), 2 (green) and 4 (blue) behaved relatively similar. The pressure gradients increased fast (reached maximum within t=2 PV) before they decreased and fluctuated over 15 PV injected. The pressure gradient across section 3 (purple) increased and reached maximum at t=3.5 PV before it decreased from 8-6 millibar/cm over 15 PV injected.

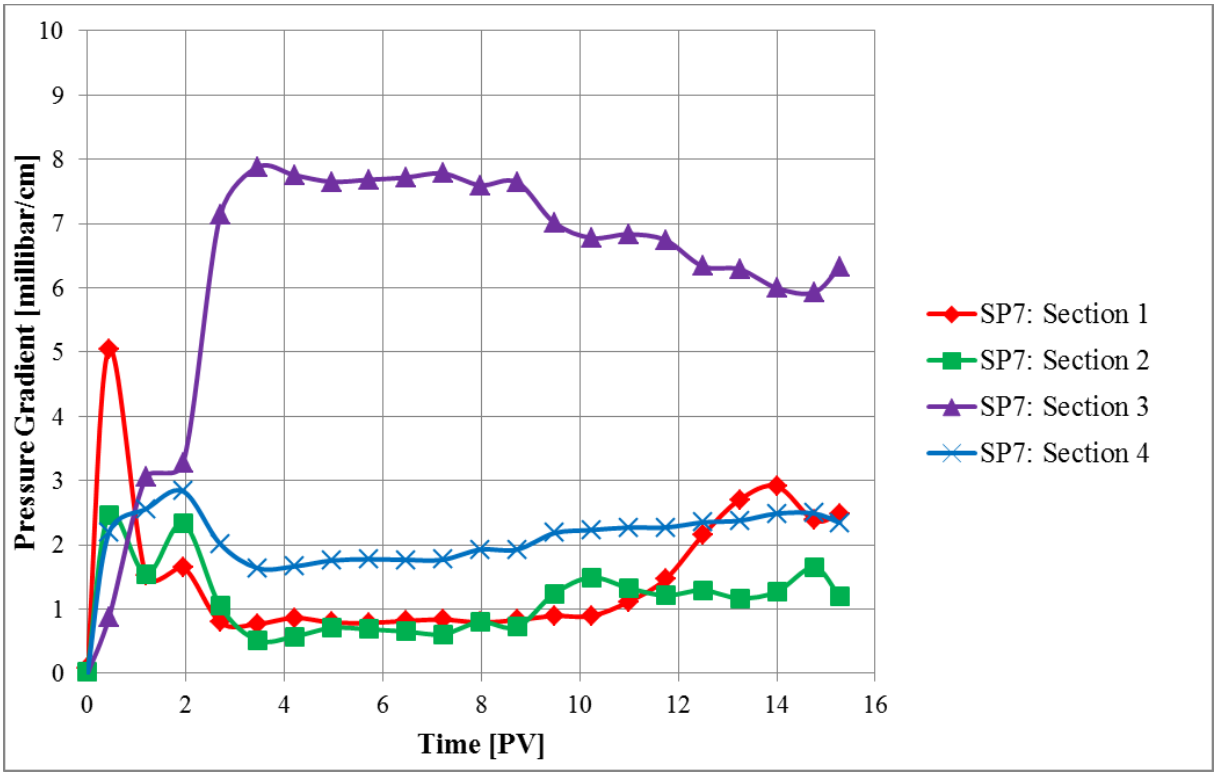

Figure 10.20: The pressure gradient [millibar/cm] across four different locations in sand pack SP7 as a function of time [PV] during co-injection (experiment 13). The four pressure gradients did not become stable during the co-injection.

The apparent viscosity for polymer enhanced foam was calculated by Darcy's law (4.6) for SP7 to compare flow and foam ability in the four sections. The permeability and the apparent foam viscosity in the four sections across SP7 are listed in **Table 10.13**.

Table 10.13: The permeability and the apparent foam viscosity in the four sections across sand pack SP7

Section	1	2	3	4
K [D]	9.4	25.3	18.2	19.9
μ_{app} [cP]	7.0	9.1	34.7	14.1

The viscosity of N_2 gas was 0.017 cP and the apparent foam viscosity in the four sections were higher than gas indicating that polymer enhanced foam was generated in all the sections across SP7. The apparent foam viscosity was higher in section 3 and 4 compared to the apparent viscosity in section 1 and 2. This indicates that stronger foam was generated from the middle towards the outlet, whereas weaker foam was generated closer to the inlet. In section 1 the permeability was 9.4 D and the apparent foam viscosity was 7 cP. In section 2 the permeability was 25.3 D and the apparent foam viscosity was 9.1 cP. In section 3 the permeability was 18.2 D and the apparent foam viscosity was 34.7 cP. In section 4 the permeability was 19.9 D and the apparent foam viscosity was 14.1 cP. This indicates that apparent foam viscosity did not vary with the permeability. However, based on previously observations in chapter 10.5 the apparent foam viscosity increased with higher permeability, see **Table 10.9**. The difference in the obtained result in **Table 10.13** and **10.9** could have been caused by the difference in PV injected. In **Figure 10.12** 80 PV was injected during the co-injection, whereas in **Figure 10.20** only 15 PV was injected.

Figure 10.21 shows the 1D saturation profiles of surfactant+polymer solution during co-injection at 16 time steps. The detected counts are plotted as function of length of the scanned interval of SP7. The PET scan was started at 12.5 cm into SP7. Each scan slice was 0.2 cm thick and the first count was recorded at 12.7 cm into SP7. The detected counts from the PET signal during co-injection are proportional to the labeled saturation of the surfactant+polymer solution. The development of the surfactant+polymer solution was non-uniform. The saturation gradually increased from 1.5 PVinjected (PV_{inj}). At 1.5, 2.0, 2.4, 2.9 and 3.3 PV_{inj} the saturation was highest at the start of the scanned interval in SP7 before it gradually decreased and increased again. At 3.8 PV_{inj} the trend was changed. At 3.8, 4.2, 4.7, 5.1, 5.6, 6.0, 6.5 and 6.9 PV_{inj} the saturation was high at the start before it gradually decreased and increased again. The saturation reached a higher saturation at the end of the scanned length compared to the saturation at the beginning of the scanned length. This suggests that possible porosity variations within the scanned interval of SP7 might have caused the non-uniform saturation development. The relatively low saturation between 17.5 cm and 23.5 cm in SP7 can indicate that a portion of the pore space was occupied with trapped gas or had a lower porosity compared to the remaining interval of the scanned SP7.

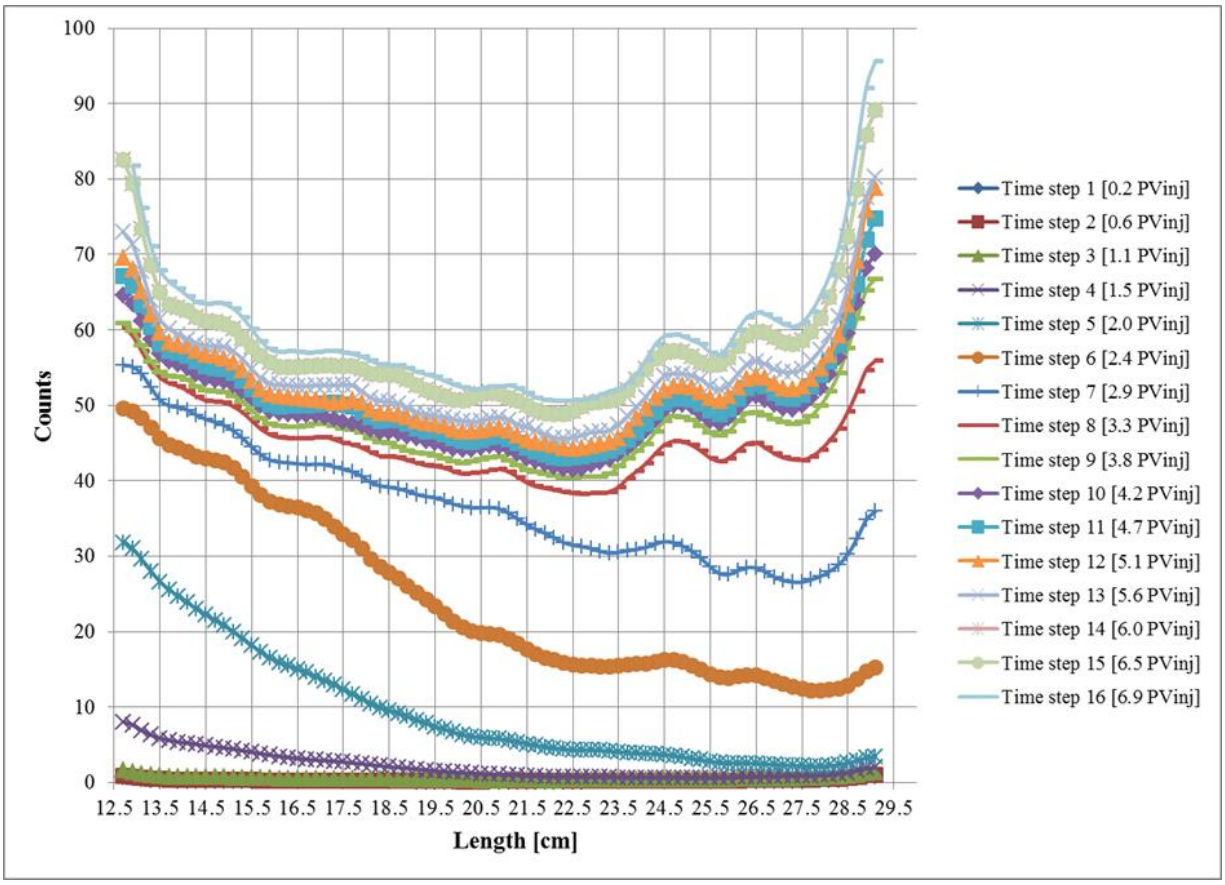

Figure 10.21: 1D saturation profiles of surfactant+polymer solution during co-injection into SP7 (experiment 13) at 16 time steps. The detected counts are plotted as function of length of the scanned interval of SP7. The detected counts during the co-injection reflect the saturation of the surfactant+polymer solution.

Figure 10.22 shows the calculated pressure gradient across section 3 (purple) and average counts per 1D saturation profile (orange) as a function of time. Section 3 represents the calculated pressure gradient between pressure ports B and C during the co-injection. The detected counts from the PET signal during the co-injection are proportional to the saturation of the labeled surfactant+polymer solution. Between t=1-2 PV was the pressure gradient stable, whereas the saturation of the labeled surfactant+polymer solution increased. The pressure gradient and the saturation of the labeled surfactant+polymer solution increased relatively fast between t=2-3 PV. This can indicate that the critical saturation for foam generation was between t=2-3 PV. At t=3.5 PV the pressure gradient reach maximum, while the average labeled surfactant+polymer solution continued to increase until t=7 PV. However, the local 1D saturation profile at time step 9 (t=3.8 PV) of the labeled surfactant+polymer solution (t=3.8 PV) was maximum at pressure port B (14.3 cm) in **Figure 10.21,** when solely considering the interval between pressure port B and C (14.3 – 24.3 cm). Prior to the co-injection adsorption was satisfied, and consequently a non-labeled surfactant+polymer

solution was present in SP7 that will affect the dynamic in the pressure development during the co-injection.

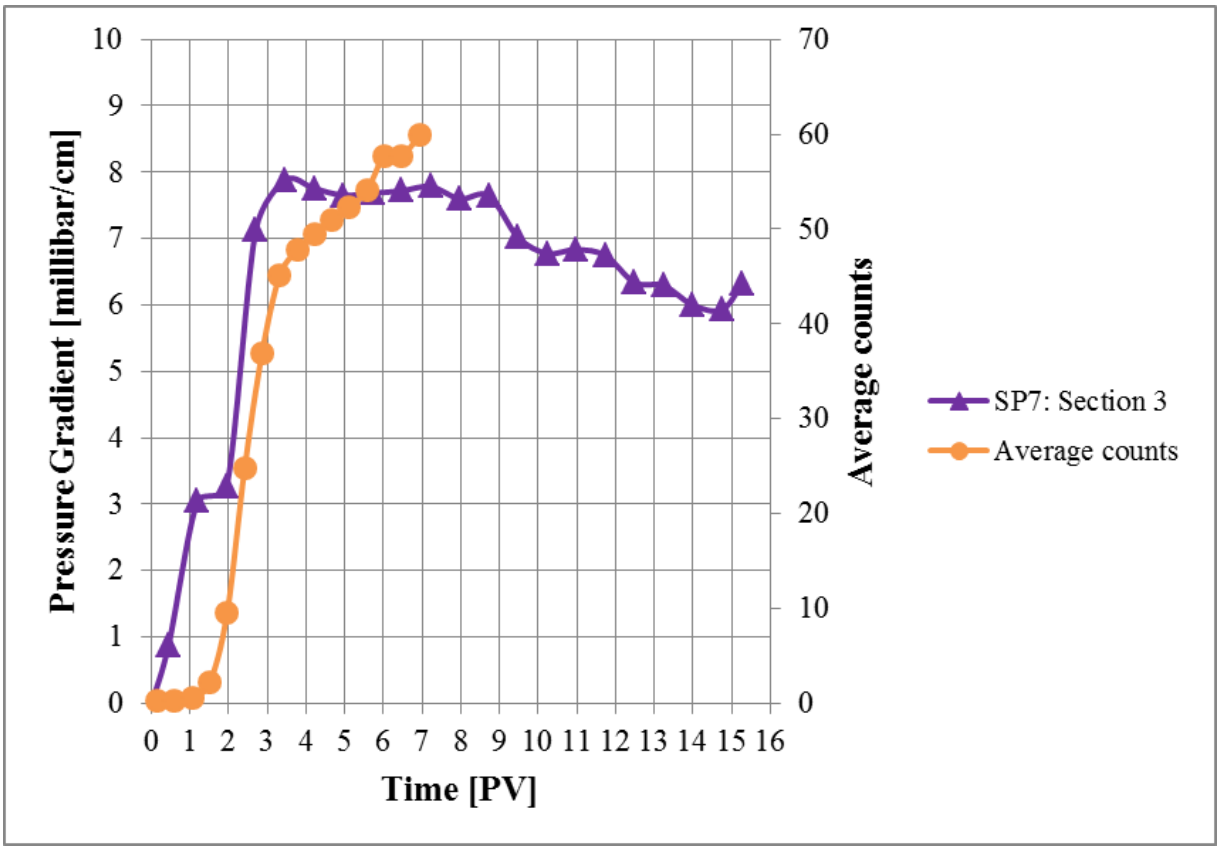

Figure 10.22: The calculated pressure gradient [millibar/cm] across section 3 (purple) in SP7 and average counts per 1D saturation profile (orange) as a function of time [PV] during co-injection (experiment 13). Section 3 represents the calculated pressure gradient between pressure ports B and C. Average counts per 1D saturation profile represent the average surfactant+polymer saturation.

Figure 10.23 shows a 2D visualization of the in-situ saturation development of the labeled surfactant+polymer solution during polymer enhanced foam by co-injection into SP7 (experiment 13) during 8 time steps. SP7 was vertically sliced and the saturation development recorded by the PET scanner was located 12.5 cm into SP7. The CT scan of the sand pack defined the boundaries of SP7 and is indicated by grey in all images. The color specter displayed at the bottom is the detected PET signal from ^{18}FDG. Warm colors indicate high concentrations of ^{18}FDG and cold colors indicate low concentrations of ^{18}FDG. The grey color in the color specter shows the activity level of the PET signal during the co-injection. The saturation of the labeled surfactant+polymer solution developed gradually from the bottom of the vertical slice of SP7 towards the top from t=1.1 PV until t=2.9 PV. This can indicate that the fluid phase during the co-injection was gravity segregated. From t=3.3 PV to t=6.9 PV the saturation of the labeled surfactant+polymer solution was relatively constant, but

the detected signal was stronger on the right-hand side of the vertical slice compared to the left-hand side during the co-injection.

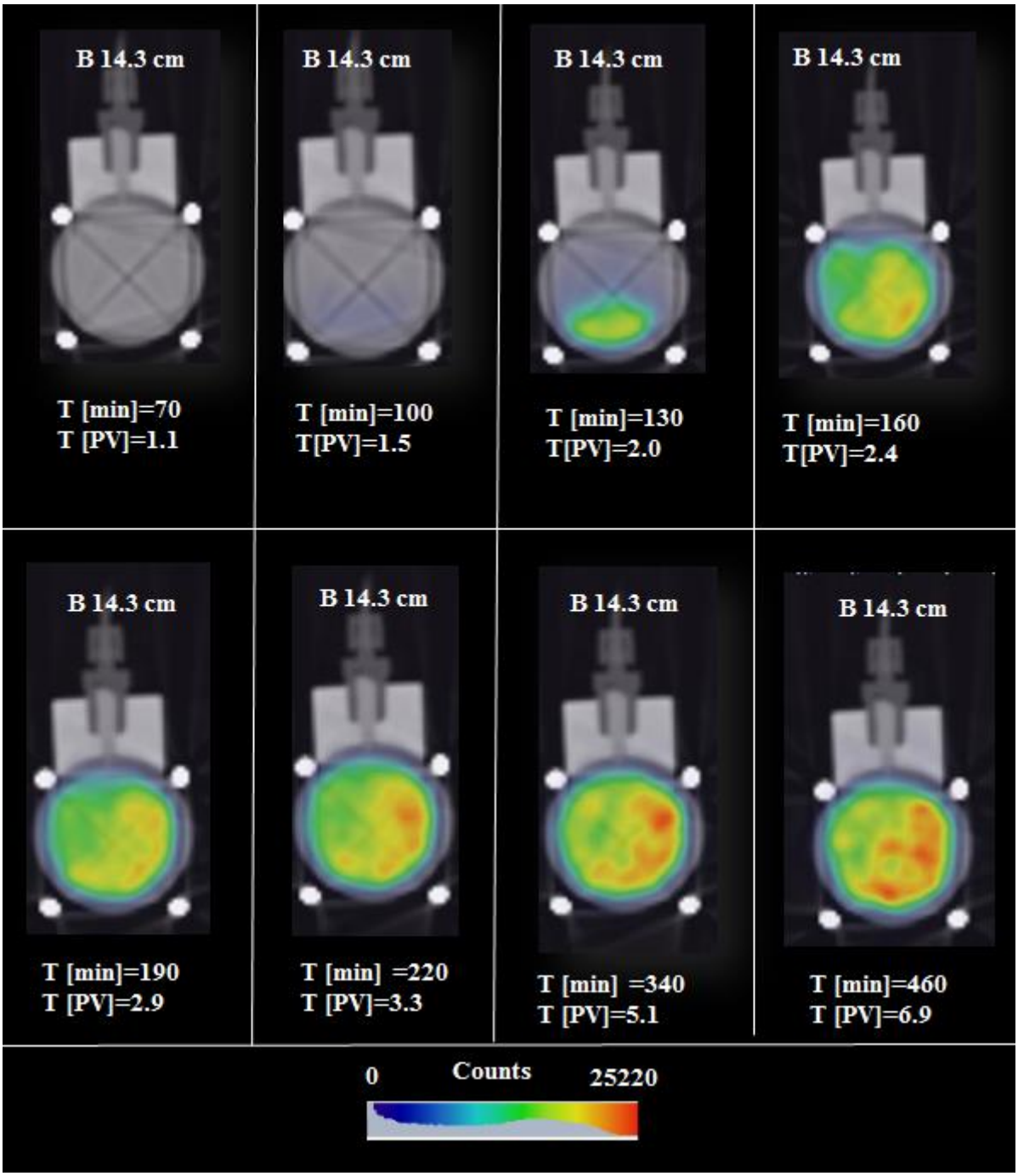

Figure 10.23: 2D visualization of PET recording of the in-situ saturation development of surfactant+polymer solution during co-injection into SP7 (experiment 13) at 8 time steps. SP7 was vertically sliced and the saturation development recorded by the PET scanner was located 12.5 cm into SP7. B 14.3 cm denoted the location of pressure port B in SP7. The CT scan of the sand pack defined the boundaries of SP7 and is indicated by grey in all images. The color specter displayed in horizontal at the bottom is the detected PET signal from ^{18}FDG. Warm colors indicate high concentrations of ^{18}FDG and cold colors indicate low concentrations of ^{18}FDG. The grey color on the color specter shows the activity level of the PET signal during the co-injection.

Figure 10.24 shows the development in absolute pressure in pressure port B during the co-injection into SP7. At t=2 PV the absolute pressure was maximum, while the labeled surfactant+polymer saturation in **Figure 10.23** was at the bottom of SP7. Between t=2-3.5 PV the absolute pressure decreased, whereas the saturation of the labeled surfactant + polymer solution was constant from t=3.3 PV (see **Figure 10.23**). This indicates the there was no 1:1 relationship between the absolute pressure and the saturation of the labeled surfactant+polymer solution. This also suggest that the saturation of the labeled surfactant +polymer solution did not follow the absolute pressure development in pressure port B, as foam was also generated by the non-labeled surfactant+polymer solution that was injected into SP7 prior to the co-injection to satisfy adsorption.

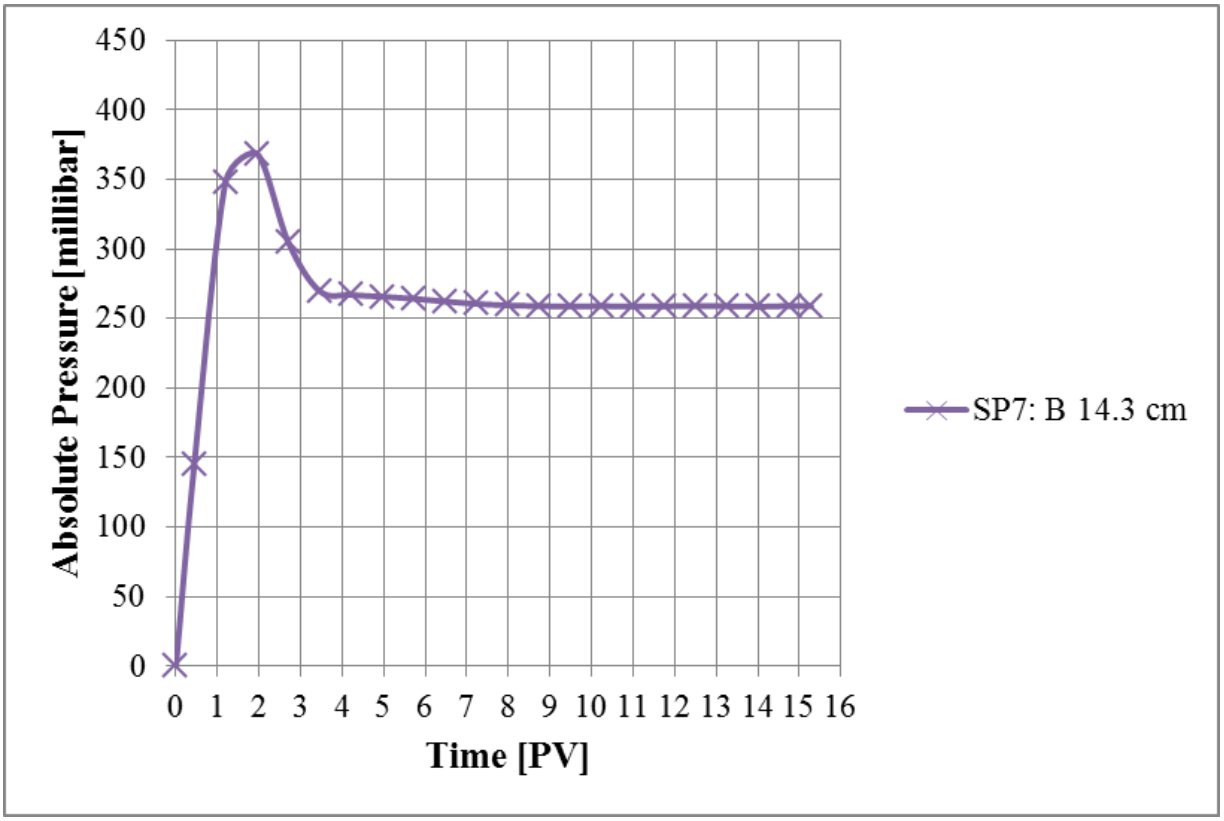

Figure 10.24: Absolute pressures [millibar] as a function of time [PV] measured at pressure port B along the sand pack during co-injection into SP7 (experiment 13).

Figure 10.25 shows a 2D visualization of the in-situ saturation development of the labeled surfactant+polymer solution during polymer enhanced foam by co-injection into SP7 (experiment 13) at 8 time steps. SP7 was horizontally sliced and the saturation development recorded by the PET scanner was located 12.5-29.1 cm into SP7. B 14.3 cm denotes the location of pressure port B and C 24.3 cm denotes the location of pressure port C. During the co-injection the saturation developed from the bottom of SP7 towards the top between t=1.5 PV and t=2.9 PV. This can indicate that the development of the front was dispersed. From t=3.3 PV the front of the surfactant+polymer solution had advanced through the scanned section of SP7 and the saturation continued to increase until t=6.9 PV. However, the saturation of surfactant+polymer was not distributed evenly across the scanned section. The detected signals were stronger in both ends of the section compared to the middle of the section. Weaker signals were detected in the middle of the section. Strong signals can indicate high porosity, whereas weaker signals can indicate lower porosity or that trapped gas occupy the pores pace.

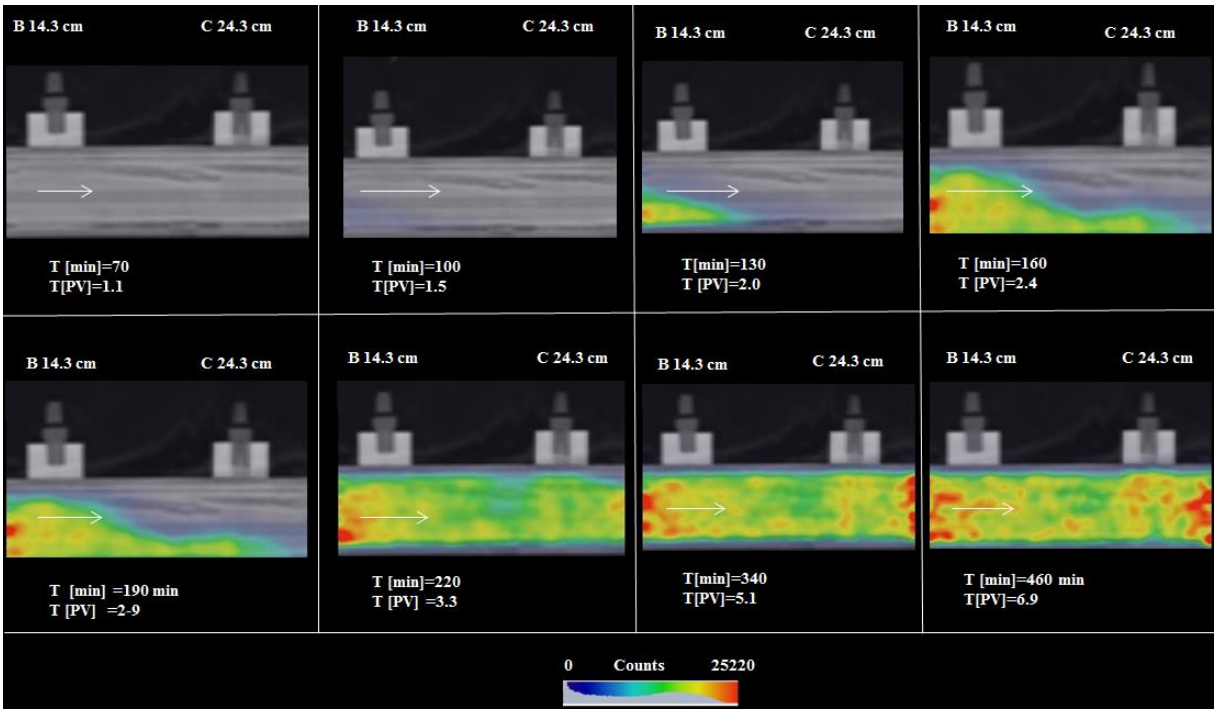

Figure 10.25: 2D visualization of PET recording of the in-situ saturation development of surfactant+polymer solution during co-injection into SP7 (experiment 13) at 8 time steps. SP7 was horizontally sliced and the saturation development recorded by the PET scanner was located 12.5-29.1 cm into SP7. Flow direction is indicated by the arrows.

Figure 10.26 displays a 3D visualization of the in-situ saturation development of surfactant+polymer solution during polymer enhanced foam by co-injection across the 16.6 cm long scan along SP7 (experiment 13) at 8 time steps. Each 3D picture consist of 83 images with voxel size 2mm * 2 mm*0.6 mm in x,-y- and z direction, respectively. The 3D pictures also display the location of pressure ports B and C as well as the threaded steel rods on the outside of the sand pack.

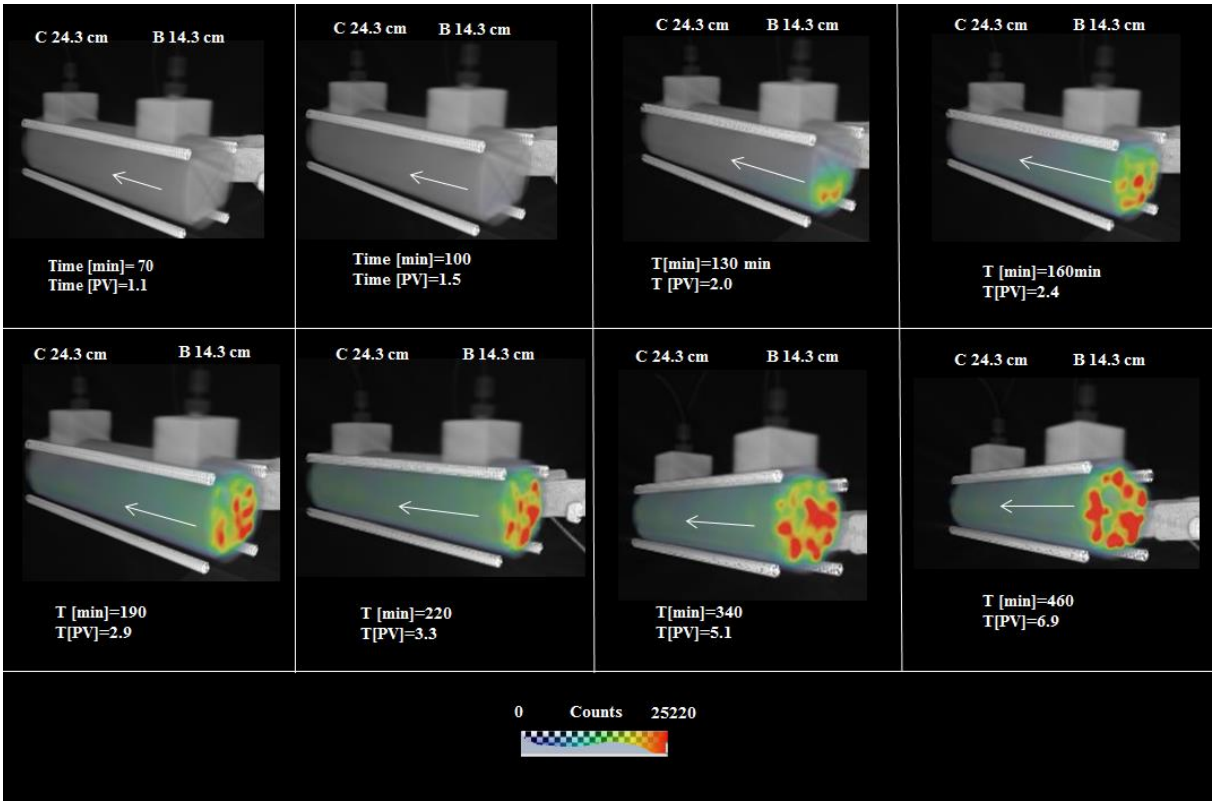

Figure 10.26: 3D visualization of PET recording of the in-situ saturation development of surfactant+polymer solution during polymer enhanced foam by co-injection into SP7 (experiment 13) at 8 time steps.

11. Uncertainties Related to the Experiments

A summary of the uncertainties related to the experiments are briefly discussed in this chapter. Uncertainties are important to take into account when reviewing the reliability of the experimental results. The uncertainties related to all the experimental work in this thesis can be divided into two categories:

- Equipment uncertainties
- Experimental uncertainties

The total uncertainty of an experiment is the sum of the associated uncertainties in each step of the preparations and implementation of the experiments, and the uncertainties related to the equipment.

All the equipment used in the experiments has an associated uncertainty. **Table A.1** in Appendix A lists the equipment uncertainties. Equations used for calculating the uncertainty for porosity and permeability of the sand packs based on the equipment uncertainties are presented in Appendix A.

All experimental work has uncertainties that can influence the accuracy of the measurements. The most significant experimental uncertainties with respect to the experimental work in this thesis are:

- **Errors in readings:** Reading the foam decay height from the graded glass cylinder during the foam coalescence tests was sometimes challenging, due to the angle of the web camera, oil spreading on the lamellae and difficulties in defining the foam height.
- **Sand pack properties:** There are uncertainties in measurements such as pore volume, bulk volume, porosity and permeability that depend on other factors and equipment that contain uncertainties. As an example the pore volume of the sand packs was found based on the measured weight difference between a dry and brine saturated sand pack. A vacuum pump removed air from the sand packs and 100 % brine saturation was assumed. If air was left behind in the pore space an underestimation of the pore volume could be the consequence.
- **Leakage:** Leaks often occur in experimental set-ups and systems with many fittings and components. Leaks are likely to occur during rebuilding and tuning. Minor leaks can be time consuming and difficult to detect and sometimes increase the uncertainty

in an experiment. In some cases the leak is so significant that the experiments are aborted.

- **Pressure measurements:** Fluctuations in the ESI pressure transducers were observed during the permeability measurements and during the co-injections, hence uncertainties occur in the actual pressure measurements.
- **Concentration:** Uncertainties were also present in the mixing of the foaming solutions and the brine. A weight was used to determine the volume of the fluids, NaCl and polymer. Too low or too high concentrations of surfactant or polymer can affect the foam generation and consequently the behavior of foam flow.

Part 4: Conclusions and Future Work

12. Concluding Remarks

In this thesis experiments were performed to investigate the observed difference in the development of pressures during co-injection of N_2 gas and two different foaming solutions, one with and one without polymer added for foam stability. Foam generation and flow behavior were studied in unconsolidated sand packs to evaluate the potential of polymer enhanced foam for IEOR application. A PET-CT scanner was used to visualize the saturation development of the foam solution within a sand pack. In addition, bulk foam coalescence tests were conducted to investigate the foam stability with or without the presence of different oils.

12.1 Key Observations from the Foam Coalescence Tests

- The foam columns stabilized by surfactant without oil had constant height during the foam decay regime and foam collapsed due to gravitational liquid drainage.
- The foam column stabilized by surfactant in the presence of n-Decane or crude oil were divided into several parts during the foam decay regime and the foam collapsed due to gravitational liquid drainage and the presence of oil.
- The foam columns stabilized by surfactant without oil had longer longevity compared to the foam columns with oil.
- As the amount of n-Decane increased the foam column was divided into several parts and the time it took to reduce the foam height to zero was decreased.
- The foam column decayed faster in the presence of crude oil compared to the presence of n-Decane.

12.2 Key Observations from Surfactant Foam and Polymer Enhanced Foam

- The absolute pressure stabilized at plateau values during co-injection of N_2 gas and surfactant solution.
- The absolute pressure did not reach stable conditions during co-injection of N_2 gas and surfactant+polymer solution due to trapped gas.
- The pressure gradients during co-injection of N_2 gas and surfactant solution increased before they decreased and stabilized.
- The pressure gradients during co-injection of N_2 gas and surfactant+polymer did not become stable.
- The apparent viscosity for surfactant foam and polymer enhanced foam varied across the four sections in the sand packs. The apparent viscosity was significantly higher in

section 2, 3 and 4 compared to section 1 close to the inlet. This indicates that stronger foam was generated across sections 2, 3 and 4 compared to section 1.

- The apparent viscosity for surfactant foam and polymer enhanced foam increased with higher permeability, but not for all co-injections.
- Both surfactant foam and polymer enhanced foam were generated successfully in unconsolidated sand packs.
- The data obtained from the PET-CT scanner were used to visualize investigate the saturation development of surfactant+polymer solution during co-injections. The saturation development of the foaming solution was not uniform across the scanned section of the sand pack and within t=7 PV the saturation had not reached stable state.

13. Future Work

- The bulk foam coalescence tests should be carried out with a foaming solution containing surfactant + polymer
- The foam coalescence test should be conducted with the presence of additional oils such as hexane and heptane to investigate the effect on foam stability.
- A better method need to be developed to be able to quantify foam stability by the half-life measurements of foam decay height.
- A standard procedure for sand packing need to be developed to obtain homogenous sand packs. An advantage with respect to homogenous sand packs is that direct comparison of foam generation and flow behavior can be established.
- Polymer enhanced foam injections for IEOR in unconsolidated sand pack should be performed in sand packs with larger dimensions. Both cross sectional area and length of the sand packs should be changed, because this could yield results more representative for a reservoir. In addition the pressure gradient should be measured across several different intervals of the longer sand pack to evaluate the foam generation.
- Further work on generation of polymer enhanced foam should be carried out under reservoir conditions. A better understanding of how polymer enhanced foam behaves with oil present in unconsolidated sand packs should be performed and tested for oil displacement efficiency.
- More visualization studies of polymer enhanced foam should be carried out and also labeling the N_2 gas to study the development of trapped gas should be considered.

14. References

AHMED, T. 2006. *Reservoir engineering handbook,* Amsterdam, Elsevier.

ALI, S. & THOMAS, S. 1996. The promise and problems of enhanced oil recovery methods. *Journal of Canadian Petroleum Technology,* 35.

ALVARADO, V. & MANRIQUE, E. 2010. Enhanced oil recovery: an update review. *Energies,* 3**,** 1529-1575.

ALVAREZ, J., RIVAS, H. & ROSSEN, W. 2001. Unified model for steady-state foam behavior at high and low foam qualities. *SPE J.,* 6**,** 325-333.

APAYDIN, O. & KOVSCEK, A. 2001. Surfactant concentration and end effects on foam flow in porous media. *Transp. Porous Media,* 43**,** 511-536.

BABADAGLI, T. 2007. Development of mature oil fields—A review. *Journal of Petroleum Science and Engineering,* 57**,** 221-246.

BEARD, D. & WEYL, P. 1973. Influence of texture on porosity and permeability of unconsolidated sand. *AAPG bulletin,* 57**,** 349-369.

BERTIN, H., QUINTARD, M. & CASTANIER, L. 1998. Development of a bubble-population correlation for foam-flow modeling in porous media. *SPE Journal,* 3**,** 356-362.

BJORLYKKE, K. 2010. *Petroleum Geoscience: From Sedimentary Environments to Rock Physics,* Berlin, Heidelberg, Springer Berlin Heidelberg: Berlin, Heidelberg.

BOND, D. C. & HOLBROOK, O. C. 1958. Gas drive oil recovery process. Google Patents.

BRATTEKÅS, B. 2014. Conformance Control for Enhanced Oil Recovery in Fractured Reservoirs. The University of Bergen.

BUREIKO, A., TRYBALA, A., KOVALCHUK, N. & STAROV, V. 2014. Current applications of foams formed from mixed surfactant–polymer solutions. *Advances in colloid and interface science*.

CHANG, H. L. 1978. Polymer flooding technology yesterday, today, and tomorrow. *Journal of Petroleum Technology,* 30**,** 1,113-1,128.

CHAOUKI, J., LARACHI, F. & DUDUKOVIÉ, M. 1997. NON-MEDICAL APPLICATIONS OF POSITRON EMISSION TOMOGRAPHY. *Non-Invasive Monitoring of Multiphase Flows***,** 161.

CHEN, M., YORTSOS, Y. & ROSSEN, W. A pore-network study of the mechanisms of foam generation. SPE Annual Technical Conference and Exhibition, 2004. Society of Petroleum Engineers.

COLES, M., MUEGGE, E., AUZERAIS, F., FRULLA, P. & KANTZAS, A. The Use of Attenuation Standards for CT Scanning. SCA Conference Paper Number, 1995.

DAVID, A. & MARSDEN JR, S. S. The rheology of foam. Fall Meeting of the Society of Petroleum Engineers of AIME, 1969. Society of Petroleum Engineers.

DONALDSON, E. C., CHILINGARIAN, G. V. & YEN, T. F. 1989. *Enhanced oil recovery, II: Processes and operations*, Elsevier.

FARAJZADEH, R., ANDRIANOV, A., KRASTEV, R., HIRASAKI, G. J. & ROSSEN, W. R. 2012. Foam–oil interaction in porous media: Implications for foam assisted enhanced oil recovery. *Advances in Colloid and Interface Science,* 183–184**,** 1-13.

FARAJZADEH, R., ANDRIANOV, A. & ZITHA, P. L. J. Foam assisted oil recovery at miscible and immiscible conditions. Kuwait International Petroleum Conference and Exhibition, 2009. Society of Petroleum Engineers.

FARAJZADEH, R., MURUGANATHAN, R., ROSSEN, W. R. & KRASTEV, R. 2011. Effect of gas type on foam film permeability and its implications for foam flow in porous media. *Advances in colloid and interface science,* 168**,** 71-78.

FERNØ, M. A., GAUTEPLASS, J., HAUGE, L. P., ABELL, G. E., ADAMSEN, T. C. H. & GRAUE, A. 2015. Combined positron emission tomography and computed tomography to visualize and quantify fluid flow in sedimentary rocks. *Water Resources Research,* 51**,** 7811-7819.

FRASER, H. 1935. Experimental study of the porosity and permeability of clastic sediments. *The Journal of Geology***,** 910-1010.

GRATON, L. C. & FRASER, H. 1935. Systematic packing of spheres: with particular relation to porosity and permeability. *The Journal of Geology***,** 785-909.

HIRASAKI, G. 1989. A Review of Steam-Foam Process Mechanisms. *paper SPE,* 19518.

HIRASAKI, G. & LAWSON, J. 1985. Mechanisms of foam flow in porous media: apparent viscosity in smooth capillaries. *Society of Petroleum Engineers Journal,* 25**,** 176-190.

JAHN, F., COOK, M. & GRAHAM, M. 1998. *Hydrocarbon exploration and production,* Amsterdam, Elsevier.

JAHN, F., COOK, M. & GRAHAM, M. 2008. *Hydrocarbon exploration & production,* Elsevier.

JENKINS, R. D. & BASSETT, D. R. 1997. Synergistic interactions among associative polymers and surfactants. *Polymeric Dispersions: Principles and Applications.* Springer.

KAM, S. & ROSSEN, W. 2003. A model for foam generation in homogeneous media. *SPE Journal,* 8**,** 417-425.

KANTZAS, A., MARENTETTE, D. & ALLSOPP, K. 1999. Utilization of polymer gels, polymer enhanced foams, and foamed gels for improving reservoir conformance. *Journal of Canadian Petroleum Technology,* 38.

KETCHAM, R. A., CARLSON, W. D., MARSCHALLINGER, R. & JOHNSON, S. E. 2001. Acquisition, optimization and interpretation of X-ray computed tomographic imagery; applications to the geosciences. *Computers & Geosciences,* 27**,** 381-400.

KHALILI, A., BASU, A. & PIETRZYK, U. 1998. Flow visualization in porous media via positron emission tomography. *Physics of Fluids (1994-present),* 10**,** 1031-1033.

KHATIB, Z., HIRASAKI, G. & FALLS, A. 1988. Effects of capillary pressure on coalescence and phase mobilities in foams flowing through porous media. *SPE reservoir engineering,* 3**,** 919-926.

KOVSCEK, A. & RADKE, C. 1993. Fundamentals of foam transport in porous media. Lawrence Berkeley Lab., CA (United States).

KRUMBEIN, W. & MONK, G. 1943. Permeability as a function of the size parameters of unconsolidated sand. *Transactions of the AIME,* 151**,** 153-163.

KUTAY, S. & SCHRAMM, L. 2004. Structure/performance relationships for surfactant and polymer stabilized foams in porous media. *Journal of Canadian Petroleum Technology,* 43.

LAKE, L. W. 2010. *Enhanced oil recovery,* Richardson, Tex, Society of Petroleum Engineers.

LAKE, L. W., CHILINGARIAN, G. V. G. V., DONALDSON, E. C. E. C. & YEN, T. F. T. F. 1989. *Enhanced Oil Recovery, II*.

LATIL, M., BARDON, C. & INSTITUT FRANÇAIS DU, P. 1980. *Enhanced oil recovery,* Paris, Editions technip.

LEE, S. & KAM, S. 2013. Enhanced oil recovery by using CO2 foams: fundamentals and field applications. *Enhanced Oil Recovery Field Case Studies***,** 23-63.

LEMMON E.W. , M. O. M. A. D. G. F. 2016. Thermophysical Properties of Fluid Systems in NIST Chemistry Webbook, NIST Standard Reference Database Number 69. Gaithersburg MD Eds. P.J. Linstrom and W.G. Mallard, National Institute of Standards and Technology.

LI, Z., ZHOU, G. & ZHOU, Z. The feasibility studies of polymer foam flooding in Gudao oilfield. SPE Asia Pacific Oil & Gas Conference and Exhibition, 2006. Society of Petroleum Engineers.

LIE, S. H. 2013. Diffusion as an oil recovery mechanism during CO_2 injection in fractured reservoirs. Bergen: Department of Physics and Technology, University of Bergen.

LIONTAS, R., MA, K., HIRASAKI, G. J. & BISWAL, S. L. 2013. Neighbor-induced bubble pinch-off: novel mechanisms of in situ foam generation in microfluidic channels. *Soft Matter,* 9**,** 10971-10984.

MANLOWE, D. J. & RADKE, C. J. 1990. A pore-level investigation of foam/oil interactions in porous media. *SPE Reservoir Engineering,* 5**,** 495-502.

MANNHARDT, K., NOVOSAD, J. & SCHRAMM, L. Foam/oil interations at reservoir conditions. SPE/DOE Improved Oil Recovery Symposium, 1998. Society of Petroleum Engineers.

MANRIQUE, E. J., THOMAS, C. P., RAVIKIRAN, R., IZADI KAMOUEI, M., LANTZ, M., ROMERO, J. L. & ALVARADO, V. EOR: current status and opportunities. SPE improved oil recovery symposium, 2010. Society of Petroleum Engineers.

NAGTEGAAL, P. 1978. Sandstone-framework instability as a function of burial diagenesis. *Journal of the Geological Society,* 135**,** 101-105.

NGUYEN, Q. P., ALEXANDROV, A. V., ZITHA, P. L. & CURRIE, P. K. Experimental and modeling studies on foam in porous media: a review. SPE International Symposium on Formation Damage Control, 2000. Society of Petroleum Engineers.

NGUYEN, Q. P., ROSSEN, W. R., ZITHA, P. L. & CURRIE, P. K. 2009. Determination of gas trapping with foam using X-ray computed tomography and effluent analysis. *SPE Journal,* 14**,** 222-236.

OSTERLOH, W. & JANTE JR, M. Effects of gas and liquid velocity on steady-state foam flow at high temperature. SPE/DOE Enhanced Oil Recovery Symposium, 1992. Society of Petroleum Engineers.

PATZEK, T. 1996. Field applications of steam foam for mobility improvement and profile control. *SPE Reserv. Eng.,* 11**,** 79-85.

POWERS, M. C. 1953. A new roundness scale for sedimentary particles. *Journal of Sedimentary Research,* 23.

RADKE, C. & GILLIS, J. A dual gas tracer technique for determining trapped gas saturation during steady foam flow in porous media. SPE Annual Technical Conference and Exhibition, 1990. Society of Petroleum Engineers.

RANSOHOFF, T. & RADKE, C. 1988. Mechanisms of foam generation in glass-bead packs. *SPE reservoir engineering,* 3**,** 573-585.

ROGERS, J. J. & HEAD, W. B. 1961. Relationships between porosity, median size, and sorting coefficients of synthetic sands. *Journal of Sedimentary Research,* 31.

ROMERO-ZERON, L. B. & KANTZAS, A. 2007. The effect of wettability and pore geometry on foamed-gel-blockage performance. *SPE Reservoir Evaluation & Engineering,* 10**,** 150-163.

ROSSEN, W. R. 1996. Foams in enhanced oil recovery. *Surfactant Science Series***,** 413-464.

SCHRAMM, L. L. 2006. *Emulsions, foams, and suspensions: fundamentals and applications*, John Wiley & Sons.

SELIN, R. 2013. The Outlook for Energy: A View to 2040.

SELLEY, R. C. & SONNENBERG, S. A. 2015. *Elements of petroleum geology,* San Diego, Calif, Academic Press.

SHENG, J. 2010. *Modern chemical enhanced oil recovery: theory and practice*, Gulf Professional Publishing.

SHENG, J. J. 2013a. Foams and Their Applications in Enhancing Oil Recovery. *Enhanced Oil Recovery Field Case Studies***,** 251.

SHENG, J. J. 2013b. Polymer Flooding—Fundamentals and Field Cases. *Enhanced Oil Recovery Field Case Studies***,** 63-82.

SIMJOO, M., REZAEI, T., ANDRIANOV, A. & ZITHA, P. L. J. 2013. Foam stability in the presence of oil: Effect of surfactant concentration and oil type. *Colloids and Surfaces A: Physicochemical and Engineering Aspects,* 438**,** 148-158.

SKARESTAD, M. & SKAUGE, A. 2005. PTEK 213–Reservoarteknikk II. *Universitetet i Bergen, Bergen*.

SKAUGE, A., SPILDO, K., HØILAND, L. & VIK, B. 2007. Theoretical and experimental evidence of different wettability classes. *Journal of Petroleum Science and Engineering,* 57**,** 321-333.

SORBIE, K. S. 2013. *Polymer-improved oil recovery,* Springer Science & Business Media.

SYDANSK, R. 1994a. Polymer-enhanced foams part 1: laboratory development and evaluation. *SPE Advanced Technology Series,* 2**,** 150-159.

SYDANSK, R. D. 1994b. Polymer-Enhanced Foams Part 2: Propagation Through High-Permeability Sandpacks. *SPE Advanced Technology Series,* 2**,** 160-166.

SYDANSK, R. D. & ROMERO-ZERON, L. 2010. *SPE Textbook, Volume 8 : Reservoir Conformance Improvement,* Richardson, Richardson, TX, USA: Society of Petroleum Engineers.

TABER, J. J., MARTIN, F. & SERIGHT, R. 1997. EOR screening criteria revisited-Part 1: Introduction to screening criteria and enhanced recovery field projects. *SPE Reservoir Engineering,* 12**,** 189-198.

TANZIL, D., HIRASAKI, G. J. & MILLER, C. A. Mobility of foam in heterogeneous media: Flow parallel and perpendicular to stratification. SPE Annual Technical Conference and Exhibition, 2000. Society of Petroleum Engineers.

VALK, P. E., DELBEKE, D., BAILEY, D. L., TOWNSEND, D. W. & MAISEY, M. N. 2006. *Positron emission tomography: clinical practice,* Springer Science & Business Media.

VIKINGSTAD, A. K., SKAUGE, A., HØILAND, H. & AARRA, M. 2005. Foam–oil interactions analyzed by static foam tests. *Colloids and Surfaces A: Physicochemical and Engineering Aspects,* 260**,** 189-198.

WATANABE, N., ISHIBASHI, T., HIRANO, N., TSUCHIYA, N., OHSAKI, Y., TAMAGAWA, T., TSUCHIYA, Y. & OKABE, H. 2011. Precise 3D numerical modeling of fracture flow coupled with X-ray computed tomography for reservoir core samples. *SPE Journal,* 16**,** 683-691.

WITHJACK, E. 1988. Computed tomography for rock-property determination and fluid-flow visualization. *SPE formation evaluation,* 3**,** 696-704.

XU, H. & PU, C. 2014. Experimental Study on Polymer-enhanced Nitrogen Foam Flooding. *Petroleum Science and Technology,* 32**,** 696-702.

ZHOU, S. & SUN, F. 2016. Sand Production Management for Unconsolidated Sandstone Reservoirs.

ZITHA, P., FELDER, R., ZORNES, D., BROWN, K. & MOHANTY, K. 2011. Increasing hydrocarbon recovery factors. *SPE Technol. Updates*.

ZOLOTUKHIN, A. B. & URSIN, J.-R. 2000. *Introduction to petroleum reservoir engineering,* Norwegien Academic Press (HóyskoleForlaget).

Appendix A – Uncertainties and Calculations

Table A.1: Equipment uncertainties

Instrument	Uncertainty
Slide caliper	± 0.002 cm
Folding ruler	± 0.1 cm
Weight	± 0.01 g
ESI digitial USB pressure transducer	± 0.05% F.S. (10 bar)
ESI digitial USB pressure transducer	± 0.01% F.S. (6 bar)
ESI digitial USB pressure transducer	± 0.02% F.S. (4 bar)
ESI digitial USB pressure transducer	± 0.05% F.S. (2.5 bar)
EL-FLOW Mass Flow Controller Bronkhorst High Tech	±0.1 ml/h
Pharmacia LKP Pump P-500	± 0.1 ml/h

Uncertainty equation

The uncertainty, σ_y, of an value, *y*, is given by:

$$\sigma_y = \sqrt{\sum_{i=1}^{n} \left(\frac{\partial y}{\partial x_i} * \sigma_{x_i}\right)^2} \quad \text{(A.1)}$$

where $i=1,...,n$ and $y = f(x_1, x_2, x_3, ... x_n)$ and x_i is an independent variable with an independent uncertainty σ_{x_i}.

Uncertainty in porosity

The porosity is calculated by:

$$\emptyset = \frac{V_p}{V_b} \quad \text{(A.2)}$$

where V_p is the pore volume ,[ml], and V_b is the bulk volume, [ml].

The uncertainty in the porosity, $\sigma_{\emptyset}$, is calculated by input from (A.2) into (A.1) and derivate it:

$$\sigma_{\emptyset} = \sqrt{\left(\frac{1}{V_b} * \sigma_{V_p}\right)^2 + \left(\frac{-V_p}{{V_b}^2} * \sigma_{V_b}\right)^2} \quad \text{(A.3)}$$

where σ_{V_p} is the uncertainty in the pore volume and σ_{V_b} is the uncertainty in the bulk volume.

In order to calculate the uncertainty in porosity the uncertainty in pore volume and in bulk volume must be calculated separately.

The pore volume, V_p ,is given by*:*

$$V_p = \frac{m}{\rho} \quad \text{(A.4)}$$

Where m is the mass difference between unsaturated and saturated sand pack,$[g]$, and ρ is the brine density, $[g/ml]$.

The uncertainty in pore volume σ_{V_p}, is calculated by input of variables from (A.4) into (A.1) and derivate it:

$$\sigma_{V_p} = \sqrt{\left(\frac{1}{\rho} * \sigma_m\right)^2 + \left(-\frac{m}{\rho^2} * \sigma_\rho\right)^2} \quad \text{(A.5)}$$

where σ_m is the uncertainty in mass and σ_ρ is the uncertainty in the brine density.

The bulk volume, V_b, is given by:

$$V_b = \pi * r_{cylinder}^2 * L_{sand} \quad \text{(A.6)}$$

where $r_{\ cylinder}$ is the inner radius of the plastic cylinder, [cm], and L_{sand} is the total length of the sand in the sand pack, [cm].

The uncertainty in bulk volume, σ_{V_b}, is calculated by input of variables from (A.6) into (A.1) and derivate it:

$$\sigma_{V_b} = \sqrt{(2 * \pi * r * L_{sand} * \sigma_r)^2 + \left(r^2 * \pi * \sigma_{L_{sand}}\right)^2} \quad \text{(A.7)}$$

where σ_r is the uncertainty of the radius and $\sigma_{L_{sand}}$ is the uncertainty in the measured length of the sand pack.

Uncertainty in permeability

Based on Darcy`s law the permeability, K, is given as:

$$K = \frac{q*\mu*L}{A*\Delta P} \quad \text{(A.8)}$$

where q is the flow rate $[cm^3/s]$, μ is the viscosity of the fluid [Pa*s], L is the length of the sand [cm], A is the cross sectional area of the sand pack $[cm^2]$ and ΔP is the differential pressure across the sand pack [Pa].

The uncertainty in the permeability is calculated by input of variables from (A.8) into (A.1) and derivate it:

$$\sigma_K = \sqrt{\left(\frac{\mu*L}{A*\Delta P} * \sigma_q\right)^2 + \left(\frac{q*L}{A*\Delta P} * \sigma_\mu\right)^2 + \left(\frac{q*\mu}{A*\Delta P} * \sigma_L\right)^2 + \left(-\frac{q*\mu*L}{A^2*\Delta P} * \sigma_A\right)^2 + \left(-\frac{q*\mu*L}{A*\Delta P^2} * \sigma_{\Delta P}\right)^2} \quad \text{(A.9)}$$

where σ_q is the uncertainty in flow rate , [cm^3/s], σ_μ is the uncertainty in viscosity , [Pa*s], σ_L is the uncertainty of the length, [cm], σ_A is the uncertainty of cross sectional area, [cm^2] and $\sigma_{\Delta P}$ is the uncertainty in the differential pressure.

The permeability can also be found by plotting the measured differential pressure, ΔP, as a function of flow rate , q. Based on plottet trend line and Darcy law (A.8) the permeability can be calculted from the line slope's equation:

$$K = \frac{\mu L}{aA} \tag{A.10}$$

where μ is the viscosity of the fluid [Pa*s], L is the length of the sand [cm], A is the cross sectional area of the sand pack $[cm^2]$ and a is the slope.

The uncertainty in the permeability is calculated by input of variables from (A.10) into (A.1) and derivate it:

$$\sigma_K = \sqrt{\left(\frac{\mu}{a*A} * \sigma_L\right)^2 + + \left(-\frac{\mu*L}{a*A^2} * \sigma_A\right)^2} \tag{A.11}$$

where σ_L is the uncertainty of the length, [cm] and σ_A is the uncertainty of cross sectional area, [cm^2].

Appendix B - Experimental Results

B.1 Surfactant Foam by Co-injection

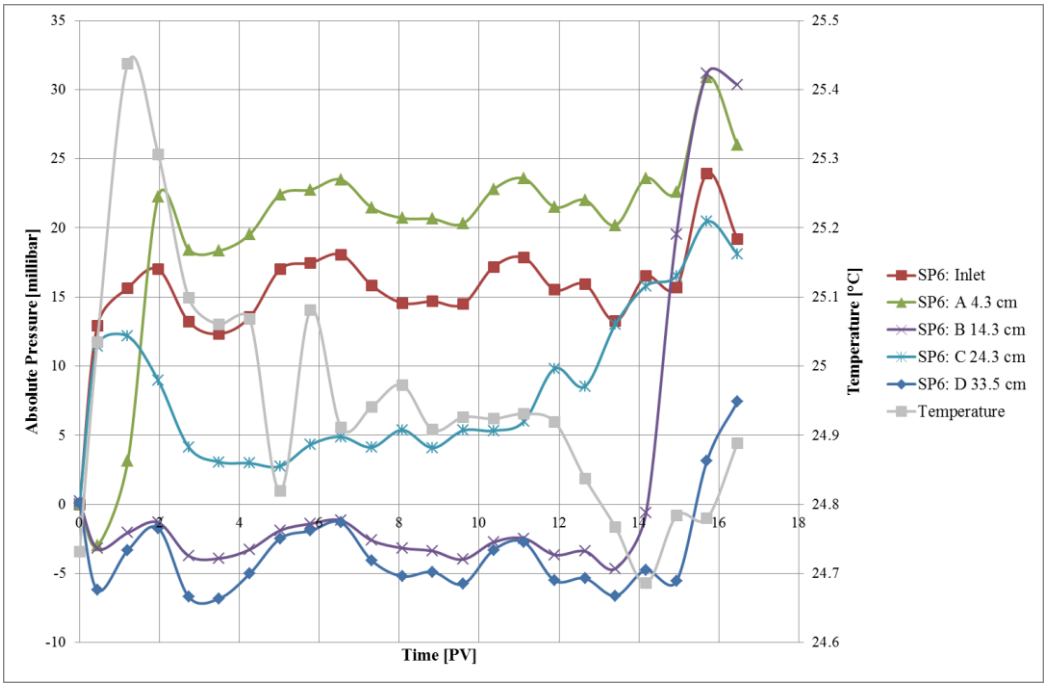

Figure B.1: Absolute pressures [millibar] as a function of time [PV] measured in five different locations along the sand pack during co-injection into SP6 (experiment 10).

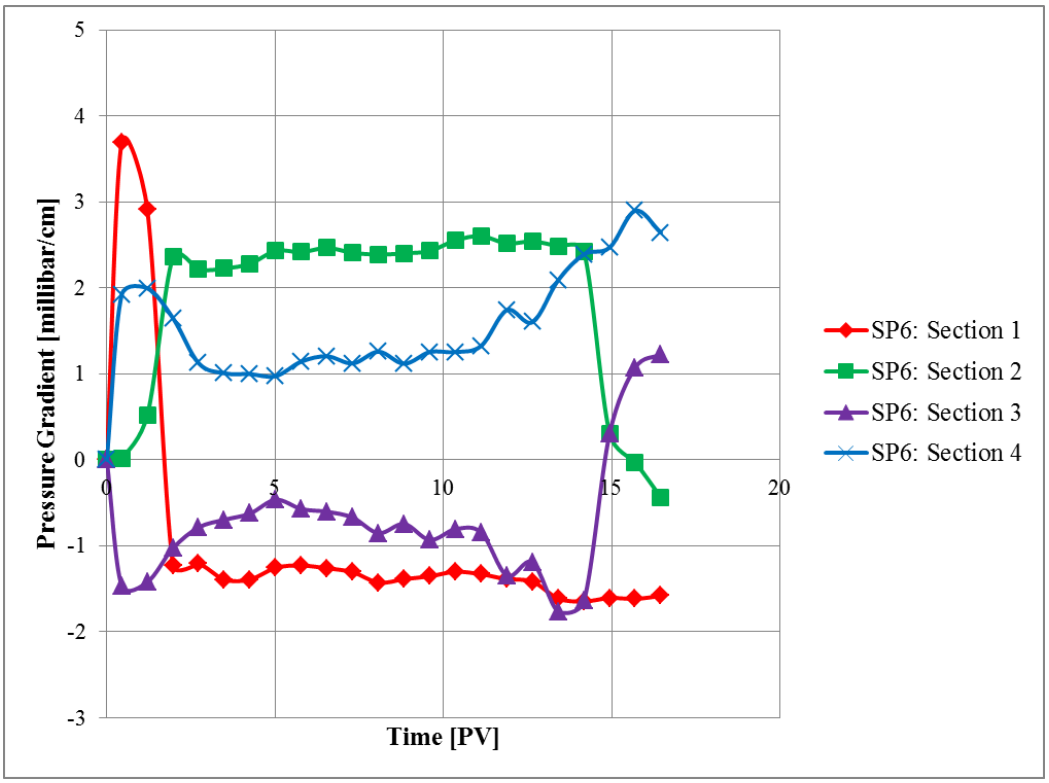

Figure B.2: The pressure gradient [millibar/cm] across four different locations in sand pack SP6 as a function of time [PV] during co-injection (experiment 10).

B.2 Polymer Enhanced Foam by Co-Injection

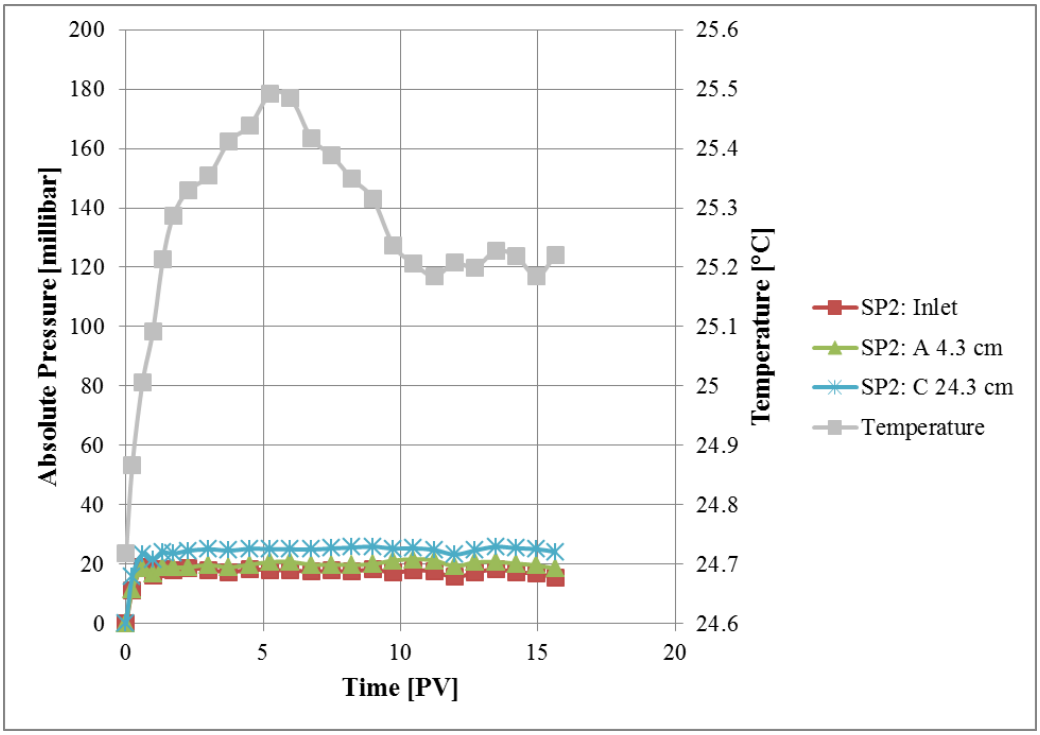

Figure B.3: Absolute pressures [millibar] as a function of time [PV] measured in three different locations along the sand pack during co-injection into SP2 (experiment 1).

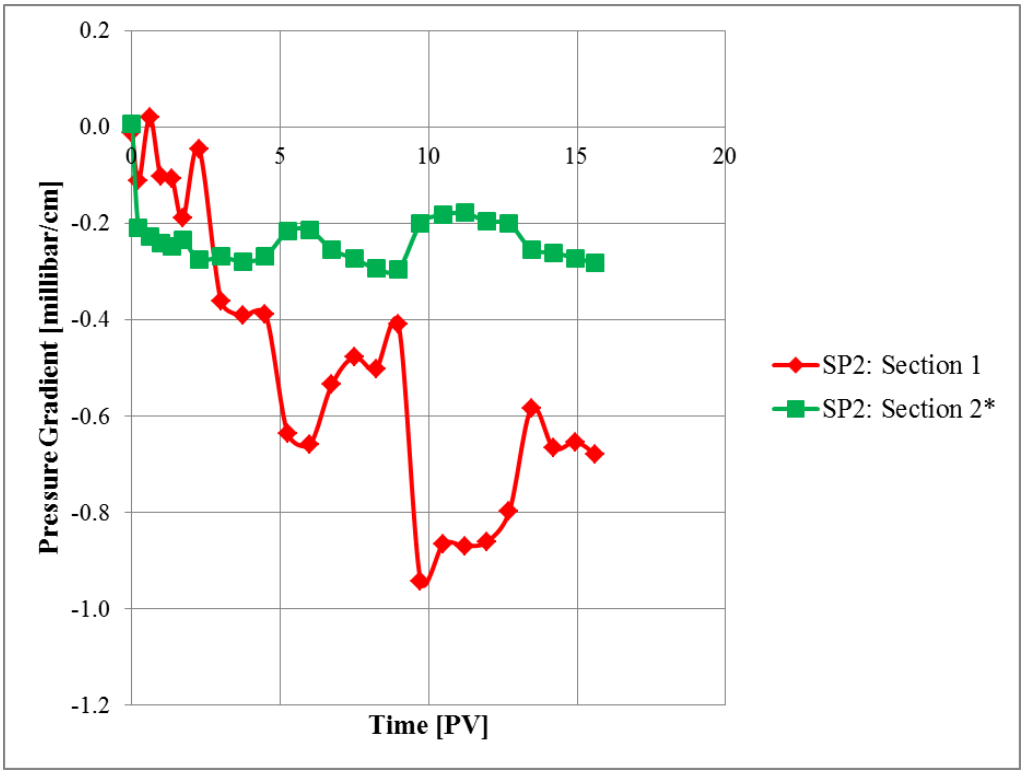

Figure B.4: The pressure gradient [millibar/cm] across two different locations in sand pack SP2 as a function of time [PV] during co-injection (experiment 1). Section 2* is between pressure port A and pressure port C.

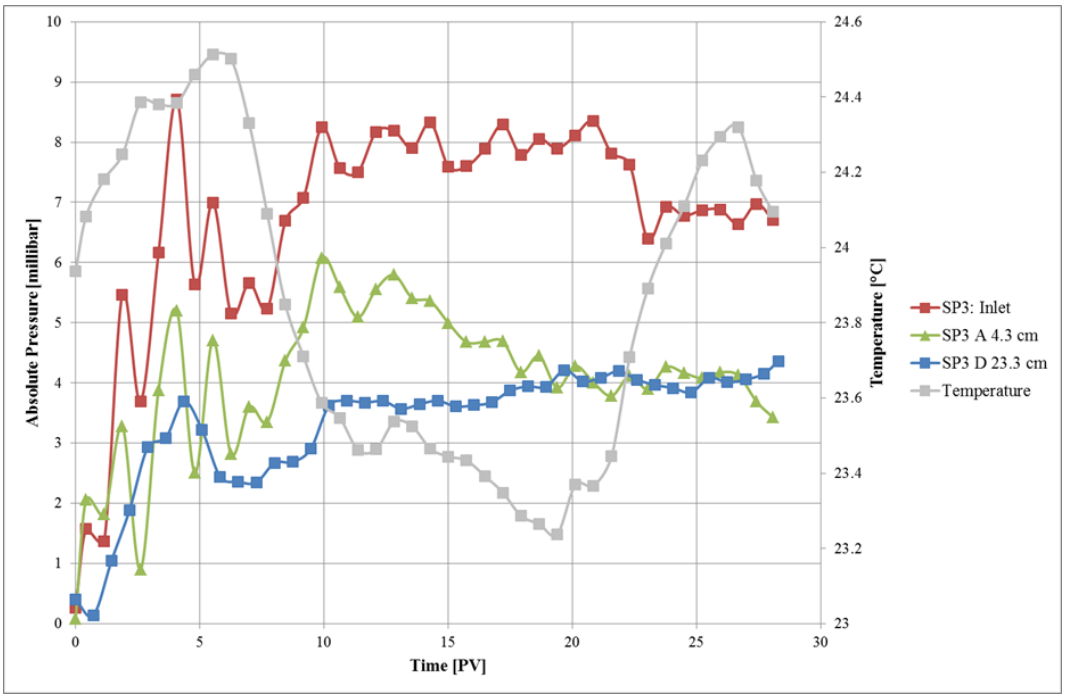

Figure B.5: Absolute pressures [millibar] as a function of time [PV] measured in three different locations along the sand pack during co-injection into SP3 (experiment 2).

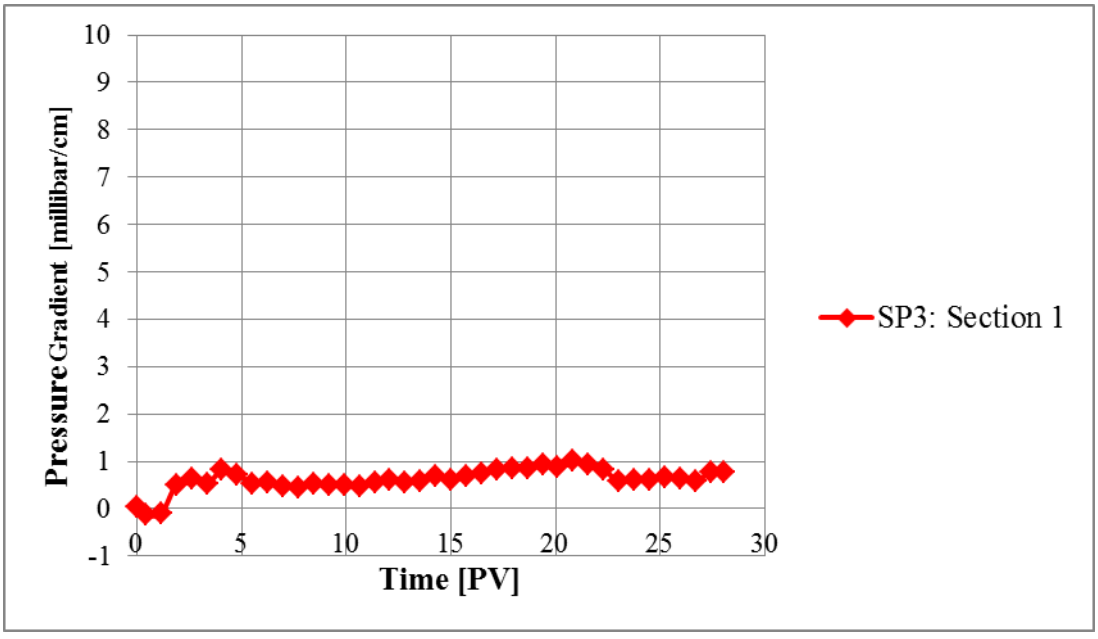

Figure B.6: The pressure gradient [millibar/cm] across section 1 in sand pack SP3 as a function of time [PV] during co-injection (experiment 2).

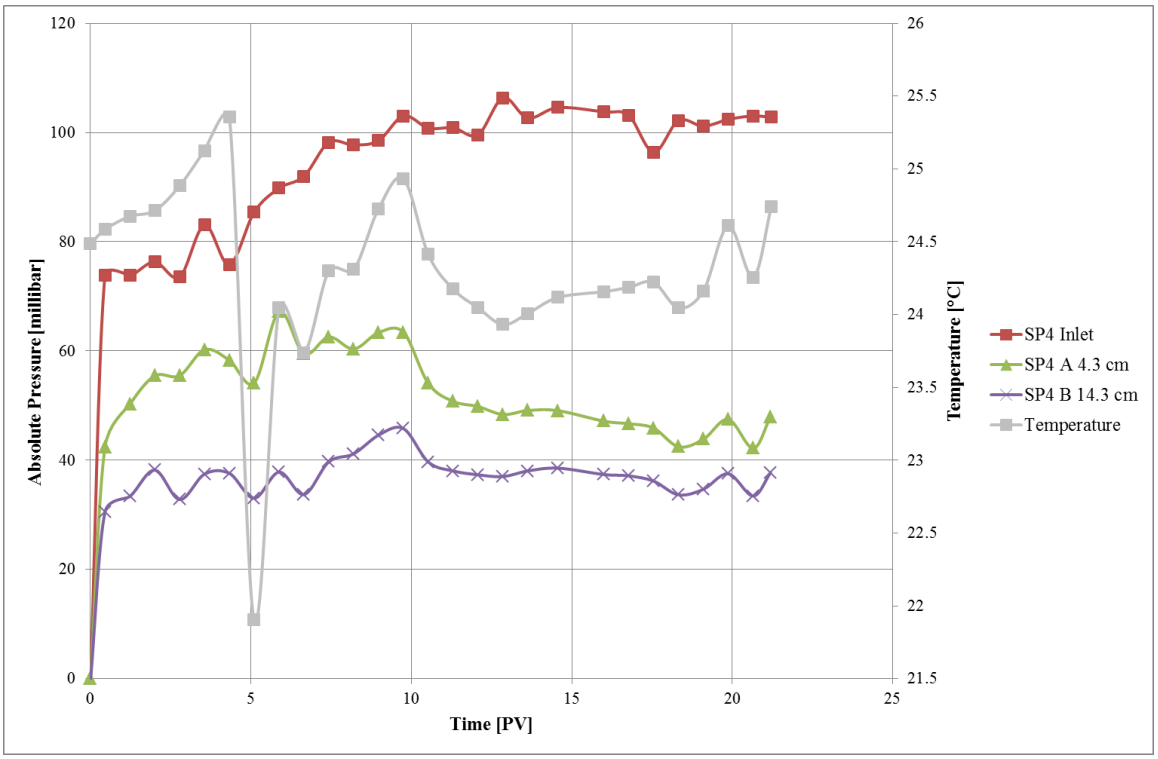

Figure B.7: Absolute pressures [millibar] as a function of time [PV] measured in three different locations along the sand pack during co-injection into SP4 (experiment 4).

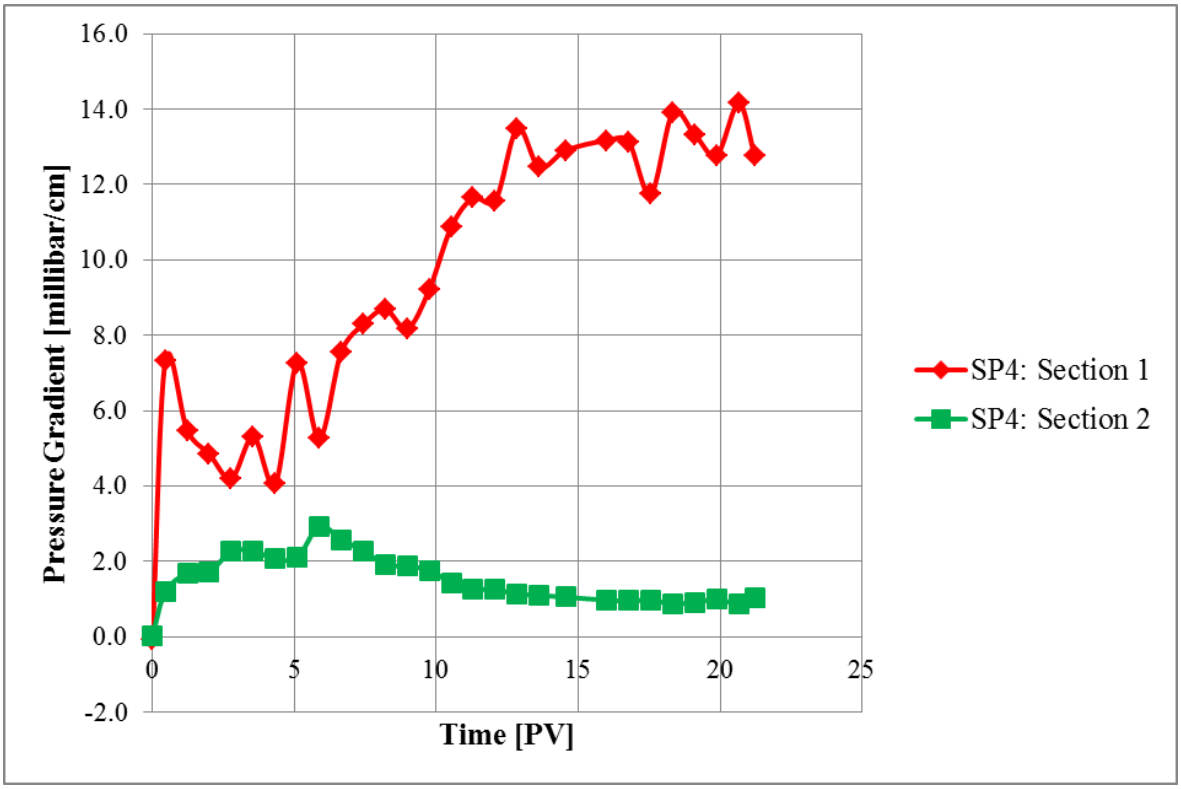

Figure B.8: The pressure gradient [millibar/cm] across two different locations in sand pack SP4 as a function of time [PV] during co-injection (experiment 4).

Appendix C – Abbreviations and Nomenclature

EOR	Enhanced Oil Recovery
IEOR	Integrated Enhanced Oil Recovery
N_2	Nitrogen gas
PET	Positron Emission Tomography
CT	Computed Tomography
PEF	Polymer Enhanced Foam
OOIP	Original Oil in Place
IFT	Interfacial tension
CMC	Critical micelle concentration
HPAM	Hydrolyzed polyacrylamide
IPV	Inaccessible pore volume
SEM	Scanning electron microscopy
POM	Polyformaldehyde
N/A	Not available
Inlet	Inlet Pressure port
A	Pressure port A
B	Pressure port B
C	Pressure port C
D	Pressure port D
SP	Sand pack
UIB	University in Bergen
f_g	Gas fractional flow/ foam quality
h	Film Thickness
Π	Disjoining pressure
P_c^*	Critical capillary pressure
S_w^*	Critical water saturation
E	Entering coefficient

S	Spreading coefficient
B	Bridging coefficient
σ	Interfacial tension
w	Water
g	Gas
o	Oil
μ_{app}	Foam Apparent Viscosity
μ	Fluid viscosity
K	Permeability
q	Flow rate
A	Cross sectional Area
L	Length
Δp	Differential pressure
k_{rf}	Relative permeability of foam
MRF	Mobility Reduction Factor
I	Intensity after have passed through the sample
I_0	Intensity of initial X-ray
μ_a	Linear attenuation coefficient for the scanned sample
x	Thickness of the sample
wt%	Weight percent
Ø	Porosity
V_p	Pore Volume
V_b	Bulk volume
ω_{dry}	Weight of dry sand pack
ω_{wet}	Weight of wet sand pack
ρ	Density
PV	Pore volume of the sand pack